UCLouvain

École polytechnique de Louvain

Analysis of embedded sensor residual stress in carbon fiber composite

Author: **François Berghmans**
Supervisor: **Denis Flandre**
Readers: **Nicolas André, Thomas Pardoen, Nicolas Roisin**
Academic year 2021–2022
Master [120] in Electrical Engineering

Abstract

Smart material have received a lot of attention over the years. One of those smart materials is a self sensing composites, which detects internal damage with sensors embedded in them. This structural health monitoring based on embedded sensors could potentially reduce the cost of maintenance in multiple sectors such as aeronautic and windmills.

This works aims to study the feasibility of embedding a sensor in carbon fiber composites and predicting which sensor could survive the manufacturing process of the composite.

We start by explaining the nature of carbon fiber and its composite form. the challenge that the composite manufacturing poses to the sensor are then explained. Different type of strain gauge are then analysed for their suitability as embedded sensor. A literature review is done to show what works have been done up until now in embedding sensor in composites. Then models and numerical analysis are presented to obtain an estimation of the residual stress of the sensor. This is then compared to two sensors embedded in pure resins, and the challenges associated with the manufacturing step of composite and sensor deployment.

Contents

List of Figures

List of Tables

Glossary

CFC carbon fiber composites. i, iii, v, 3, 5–8, 11, 13, 15–18, 21, 22, 39, 46, 60, 62, 74, 76

CTE coefficient of thermal expansion. iii, 6, 8, 10, 12, 21, 22, 24, 26, 28–31, 33, 38, 39, 41, 43, 44, 46, 48, 52, 62, 76

EFPI Explicit Fabry-Perot interferometer. 16, 18

FBG Fiber bragg grating. 15, 16, 18

PVDF polyvinilidene fluoride. 15

PZT lead zirconate Titanates. 15

RTM Resin transfer molding. 9

SHM structural health monitoring. 3, 8, 11–13, 15, 18, 19, 76, 77

List of Symbols

α	Coefficient of thermal expansion
β	chemical shrinkage coefficient
ϵ	Strain
ϵ_0	Vacuum permittivity
ϵ_r	Relative permittivity
μ	Carrier mobility
ω	Angular frequency
ρ	resistivity
σ	stress
E	Young's modulus
GF	Gauge factor
n	Electron concentration
p	Hole concentration
R	Resistance
T	Temperature
t	thickness
T_g	Glass transition temperature
x	degree of cure

Introduction

As of recently, an increasing interest is being given to smart materials. One of the applications of said smart materials is the damage detection also called structural health monitoring. Both in the aeronautics industry and the energy sector, for windmill mostly, the prospect of reducing cost have pushed for more integrated structural health monitoring. A lot of effort has been focused on monitoring carbon fiber composites with different kind of strain sensor. This work focus on the different parameter that influence the residual stress after manufacturing on the sensor. Even by using only carbon fiber as reinforcement, the number of options available is enormous. Models are explored to understand which choice during the manufacturing has an impact on the result.

The first chapter starts with a cursory explanation of carbon fiber and their composites. it is followed by a small market analysis which shows different sector demands. Then it focusses on the manufacturing process of the composite and the challenge it will bring to the sensor integration. Different sensors will then be presented as well as their drawbacks and advantage for embedding. Finally, the chapter will finish with a literature review of studies about sensors embedded in composites.

Simple analytical model will be presented on the second chapter. Their suitability for the case of embedded sensor will be described and the parameters used to compute the residual stress will be analysed. The simplification of the different materials properties will be explained and the error they generate computed. A model of the curing will be described to show the impact of the curing cycle upon the embedded sensor. To conclude chapter 2, the thermal output of the strain gauges is analysed.

With the result of simple analytical model, a numerical analysis is done in chapter 3. Two software, which were available, are compared with a simple case study that can easily be compared to the analytical results. Afterwards multiple sweeps on different parameters are done to understand the sensitivity of residual stress over them. This is done in two cases, the gauge with and without baking as both geometries are available in the form of commercial strain gauge. Following this, a thermal circuit equivalent is described to obtain an upper estimate of the thermal gradient during cure. And a transient thermal simulation is set up to measure the maximum temperature gradient during the curing. A very brief explanation is given on the original goal of the numerical analysis, a full transient cure simulation.

Finally in the final chapter, the preparations of the experiment in embedding the gauge are described. This highlighted that the difficulty of embedding sensor starts before the manufacturing step. Then the data extracted from the monitoring in-situ during the curing is analysed and problems are highlighted. Afterwards with a bending test, the gauges are

tested for strain known to happen in the aeronautic industry.

The conclusion summarizes the different results obtained all along this work and the potential continuation of this work.

Chapter 1

Overall context and literature overview

This work overarching context, is the integration of sensors in composite material for wireless structural health monitoring (SHM). This first chapter covers the context of this work on the validation for the integration of strain sensors within composites, more specifically carbon fiber composites (CFC).

The first part describes what CFC are and their many variations. Afterwards, a literature review of the fabrication methods of CFC and the challenges that arise from it. It is followed by an overview over the different kind of strain sensors and their compatibility for wireless SHM in CFC. Finally, a review of the literature for embedded sensor in composites was done were the type of sensor, composites and size of both sensor and composite were compared.

1.1 Carbon fibre composite material

1.1.1 Overview

CFC is a system composed of carbon fibre sheet, called a ply, stacked upon each other and a matrix, composed of resin, binding all the plies together. The most basic component of the ply is the carbon fibre. Those fibres are entwined together to form a filament as shown on figure 1.1. Those filaments are then packed together to make a tow. In manufacturers specifications sheet, there will often be a number followed by k such as 3k, 6 k, 12k. Those three numbers of filament per tow are the most common, but other configurations exist. Those represent the number of filaments used to make a single tow. The filament count alone has only a small effect on the final carbon fibre weave properties. The tows are then weaved to make a fabric which, depending on the weaving pattern, will have different properties.

The plain weave, the 2x2 basket and 2/2 twill are called balanced weave. Balanced weaves are weaves with the same amount of vertical and horizontal tow on each side of the weave. Their pattern can be seen on 1.2. This is important to know as it gives the weave symmetric mechanical properties, which is not the case of the imbalanced weave with patterns such as harness satin pattern or unidirectional weave. The type of weaving will heavily influence the product properties such as the drapability. The drapability is the capacity of the weave to

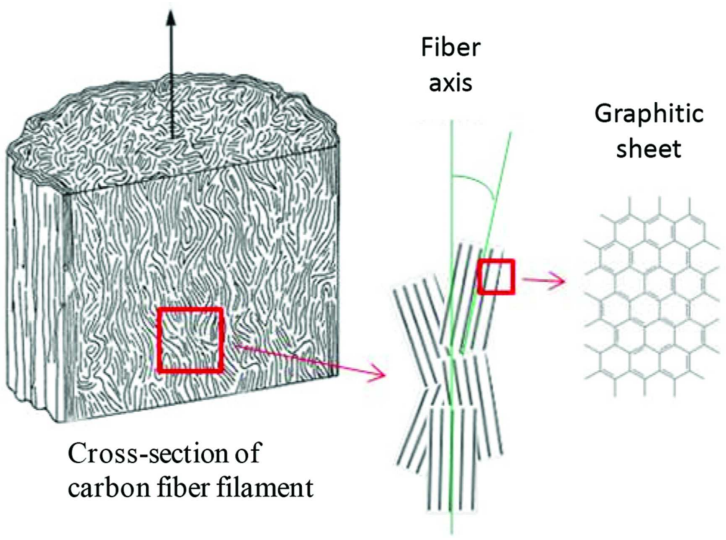

Figure 1.1: Carbon filament microstructure showing the atomic scale, the composition of a single filament and the cross section of said filament, reproduced from [1]

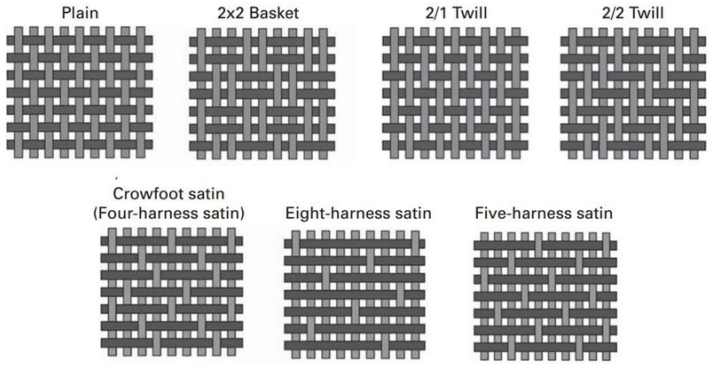

Figure 1.2: Weaving pattern for carbon fibre ply, reproduced from [2]

conform to the surface of the molds and crimp which is the length of the tow used to weave around its path. For the sake of simplicity in this work, we will consider all the plies to be balanced. This means that results should be independent from the number of plies above and below the sensor. We will also consider the plies to be isotropic in the plane of the weave.

The second part of the composite is the matrix, generally made of resin. It can be seen holding the fibres together on 1.3. Two broad category of resin can be discerned[10]:

- Thermosetting resins
- Thermoplastic resins

Thermosetting resins are generally liquid polymers with irreversible curing. This curing process may be affected by heat, chemical reaction or irradiation. Thermoplastic on the other hand can be reused by melting them back into liquid form. There mechanical properties vary more with temperature than thermosetting and thus may not be suitable for all application.

Table 1.1 presents a non-exhaustive list of available resin families. Care should be taken when choosing a resin as some additive can change its thermomechanical properties wildly.

Thermosetting	Thermoplastic
Cyanate ester	Polyamide
Epoxy	Polycarbonate
Phenolic	Polyetheretherketone
polyester	Polyetherimide
polyimide	Polyethersulfone
vinyl ester	Polypropylene

Table 1.1: Families of resin from both thermosetting and thermoplastic type used in CFC

Each resin family has different options for curing. A well-known resin is epoxy. It has multiple options available depending on the curing agent used. It can be cured at room temperature via a curing agent such as aliphatic polyamine, or via light with photo initiators. And of course, it can be cured with heat by using high temperature. The different curing method will be discussed more in depth in subsection 1.2.

1.1.2 CFC mechanical failure modes

There is multiple mode of failure in CFC, but generally the first to appear concerns the matrix. Whenever the fibres itself fail means the matrix has already failed either as a delamination or as a crack. This is because all resin used for the matrix have a lower ultimate yield strength than the fibre in their main direction. The only difference between the delamination and the crack is the direction of failure, as shown on figure 1.3. A delamination is a crack that propagates parallel to the plies while a matrix crack is perpendicular to the plies.

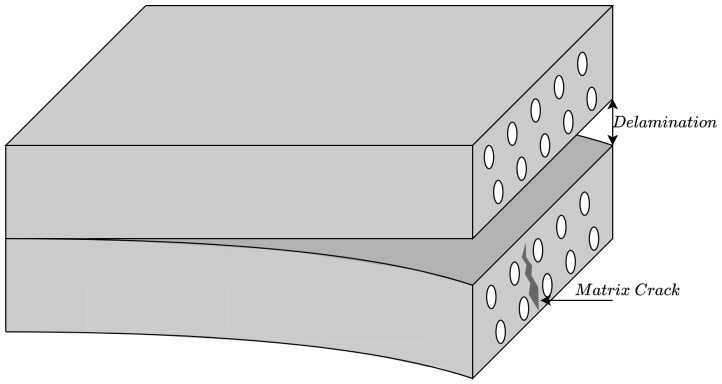

Figure 1.3: CFC showing matrix in grey and carbon fibre in white. Delamination and matrix crack in composites.

In this work, both matrix cracks and delamination may occur due to the insertion of a sensor inside the composite. In literature, sensors often generate delamination due to a mismatch of the coefficient of thermal expansion (CTE).[11]

1.1.3 CFC commercial use

Carbon fibres are used in a multitude of market due to their lightweight and high tensile strength properties.

	Elasticity Modulus [GPa]	Yield strength [MPa]	Ultimate strength [MPa]	Density $[\frac{g}{cm^3}]$	Price
Carbon Fiber Composite Injectex®G0926	67[1]	N/A	860[1]	1.551[1]	234$ per Kg*
Glass Fiber Composite S2 Glass	55.61[2]	N/A	2297[2]	2.46[2]	72.37$ per Kg*
Aluminium alloy 6063 Aluminium	68.9[3]	214[3]	241[3]	2.7[3]	N/A
Steel 316L Stainless steel	200[4]	205[4]	515[4]	8[4]	5$ per Kg
Oak Wood	9[5]	N/A	70[5]	0.704[5]	0.7$ per Kg

Table 1.2: Strength, stiffness and cost comparison of different materials.

[1] From reference [12]
[2] From reference [13]
[3] From reference [14]
[4] From reference [15]
[5] From reference [16]

One of the main users of CFC is the aerospace industry, given its necessity to reduce weight as much as possible. Currently Space X, the lowest cost orbital launcher quotes 2350$ to launch a kilogram of payload to orbit with their Falcon heavy vehicle. This means that despite the higher cost of CFC, and thus the higher final cost of the launch vehicle, the cost to launch weight in low earth orbit is reduced. It is very hard to obtain precise flight cost for aircraft but the general trend of having less dead weight is still applicable.

Another known industry using CFC, is the high-end sport car. In this industry, performance is paramount, giving CFC an edge over all other materials since its overall properties as seen in 1.2 are either the same or better than all other materials analysed.

CFC is also used for large sized windmill alongside glass fibre composite to reinforce the blades. The use of CFC is to reduce the number of windmills by having more efficient and bigger windmills justifying it's higher cost. Given the polluting nature of CFC manufacturing, many studies have been made to find a bio-composite with less impact on the environment[17].

Source	2022 Demand (Red and Zimm 2012)			2020 Demand (Industry Experts 2013)			2018 Demand (Lucintel 2012)		
Rank	Application	Tonnes	% of Total	Application	Tonnes	% of Total	Application	Tonnes	% of Total
1	*Wind*	*47,390*	*38.6%*	*Wind*	*36,350*	*25.6%*	*Aerospace*	*20,644*	*24.8%*
2	*Aerospace*	*21,370*	*17.4%*	*Aerospace*	*23,170*	*16.3%*	*Wind*	*14,837*	*17.8%*
3	*Pressure Vessels*	*11,200*	*9.1%*	*Automotive*	*22,620*	*16.0%*	*Automotive*	*12,613*	*15.2%*
4	Sporting Goods	8,390	6.8%	Other Industrial	17,730	12.5%	Molding Compounds	10,662	12.8%
5	*Automotive*	*6,200*	*5.0%*	Sporting Goods	12,310	8.7%	Sporting Goods	7,985	9.6%
6	Molding Compounds	5,280	4.3%	Molding Compounds	9,350	6.6%	Industrial Other	5,989	7.2%
7	Tooling	4,540	3.7%	*Pressure Vessels*	*9,340*	*6.6%*	*Pressure Vessels*	*5,808*	*7.0%*
8	Civil	4,300	3.5%	Civil	6,850	4.8%	Civil	3,584	4.3%
9	Pultrusion Misc.	4,090	3.3%	Oil and Gas	4,000	2.8%	Marine	1,044	1.3%
10	Misc. Consumer	3,920	3.2%						
11	Sailing/Yacht Building	2,320	1.9%						
12	Misc. Energy	2,010	1.6%						
13	Oil and Gas	920	0.7%						
14	Medical/Prosthetics	460	0.4%						
15	Industrial Rollers	390	0.3%						
	Total	122,780	100.0%		141,720	100.0%		83,167	100.0%

Figure 1.4: CFC estimated market share, reproduced from [3]

As we can see on table 1.4, pressure vessel is the third largest market for CFC. Instead of a traditional bulky and heavy stainless-steel tank, truck can haul a lighter CFC tank which is also resistant to corrosion. En demand in this market tends to vary widely depending on the estimator. The reasons being the cost of CFC makes it difficult to justify its usage when much cheaper steel is available. As for the fuel cost savings, it remains hard to justify such investment as the cost of oil which is used to produce fuel can vary very wildly from being negative in April 2020 to shooting up in the recent month.

Other markets exist such as the sport industry, many of the sports tools such as a tennis racket or a golf club are made of lightweight CFC. And while they do represent a non-negligible market share, there is little to no need for SHM.

SHM for aircraft would allow to reduce the maintenance cost and reduce the risk of catastrophic failures. For the spatial industry, the risk of rapid unscheduled disassembly due to a structural fault would be reduced. Wind blades set up with SHM could have reduced maintenance schedule and longer lifetime. Pressure vessel may benefit from SHM to detect potential weak point where leaks are likely to form and thus prevent them. Other industry may benefit from SHM, but their benefit may be marginal. One example would be the car frame, due to their very small thickness embedded sensor would add very little in terms of added value.

1.2 CFC fabrication methods and challenges

The manufacturing methods of carbon fibre are as diverse as its properties. As mentioned in the previous section, there are multiple methods of curing the matrix, this in turn leads to a wide variety of possible manufacturing method. All have advantages and disadvantages, but some create problems for the integration of sensors within the composites. For example, the CTE mismatch between the matrix and reinforcement during heat curing generates stresses

and deformation during the manufacturing process.

1.2.1 Open molding process

The open molding manufacturing process consists of using an open mold where the resin and reinforcement are deposited on it or in it. Then the cure can happen at ambient temperature or via autoclave. Here are some of the techniques used for open mold process.

Hand lay-up and wet lay-up

Hand lay-up and the very similar wet lay-up are the first processes used in the industry to manufacture composites.[18] The first step consists of spraying or coating the mold with releasing agent. Then each layer of reinforcement is applied by hand. In between each layer, resin is then coated via a roll and brushes. Wet lay-up uses prepreg plies instead of using dry carbon fibre plies. Prepreg plies are already coated in resin before their lay up in the mold. This technique has the advantage of being cheap and not requiring any trained personnel. Nevertheless, the production of each piece is time consuming, and the quality vary enormously from piece to piece. An alternative to hand lay-up is automated tape lay-up. Instead of having humans manually stacking plies upon each other, a loaded roller lay down tapes of uni-directional fibre unto the surface of the part.[19]

Spray lay-up

Spray lay-up is very similar to hand lay-up with the exception that both the resin and reinforcement are sprayed onto the mold. This requires a spray set up and is thus a bit more costly than hand lay-up. Another problem is that the layer thickness may not be as consistent as hand lay-up. Only chopped fibre can be used as reinforcement with this lay-up method, and often results in low fibre content of the finished product. In turn, the process of layering is much faster, reducing the labour cost.

Autoclave curing

As mentioned in the previous section, there are multiple curing options. For open molding process room temperature, heat curing, and photo curing are possible. For autoclave curing, once the reinforcement and resin have been applied to the mold, the mold is inserted in a vacuum bag which is then sealed. The vacuum will get rid of most of the trapped air bubbles within the resin. Afterwards the vacuum bag is placed within the autoclave. Then hot inert gas will apply pressure to cure and increase the density of the final product. This technique, while achieving very high fibre content with little amount of void, comes with a high cost. The equipment required for the autoclave is very expensive and it limits the maximum size of the final piece that can be manufactured.

1.2.2 Close molding process

As opposed to open molding processes, closed molding uses multiple piece which when put together form a closed mold. First the reinforcements are stacked into the different pieces of the mold which is then closed. Heat and pressure is then applied to cure the resin and increase the fiber weight ratio.

Resin transfer molding (RTM) and vacuum assisted RTM

In RTM, when the mold is closed with all the plies stacked together inside, the resin is infused via a small inlet. The resin diffuses through all the plies and piece thanks to pressure. This can be controlled to be either high, around 25 bar or lower, giving different resin impregnation times. Vacuum assisted RTM is similar but instead of having a press putting pressure on the mold and a piston pushing the resin within, the atmosphere pushed the resin into the mold and maintains the pressure on the vacuum bag.

RTM has quite a few advantages: It has a high throughput compared to open molding processes, allowing this technique to produce pieces much faster and thus reducing labour cost. It can achieve a high fibre ratio and produce a wide range of laminate thickness.[10] Nevertheless, it requires expensive tooling, making it justifiable only if many pieces are produced.

Preform molding process

Preform molding process also called sheet molding compound, is a process where the reinforcement and resin are placed within the mold which is then closed, compressed and heated for the resin to cure. This type of manufacturing is extremely fast and allows to eliminate the need of trimming after the molding step.[20] Nevertheless this process doesn't work very well for pieces with sections perpendicular to the compression direction. It also requires a specific steel mold for each specific part, making it only viable for high production volume or small pieces.

There are many others processes for composite manufacturing, but in the scope of this work only the processes requiring or having heat curing available are of interest to us.

1.2.3 Heat curing and resin glass transition

One of the main problems when introducing a foreign object into a composite with a resin that needs heat curing, is the stresses generated by the CTE mismatch. Many of the resin used in composite have high CTE, compare to the smaller coefficient of material such as silicon which are used for strain sensor as shown on figure 1.5.

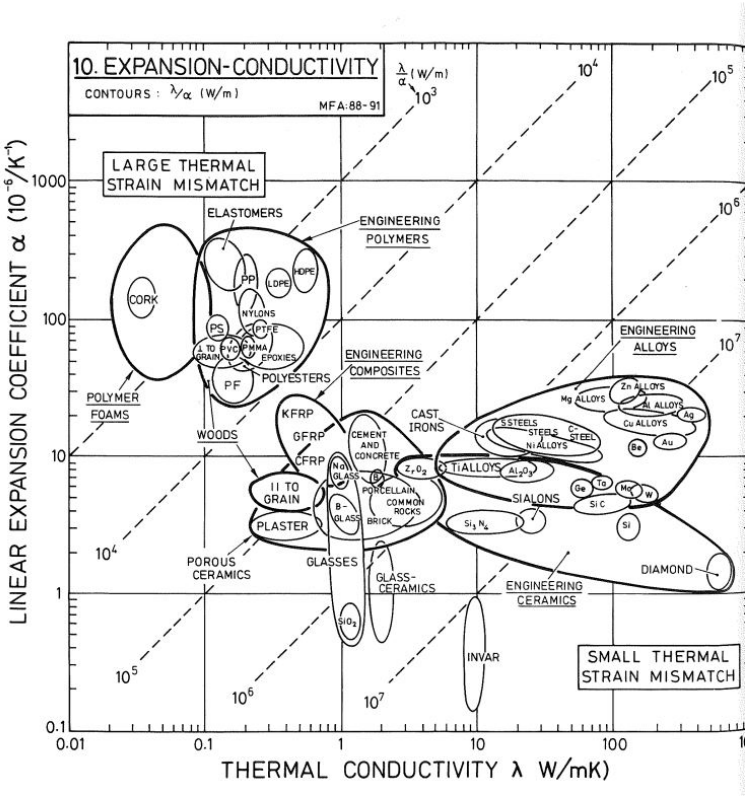

Figure 1.5: CTE properties of a wide range of materials, reproduced from [4]

This will give rise to big stresses on the sensor during and after the curing process. The stress will not appear during the beginning of the curing as the resin is still liquid. Instead, the stress will start appearing when the resin is cooling down. Another deformation phenomenon independent of temperature is the chemical shrinkage of the resin due to crosslinking.[21] The chemical shrinkage affects the resin regardless of whether it has been heat cured or not. Both CTE mismatch and chemical shrinkage apply stresses only after a certain degree of cure, as before that point the resin molecule can still move enough as to relax. During the cooling down of the resin, stresses will not appear immediately, this is due to the resin relaxation. As the resins cools down, the cross-linked polymer will deform to reach a lower energy state. Until it reaches close to the low energy state, the stresses generated will be negligible. This will be discussed more in detailed in chapter 2.

1.3 Review of strain sensors for embedded application

The integrated sensor will have to conform to certain restrictions, some imposed by the industry and others due to physical limitations. The first limitation is the maximum dimension of the sensor. As this work is a continuation of the previous master thesis, it will assume the same restrictions. The maximum dimensions for inclusions from Samuel Gilet master thesis[22] are set at 10mm for length and width, and 300 μm for depth. The second restriction is the power consumption of the sensor, as shown in [22], the power transmission

efficiency is low for integration at 1 and 2 ply depth.

The third limitation is the impact of the composite manufacturing process on the embedded sensor. This is not a problem for composite such as concrete or plywood as they only need the matrix to dry. CFC with matrix curing at ambient temperature are also easier to integrate with as only the chemical shrinkage will generate stress. The last restriction is the matching between the sensor maximum strain and the materials maximum strain. The sensor can have a strain range equal or greater than the housing material, but must never have a smaller range, otherwise the purpose of SHM is defeated. Other restrictions may be applied, but for this work, those are enough to narrow down the type of sensors viable for integration in CFC.

1.3.1 Piezoresistive strain sensor

The gauge uses the change of resistance generated by strain to measure said strain. The resistance change is given by equation 1.1.

$$\frac{\Delta R}{R} = \frac{\Delta \rho}{\rho} - \frac{\Delta A}{A} + \frac{\Delta L}{L} \tag{1.1}$$

Where ρ represent the resistivity of the material, A and L its cross-section area and length respectively. Two contributions can be identified

- $\frac{\Delta \rho}{\rho}$, the change of resistivity due to stress
- $-\frac{\Delta A}{A} + \frac{\Delta L}{L}$, the geometrical deformation

The sensitivity of a sensor, called the *gauge factor* can be obtained with the following equation:

$$GF = \frac{\Delta R/R}{\epsilon} \tag{1.2}$$

where ϵ is the sensor's strain. The contribution to the gauge factor allows to distinguish two main categories of gauge, being metallic gauge and semiconductor gauge.

Metallic gauges

Most metallic gauge rely on the geometrical deformation to measure strain; this limits their maximum sensitivity. This is not true for every metal as shown on 1.3 for Nickel but compared to semiconductor gauges they have lower gauge factor. Metallic gauges are generally of bigger size, this is due to their low resistivity. To obtain a reasonable resistance, they are made in a comb like pattern. Nevertheless, commercial strain gauges have high maximum strain. Constantan alloy strain gauges from BCM sensor have a strain limit around 30,000$\mu\epsilon$ compared to 5000$\mu\epsilon$ for their silicon counterpart.[23] Another advantage of metallic gauges is the large range of different metal and alloys available. This allows CTE matching between the composite and the gauge as shown on 1.5. A possibility would be to counteract the change of resistance due to the stress generated due to CTE mismatch by the change due to a temperature drift.

(1.3)

Semi-conductor gauge

Semi-conductor gauges rely on the resistivity variation due to stress to measure strain. This gives them a very high gauge factor and combined with their relatively small size, it makes them a very good candidate for integrated SHM. Unfortunately, their range of deformation is much lower, limiting the materials it can be integrated in. The most widespread material for semiconductor gauges is silicon. This limits the CTE matching with the composite material. The CTE mismatch and the smaller strain range will further limit the possibilities of integrating silicon gauge within composite. There are other semi conductor materials such as graphene and III/V materials which can be used for strain sensor application. A GaN thin film, which is a III/V material, has a gauge factor around 130.[24] Graphene strain sensors for SHM, have a gauge factor between 375 and 473.[25] The drawbacks of III/V and graphene are mostly their fabrication cost, especially compared to metallic and silicon gauges.

Special material gauges

There are special engineered materials to increase the sensitivity of a gauge. One such material, a heterostructure nanocrystal solid, has been used to achieve a gauge factor of 5045.[26] While many interesting properties may be achieved with those special materials, they are unlikely to be commercially available in the near future due to their complicated and expensive manufacturing process.

Material	Gauge Factor
Al	1.4
Cu	2.1
Ni	-12.62
Pt	2.60
Si(SC)	-102 to 135
Si(Poly)	-30 to 40

Table 1.3: Comparison of metal and semiconductors gauge factor, reproduced from [9]

1.3.2 Capacitive strain sensor

Capacitive strain sensors function similarly to piezoresistive gauge. They also measure the change in impedance due to the strain. The impedance of a capacitor is given by equation 1.4.

$$Z = \frac{1}{j\omega C} \tag{1.4}$$

ω is a parameter of the sensor circuitry, leaving only C. For the classical two parallel plate example, the capacitance can be computed as follow:

$$C = \epsilon_r \epsilon_0 \frac{A}{d} \tag{1.5}$$

Where ϵ_r represent the relative permittivity of the material between the two plates, A represents the area of the plates and d represents the distance between the two plates. Capacitive strain sensors exist in many forms to exploit either a change in area, a change in distance or both as shown on figure 1.6.

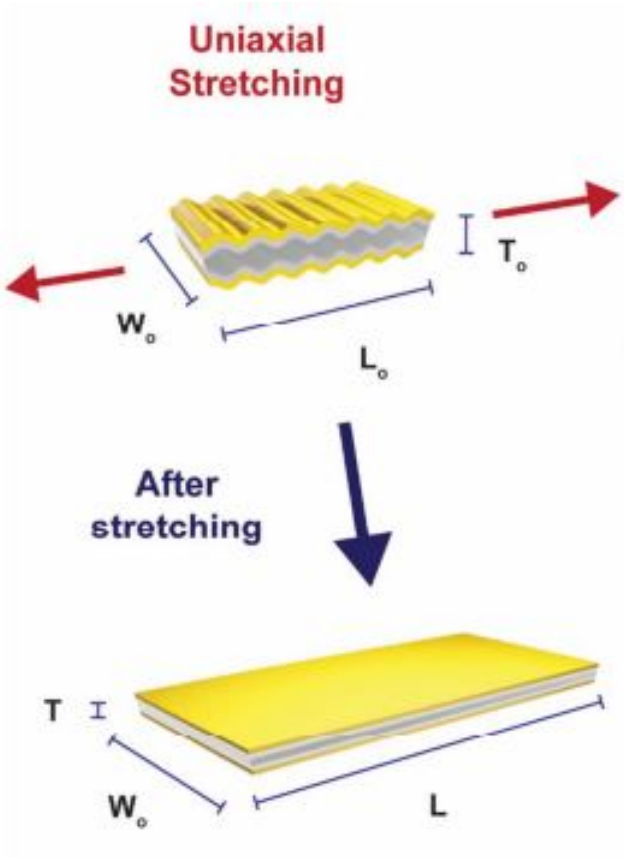

Figure 1.6: Crumpled gold foil capacitance, reproduced from [5]

Capacitance strain sensors cover very wide ranges of strain. The gold thin foil from [5], can support up to 140% deformations. It is also very linear over that big strain, but this comes at the cost of very poor sensitivity. Gauge factors found in the literature vary from 2 to 6.[5, 27, 28] Another advantage is the very low power consumption. Some systems have been powered via RFID.[29] They are a very good contender for SHM, but are more suited for materials which can deform more easily than CFC.

1.3.3 Optical strain sensor

Optical strain sensors come in the form of fibre Bragg gratings. Fibre Bragg gratings function by creating a periodic pattern in the optical fibre refractive index. This periodic pattern reflects a specific frequency band, which depends on the distance between each refractive change. Should the pattern periodicity change due to strain, then the reflected frequency will change accordingly.

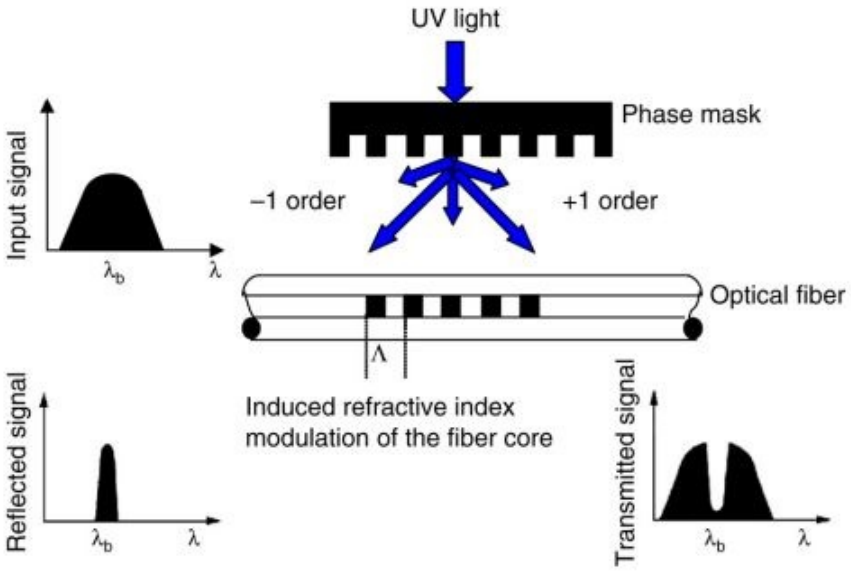

Figure 1.7: Fiber Bragg grating manufacture and working principle, reproduced from [6]

Optical fibre have many advantages, being their robustness against electromagnetic interference and their precision. They also have their disadvantages, being that optical fibre have diameter in the range of 100 microns due to cladding. This makes them less attractive in SHM compared to the piezoresistive sensors which can have a thickness of ± 40 microns. Not only are they thick, but they also require complex and bulky equipment to analyse the fibre output, making them ill-suited for embedded applications. Said equipment also have high power consumption in the order of watts. Optical fiber were also shown to weaken the compressive strength of the composite they are embedded in by nearly 40%[30].

Despite all those disadvantages, fibre Bragg grating are the most used strain sensors in literature for embedded monitoring in CFC, whether in-situ monitoring[31] or internal monitoring[32, 33].

The optical fibre used for monitoring, meshes well with the carbon fibres and are able to support the stress from the shrinking resin. The sensors electronics is outside of the composite due to its size, nullifying any worry about temperature frying the electronics.

1.3.4 Piezoelectric strain sensors

Piezoelectric sensors exploit the properties of some materials to generate charge density on their surface orthogonal to the applied deformation. The two most common materials used for piezoelectric sensors are lead zirconate Titanates (PZT) and polyvinilidene fluoride (PVDF). PZT has a much higher piezoelectric coefficient but is much stiffer than PVDF.[34] Piezoelectric sensor are very simple to set-up but comes with durability issues, especially for piezoelectric wafer active sensors. Sensors subjected to environmental temperature variation showed signs of delamination[35], and those subjected to low velocity impact while embedded in a composite cracked before the composite showed damage.[36]

Type	Model	Size	GF or sensitivity	Price per unit	Manufacturer
Metallic piezoresistive	CEA-05-250UWA-350	14x6.9x??mm	2.07	20 €	Micro Measurment
	1-LY19-6/350A	13x6x0.075mm	±2	12 €	HBM
Semiconductor piezoresistive	BPY-1000-2.6-UIRL	6x4x0.07mm	150	Unknown	BCM sensor
Fiber bragg interogator and optical fiber	1-FS22DI-ST/4CH T100 FBG array	$\varnothing = 0.25mm$ $L = 8mm$	$1.2\frac{pm}{\mu\epsilon}$	17000 €	HBM and Technica
Piezoelectric	T220-A4BR-1305YE	32x12.7x0.5mm	$0.33\frac{V}{\mu\epsilon}$	239.80 $	Piezo.com

Table 1.4: Commercially available strain sensor

1.4 Literature review of embedded sensor in composites

The concept of embedding sensors into resin or composites is not new to the literature. Already in 1992, Ki-Soo Kim, Menachem Breslauera and George S. Springer were already studying the effect of embedded sensors on the composite strength[37]. While this works focusses specifically into CFC, other composites such as concretes, metal laminates, glass fiber reinforced plastic, and others have also been studied.

1.4.1 Optical embedded sensor

When optical sensor is mentioned in embedded sensor, most of the literature will refer to Fiber bragg grating. But other sensor such as the Fabry–Perot interferometer exist and have been used as embedded sensor[38]. Both technologies use optical fiber, Fabry-Perot uses either one or two depending on whether an Explicit Fabry-Perot interferometer or an intrinsic Fabry–Perot interferometer configuration is used. Table 1.5 shows a non-exhaustive list of studies done with embedded optical sensor in composites.

In the sensor dimension, the diameter of the whole fiber optic, core, cladding and coating(s) is considered. As for the length, either it is the length of the whole embedded optical fiber when given or only the part containing the fibre bragg grating.

In most studies, the residual strain due to the manufacturing step is often skipped over. Another potential figure of merit that is often not mentioned is the power consumption of the samples. The power consumption is mostly dependent on the interrogator used. Another noticeable point is the size of the composites which are generally small compared to real composites pieces such as airplanes wings or windmill blade. The geometries of all samples from the articles in table 1.5, are simple stacked sheet.

1.4.2 Embedded piezoresistive and piezoelectric strain gauge

Other types of sensors have also been studied for their integrations within composites. The two most common is the piezoresistive and piezoelectric sensors. For the piezoresistive, the focus of most studies is the low impact of the embedded sensor on the composites. Table 1.6 shows a non-exhaustive list of studies on embedded piezoelectric and piezoresistive sensors.

Glass fiber is used more often than for optical sensor, this is mostly due to the conductive property of carbon fiber making it more complicated to integrate piezoresistive sensors without shorting them. And since as shown in table 1.2, glass fiber is cheaper than carbon fiber, the samples are generally bigger compared to what is shown on table 1.5. The absence of semiconductor strain gauge is quite noticeable, indeed there exist many commercial metallic strain gauges but semiconductor strain gauge are much rarer. The only one found was from BCM sensor, while others have been found to also sell semiconductor gauge, they are suspiciously similar to the BCM one.

1.5 Scope of this work

During the first chapter, the different combination of sensors and CFC were showcased. Showing the immense number of possibilities available. Since our work is a continuation of Samuel Gilet master thesis[22], we maintain the same constraints in term of size and power consumption. This limits the choice not only in sensors but also in CFC, since the aero-spatial industry only take validated combination of resin and carbon ply.

The initial objectives of this work were the thinning and better integration of sensors into composites. During the literature research, it shifted to the following point. First, finding a simplified model to get a close approximation of the residual stress. Second, finding the different parameters and their impact on the residual stress of the sensor. Those will be compared with experimental data from two samples. To do this we will limit ourselves to the RTM6 epoxy resin from Hexcel for the material properties and two specific strain sensors. The works should remain valid for other materials simply by replacing the material properties. Many studies have been done in literature on the integration of strain sensor into composite. While most of the studies uses optical sensor such as fiber Bragg gratings, many others show the potential of nano carbon tube as a non-intrusive sensor. There have been investigations on when and how the residual strain appears and to what physical phenomenon they are linked but rarely a quantitative analysis.

At UCL, previous works have been done to develop the ability to embed sensor into CFC and to interrogate it wirelessly. The first work was done by Samuel Gilet on developing the models for wireless transfer of energy and information through carbon fiber plies. The second work was done by Nicolas Roisin, into developing an extremely low power strain gauge to embed into CFC.

Type of sensor	Materials monitored	Composites dimension	Sensor dimension	Goal of the study
EFPI, FBG	Carbon fiber reinforced plastic	240x240x20mm	∅ : NaN L :120 mm	Demonstration of EFPI and FBG for SHM in CFC [38]
FBG	Carbon fiber reinforced plastic	??x??x10.3mm	$\varnothing : 145 \pm 5\mu m$ L : NaN	Development of smart embedded sensor for condition based maintenance in composite. [39]
FBG	Carbon fiber reinforced plastic, epoxy adhesive Araldite 420 A/B	107x24 x1.2mm	$\varnothing : 245 \pm 7\mu m$ L : NaN	Feasibility of using Fiber bragg grating for strain monitoring in bonded region. [40]
FBG	Carbon fiber reinforced plastic	230x50mm 10 plies	∅ : NaN L : NaN	Monitoring of cure with Fiber bragg grating. [41]
FBG	Unidirectional Carbon fiber reinforced plastic	100x20x1.5mm	∅ : NaN L : NaN	Improving the accuracy and reliability of FBG in unidirectional composites.[42]
FBG	AS4/3501-6 unidirectional carbon/epoxy prepreg tape	254x12.7mm 114.3x12.7mm 8 or 16 plies	$\varnothing : 145\mu m$ L : NaN	Composites mechanical failures due to embedded fiber optic. [30]
FBG	Carbon fiber reinforced plastic S160-REM, Seal	50x15x1mm 8 plies	$\varnothing : 242 \pm 5\mu m$ L : 5, 10 mm	Evaluation of the coating and length of the fiber bragg grating on the polymer. [43]
FBG	Carbon fiber and glass fiber reinforced plastic, metal laminates	250x25mm 2,4,7,8 plies	∅ : NaN L : NaN	Variables impact on final FBG spectrum analysis. [44]
FBG	Carbon fiber reinforced plastic T800H/3631	NaN	$\varnothing : 250\mu m$ L : 10 mm	Detection of transverse crack in CFC.[45]

Table 1.5: Non selective list of studies in Optical sensor embedding in composites.

Type of sensor	Materials monitored	Composites dimension	Sensor dimension	Goal of the study
Piezoelectric	Glass fiber reinforced plastic	360x250x3mm	25x25x0.25mm	Feasibility of using piezoelectric for crack detection. [46]
Piezoelectric	Glass fiber reinforced plastic	100x25.4mm 8 plies	$\varnothing = 7mm$ t=0.2mm	SHM of composites with PZT sensors. [47]
Piezoelectric	Glass fiber reinforced plastic	80x80x10.4mm 600x500x3.31mm	$\varnothing = 20mm$ t=1mm	In situ measurment during cure and SHM with contactless sensors.[48]
MEMS Piezoresistive	Glass fiber reinforced plastic Fiberite 7781	63.5x305mm t=2-12.2mm	10x10x0.5mm	Evaluation of MEMS strain sensors in composites.[49]
Piezoresistive	Carbon fiber reinforced plastic	250x25x1.15mm	20x3x0.045mm	Presentation of a nano composite piezoresistive sensor for In situ monitoring. [50]
Piezoresistive	Concrete	Unknown	Unknown	Review of cement based sensor with carbon nano tube.[51]
Piezoresistive	Epoxy/flax bio composites	Unknown	$A = 0.5cm^2$ t=1.75μm	Smart bio composite using nano composite sensors.[52]
Piezoresistive	Carbon/glass fiber reinforced plastic	300x300x2mm	$\varnothing = 0.178mm$ L=150mm	SHM for composites with carbon nano tube. [53]
Piezoresistive	Glass fiber reinforced plastic	180x15mm 10 plies	100x100mm $t = 0.67 - 1.67\mu m$	SHM for composites with carbon quantum piezoresistive sensor.[54]

Table 1.6: Non selective list of studies on piezoresistive and piezoelectric embedded sensor in composite.

Chapter 2

Analytical model and properties estimation

In this chapter, different models to estimate the residual strains will be shown. First the simplest model with its hypotheses is presented, then it is refined by using a more advanced model with more accurate hypotheses. Afterwards the advanced model's parameters are sweeped to observe their sensitivity on the residual strain. Thereafter an explanation on how the material's properties were simplified for the previous model is given. Then the glass transition temperature is studied in more details to give a better insight into how the process can affect the residual stress. Finally, two models are shown to compensate for the temperature output of a silicon strain gauge and a commercial metallic strain gauge.

2.1 Stress in layered material

2.1.1 Target geometry

To model the stress due to the integration of a sensor within a composite, a good knowledge of the geometry is required. The geometry will vary with the sensor shape, the way it is embedded in the composites and the manufacturing process. In this work, the manufacturing process is not studied. As for the sensor shape, it is studied more in depth in chapter 3, where different geometries available in commercial strain gauge are simulated. Finally for the embedding, the simplest deposition between two plies is studied. There exists other method to embed a sensor such as cutting a hole in one of the plies and placing the sensor in it but they will not be studied here.

Unfortunately, in the literature, there are very few images of the internal structure of a composite with a square sensor embedded in. The reason is present in chapter 1, where most of the research focus on either optical fiber or carbon nanotube. An image of an embedded optical fiber is available in [30]. Figure 2.1 shows two embedded sensors and their impact on the composites. The curvature of the reinforcement fiber is nontrivial and as shown can be influenced by other defects. One of those defects is the voids of resin, little pocket where the resin didn't flow properly in, another one can be another sensor or a contaminant such as dust. The curvature will dictate how big the resin pocket around the sensor will be.

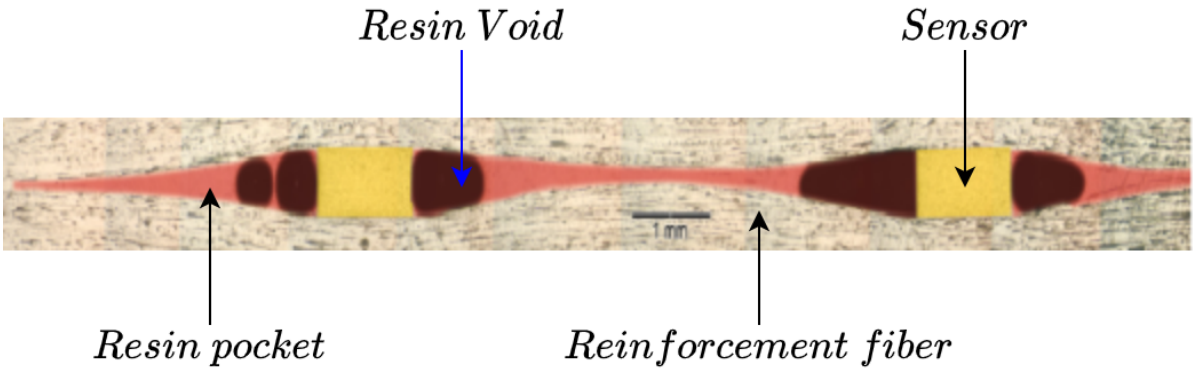

Figure 2.1: Embedded sensors in CFC, reproduced from [7]

2.1.2 Bi-layer model

When two materials with different CTE are layered upon each other like in 2.2 and one of them has a negligible thickness compared to the other, the stress they will generate when the temperature change can be approximated by:

$$\sigma = E(\alpha_1 - \alpha_2)\Delta T \tag{2.1}$$

Where E is the Young's modulus of the thin layer, α_i are the coefficient of thermal expansion of each layer and ΔT is the difference between their rest temperature and the current temperature.

Figure 2.2: Bi-layered material geometry

While being very easy and fast to use, it only gives an approximation under certain hypothesis. This model completely neglects the stress generated by the chemical shrinkage of the resin. The hypothesises are the following:

- The temperature is the same in all the spatial dimension.
- The deformation is an elastic deformation.
- The only component in the composite which will generate stress on the sensor is the resin.
- The sensor is on the surface of the composite.

- The upper layer is much thinner than the substrate.(Stoney's approximation)

The first hypothesis is acceptable especially at the end of the curing cycle. During the curing, due to the exothermic nature of the reaction, the temperature may not be completely homogeneous in the composite. But with good control over the overall temperature in the mold during the whole process and the relatively thin samples, this hypothesis should only introduce a minimal error.

The second hypothesis consider that the deformation generated by the thermal shrinkage is smaller than the elastic limit of silicon. The difference in density between the liquid uncured resin and the solid cured resin is given as $\frac{\Delta V}{V} = -0.046$ in [55]. For a cube of resin, each of the side would shrink by approximately 1.5%.

$$\frac{\Delta V}{V} = -0.046 \rightarrow C_1^3 - C_2^3 = -0.046 C_1^3 \rightarrow C_1 = 0.9852 C_2 \tag{2.2}$$

This is equivalent to a strain of around $1500\mu\epsilon$ which is lower than the BCM sensors strain limit of $5000\mu\epsilon$ but higher than the working strain. We are still in an elastic deformation, but we are out of the linear sensing range. Two simple ways to compensate for this, is to pre-strain the sensor in tension to cancel out the compression. Or to shift the zero strain to the residual strain of the manufacturing.

The third hypothesis consider the impact of carbon fibre ply to be negligible on the sensor strain. Considering the very small CTE mismatch between the sensor material and the carbon fibre, this hypothesis will only generate a small error. If a sensor material with a greater CTE mismatch is chosen, then this hypothesis may not be usable anymore.

The fourth and last hypothesis is the most problematic one, since the goal of this work is to determine the feasibility of embedding a sensor into CFC. Unfortunately, there are no analytical model for a sensor completely embedded into CFC as the generated geometry is nontrivial. Instead, finite element methods are used to obtain a more accurate estimation of stress, and even then, the geometry studied is still approximative.

2.1.3 Multi-layer model

To get a better estimation of the stress, the model of Chun-Hway Hsueh[8] will be used. This model computes the normal stress in a multi layered structure with a substrate under thermal strain and external bending. In the article two solutions are given, one with Stoney's approximation[56], where the layers are much thinner than the substrate, and one without. For the current application, the solution without Stoney's approximation will be used.

In our case the curvature radius will be set to infinity as there are no external bending applied.

$$r \rightarrow \infty \tag{2.3}$$

There will be only three layers, two made of resin with a thickness of $300\mu m$ which is considered to be the thickness of a ply and a layer made of the sensor material with the sensor thickness. This of course can be modified to study multi plies system. The stress for a given layer is given by the following equation:

$$\sigma_i = E_i(\epsilon - \alpha_i \Delta T) \tag{2.4}$$

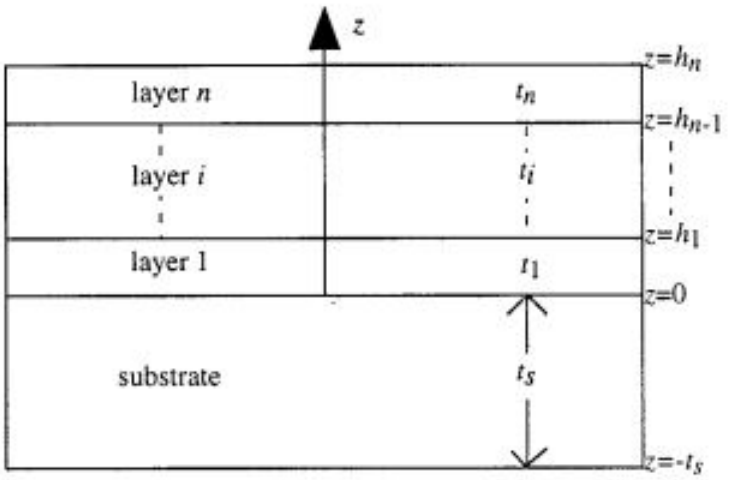

Figure 2.3: Coordinate system of multi-layer strip, reproduced from [8]

ϵ is the strain in the system and is given by

$$\epsilon = c + \frac{z - t_b}{r} \tag{2.5}$$

With the curvature radius set to infinity, it becomes:

$$\epsilon = c \tag{2.6}$$

Since the third layer has the same thickness as the substrate, the solution for c is

$$c = \frac{(E_s t_s \alpha_s + \sum_{i=1}^{n} E_i t_i \alpha_i)\Delta T}{E_s t_s + \sum_{i=1}^{n} E_i t_i} \tag{2.7}$$

The stress is thus given by

$$\sigma_i = E_i \left(\frac{(E_s t_s \alpha_s + \sum_{i=1}^{n} E_i t_i \alpha_i)}{E_s t_s + \sum_{i=1}^{n} E_i t_i} - \alpha_i \right) \Delta T \tag{2.8}$$

From this equation, the stress is influenced by three parameters.

- The temperature differential.(Process dependent)
- The thermal coefficients and Young modulus.(Material dependent)
- The layers thickness.(Geometry dependent)

By fixing some of the parameters, a sweep can be performed to understand the dependency of stress. In figure 2.4, three layers are used, two layers of resin sandwiching a single layer of silicon. The properties used for figure 2.4 are shown in table 2.1.

Before analysing the result, it is important to note that while this model is closer to the case of an embedded sensor, there are still some discrepancies between the embedded model

	Young modulus E	CTE α	thickness mm
Layer 1 Resin	2.51GPa	Variable to T $[62, 68.4] * 10^{-}6$	$300\mu m$
Layer 2 Silicon	170GPa	$2.1 * 10^{-}6\frac{1}{^{\circ}C}$	Variable
Layer 3 Resin	2.51GPa	Variable to T $[62, 68.4] * 10^{-}6$	$300\mu m$

Table 2.1: Computation parameters of figure 2.4

and this model. From the new model, the sensor thickness starts to have an impact on the normal stress within the sensor as shown on figure 2.4. Thinner sensor generates more stress than thicker one, while this may push for thicker sensor, this model does not take the impact of the sensor on the composite integrity. If care is not taken, a thicker sensor which generate less stress may have a lower production yield than a thinner sensor with higher stress.

This covers the variation in the geometry of the sensor and the process. On figure 2.5, the variation of the sensor material can be observed. Table 2.2 holds all the parameters which have been used for the sweep.

	Young modulus E	CTE α	thickness mm	Temperature Differential
Layer 1 Resin	2.51GPa	$68.4 * 10^{-}6\frac{1}{^{\circ}C}$	$300\mu m$	$\Delta T = 160^{\circ}C$
Layer 2 Materials	Variable	Variable	$40\mu m$	
Layer 3 Resin	2.51GPa	$68.4 * 10^{-}6\frac{1}{^{\circ}C}$	$300\mu m$	

Table 2.2: Computation parameters of figure 2.5

Figure 2.5 shows an interesting evolution of the stress. A very soft sensor would see it's stress decrease rapidly, but as the sensor becomes stiffer, the stress increase starts to slow down heavily. This trend favours softer sensor just as much as sensor who have matching CTE As shown on table 2.2, the composite stack is quite thin, as it is only comprised of two layers around the sensor. In the next figure, the same parameters will be used but the thickness of each layer of resin will be increased to simulate the effect of a 20 plies composite.

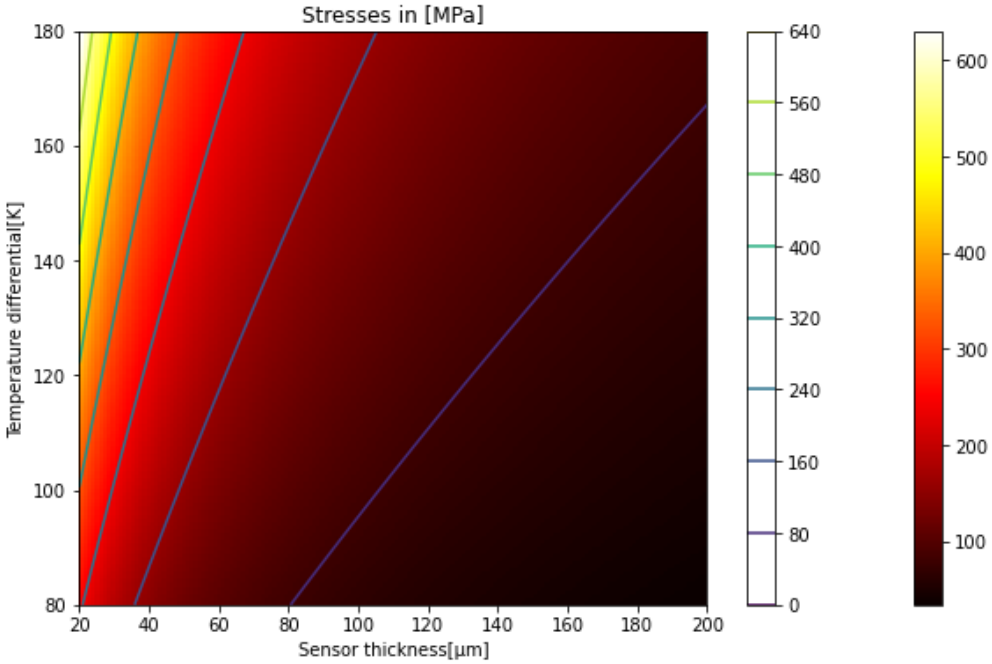

Figure 2.4: Stresses in the sensor.

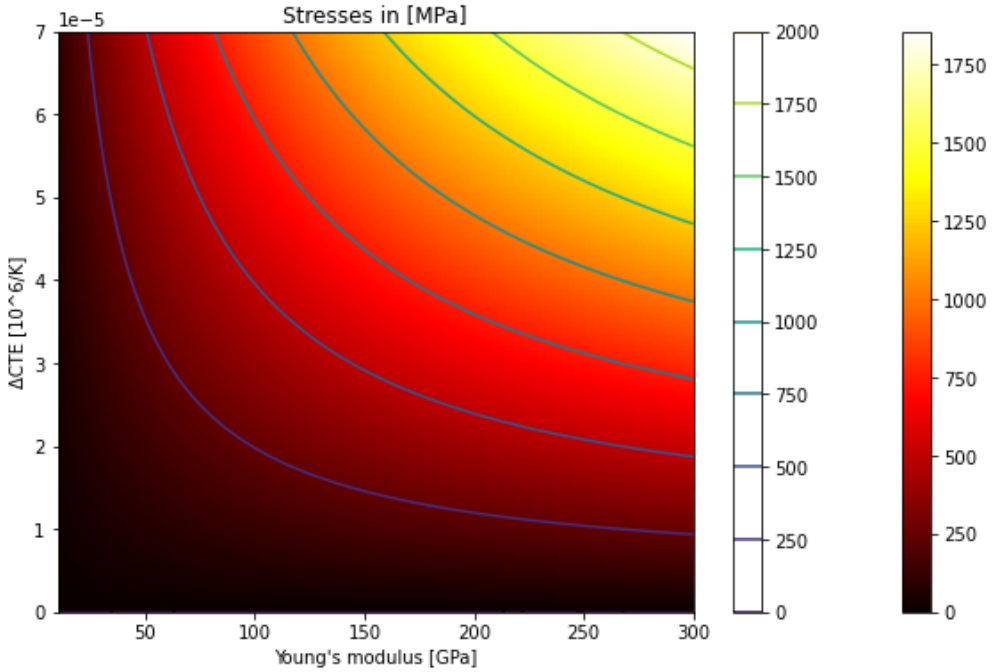

Figure 2.6: Stresses in the sensor with 3mm thick resin layer on each side.

Figure 2.6 takes the same parameters as figure 2.5, except both layers 1 and 3 have their thickness increase to $3000\mu m$ or $3mm$. The result of increasing the layer thickness of the resin is an overall increase in the generated stress and a increase in the sensitivity of stress to the

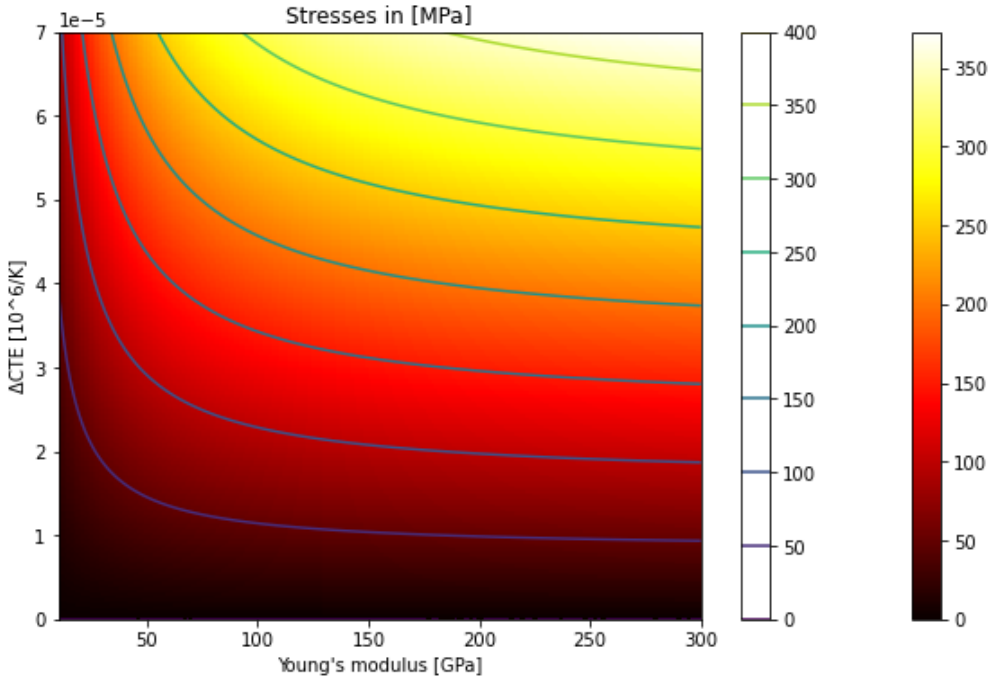

Figure 2.5: Stresses in the sensor.

sensor Young's modulus. For thick laminates the CTE matching becomes just as important as a low Young's modulus.

Interestingly, the depth at which the sensor is embedded has no impact on the stress in this model. Indeed, regardless of the thickness of the layers above or below, they remained summed in way that makes them indistinguishable. Only the total thickness, as shown with the difference of figure 2.6 and 2.5, has an impact on the generated stress.

2.2 Resin curing modelling

In the previous estimation of stress, we considered the resin to be a solid. This is only true when the temperature of the resin is below T_g for it's given degree of cure. The states during the curing are a bit more complex, the resin can be a liquid, a gel or a solid. The state depends on both the degree of cure and the temperature, with the degree of cure being itself dependent on the temperature history of the resin. Universally, the resin is liquid at the beginning of the curing process, this will change when the cross linking of the molecules has reached a certain stage, which is called the gel point.

The gel point is generally defined as the moment of formation of an infinite network preventing flow. One of the consequences of the infinite network is the dramatic increase in the resin viscosity. After the gel point, the resin has viscoelastic properties. A viscoelastic material exhibit both an elastic and viscous behaviour at the same time. This means that strain is not only dependent on the stress applied but also of the time of the applied stress. In practice this means that even after the gel point, there will be little to no stress applied

on the embedded sensor. As stress will result in a plastic deformation of the resin and a relaxation. At some point during the curing, the glass transition temperature will increase beyond the temperature of the resin. When this happens, the resin will transition from a rubbery gel to a glassy solid. It is in this glassy state that most residual stresses will be appear.

2.2.1 Degree of cure modelling

Since nearly all the resin properties are dependent on the degree of cure, we will need a model able to predict the degree of cure throughout the curing. There exist multiple models for the cure kinetics for thermosets, one such model is the Karkanas and Partridge[57] model. The Karkanas and Partridge model is a mix between nth order model and an autocatalytic model, making it a very suitable model for the RTM6 resin we are using. The equation is as follow:

$$\frac{\partial x}{\partial t} = A_1 e^{\frac{-E_1}{RT}}(1-x)^{n_1} + A_2 e^{\frac{-E_2}{RT}} x^m (1-x)^{n_2} \tag{2.9}$$

Where

- x is the degree of cure. $x \in [0, 1]$.
- R is the universal gas constant with the following value. $(8.3144 \frac{J}{mol\ K})$.
- $A_1,\ A_2$ are the pre-exponential factor.
- $E_1,\ E_2$ are the activation energies in $\frac{J}{moles}$.
- $m,\ n_1,\ n_2$ are the power.

The numerical value of those parameters is extracted from experiments. This has the disadvantages of having set of parameters only suitable for a specific resin. Requiring a new experiment for any new type of resin even if they are in the same family as an already known and characterised resin.[58, 57] Not only that but the same resin can have wildly different numerical values as shown on table 2.3 Care should be taken when analysing the result of the simulation. Additional external factor such as the method and time of storage of the resin before being used can also have an impact on the curing of the resin.

	B. Wucher[55]	G. Struzziero[59]
A_1	2.6e4S^{-1}	2.93e5S^{-1}
A_2	5.78e4S^{-1}	1.23e5S^{-1}
n_1	0.449	3.96
n_2	1.786	1.61
E_1	7.469e4$\frac{J}{mol}$	8.149e4$\frac{J}{mol}$
E_2	5.837e4$\frac{J}{mol}$	6.423e4$\frac{J}{mol}$
m	1.217	1.15

Table 2.3: The model constant given by different sources.

The gel point, as defined in [55], is indicated by the black lines on figure 2.7, as for the glass transition it can be seen on figure 2.9.

With the numerical value obtained from [55], and the cure cycle extracted from [60], the cure evolution on figure 2.7 is obtained.

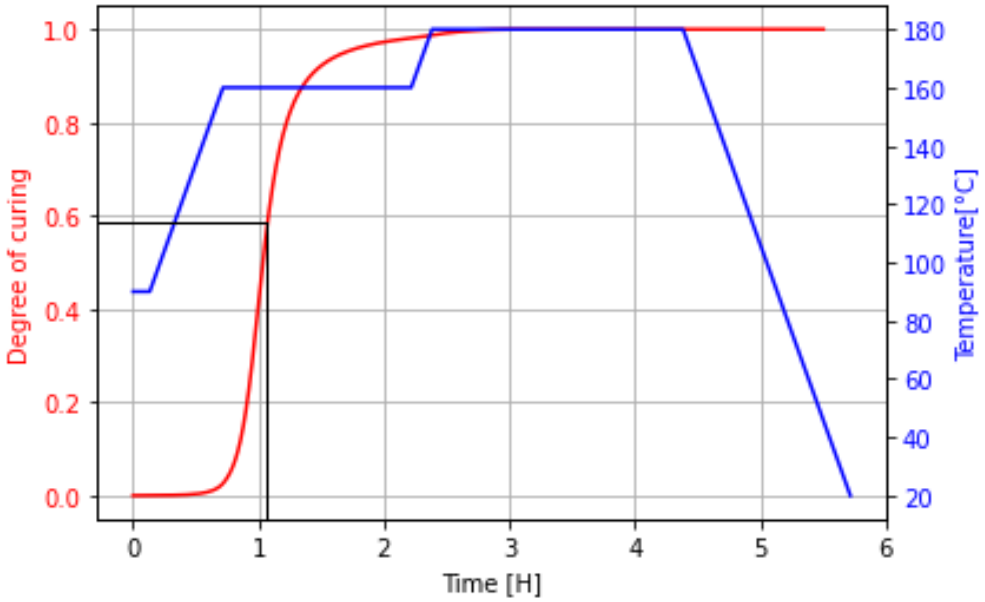

Figure 2.7: Degree of cure and curing cycle with the gel point shown by the black lines.

The method used to integrate 2.9 is a Runge-Kutta method, more precisely, the Cash Karp method. The time steps were dynamically chosen with a maximum step size set at 60 seconds. The code in python used for the computation is available in the annex.

2.2.2 Properties approximations

Up until now, only the shrinkage due to CTE has been considered. But for epoxy resin there exist another type of shrinkage which already mentioned in chapter 1, chemical shrinkage. As the polymers starts to cross-link, the volume it occupies shrinks. For the RTM6, the overall volume shrinkage can vary from 2% to 7% the initial volume[55, 61, 62].

Often, chemical shrinkage is characterised as either linear, quadratic or bi linear.[55, 21] Often a inflexion point is observed near the gel point, but as already mentioned, only the shrinkage occurring after the vitrification point is of interest. This allows us to take a linear model for the evolution of the chemical shrinkage.

Since part of the chemical shrinkage occurs before the gel point and another part occurs before the glass transition, only the small part occurring after the glass transition will generate non-negligible residual stress. The overall generated strain by chemical shrinkage is given by equation 2.10

$$\epsilon_{chemical} = (1 - x)\beta \tag{2.10}$$

Where β is the chemical shrinkage factor, for RTM6, its value is taken as -0.015[55]. Since both the chemical shrinkage and the glass transition temperature are dependent on the degree

of cure, the fraction of shrinkage occurring during the glass transition can be computed by knowing for what degree of cure the glass transition occurs.

The CTE also changes with temperature. The evolution of CTE with the temperature follows equation 2.11, when the temperature is below the glass transition temperature.

$$\alpha(T) = 54 * 10^{-6} + 0.16 * 10^{-6} T[\frac{1}{K}] \tag{2.11}$$

Where T is the temperature in degree $°C$. Since in this work we are interested in the residual stress and strain from the curing and not from an intermediate point, we can average the value of the CTE between the maximum curing temperature and the room temperature without introducing any error. The maximum value of the CTE is the glass transition temperature, since the asymmetry between the heating expansion and cooling expansion disappear for higher temperature. It is with this average value that all stresses will be computed with.

$$\alpha_{avg} = \frac{\alpha(T_g) + \alpha(T_{ambient})}{2} \tag{2.12}$$

Another important detail is the variation of the Young's modulus with temperature and degree of cure. Most assumptions about the stress appearing after the glass transition temperature are based on the change of the Young's modulus through the different phase of the resin. Even then the Young's modulus still change even when the resin has become a glassy solid. Its evolution can be seen on figure 2.8. To simplify the computation, we will take an

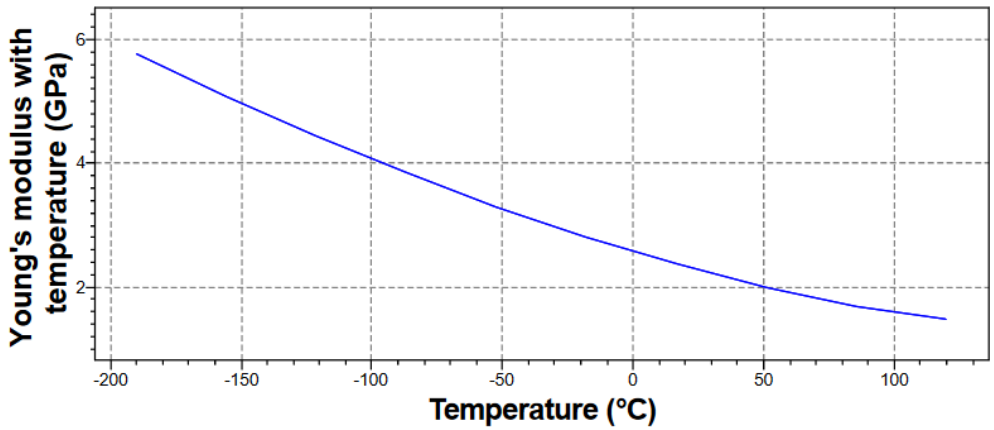

Figure 2.8: Resin's Young's modulus Vs temperature. Image used courtesy of ANSYS, Inc.

average value since only the final result of stress is important to us. We can estimate the error made by approximating the Young's modulus as an average value, by comparing it to the value when integrating the Young's modulus over the temperature range.

$$e = \left| \int_{T_0}^{T_f} E(T)(\alpha_1 - \alpha_2) dT - E_{avg}(\alpha_1 - \alpha_2)\Delta T \right| \tag{2.13}$$

Stress computed with an average Young's modulus $[\frac{N}{m^2}]$	Stress computed with an integrated Young's modulus $[\frac{N}{m^2}]$	Absolute error$[\frac{N}{m^2}]$ Relative error[%]
-30594533	-30649383	54849 0.17

Table 2.4: Stresses in the resin due to Young's modulus approximations.

The results from table 2.4 are obtained with following parameters:$\alpha_1 = 2.6 * 10^{-6}$, $\alpha_2 = 81 * 10^{-6}$ and $\Delta T = 155°C$. From those result, we can safely approximate the Young's modulus with the average value between room temperature and the maximum temperature of curing.

$$E_{avg} = \frac{E_{T0} + E_{Tmax}}{2} \tag{2.14}$$

The heat capacity of the RTM6 resin also change with temperature and cure. The dependency of the heat capacity on temperature are in the order of a few percent for every 30 degrees $°C$ and are very linear. Similarly, to the Young's modulus, the average can be taken while introducing only minimal error.

2.2.3 Glass transition temperature

Since most of the stress occurs after the temperature drops below the glass transition point, the crossing point needs to be accurately estimated. The glass transition temperature evolution over the degree of curing is given by the DiBenedetto equation shown on 2.15.[63]

$$T_g = T_{g0} + \frac{(T_{g\infty} - T_{g0})\lambda x}{1 - (1 - \lambda)x} \tag{2.15}$$

The value of T_{g0}, $T_{g\infty}$ and λ are fitted for a specific resin type. For the RTM6, the numerical values are, -11, 206 and 0.435 for T_{g0}, $T_{g\infty}$ and λ respectively taken from [55].

This equation combined with the Karkanas and Partridge model, allows us to estimate when the resin goes through the glass transition if the curing cycle is known. A few assumptions are made, the first is that the temperature throughout the curing and the resin is homogeneous and equal that of the curing oven. This is true in thin pieces of composites and resin, if the temperature changes slowly. The second assumption is that the heat of enthalpy of the cross linking reaction is dissipating fast enough that no heat pocket is created. By combining the previous result in 2.7 with the DiBenedetto equation, we obtain the glass transition temperature evolution all throughout the cure cycle. The results in figure 2.9 allows us to refine our first computation of the residual stress. In the first computation we took the highest temperature of the cure cycle, in this case $180°C$, but from the result in 2.9, we can take a lower initial temperature of $160°C$.

The equations and models allow us to compare more accurately different curing cycles. The residual stress of different curing cycle is compared in the following table. The residual stress from CTE mismatch were computed using equation 2.1, with the $\Delta\alpha$ chosen accordingly to T_g and $E = 170[GPa]$.

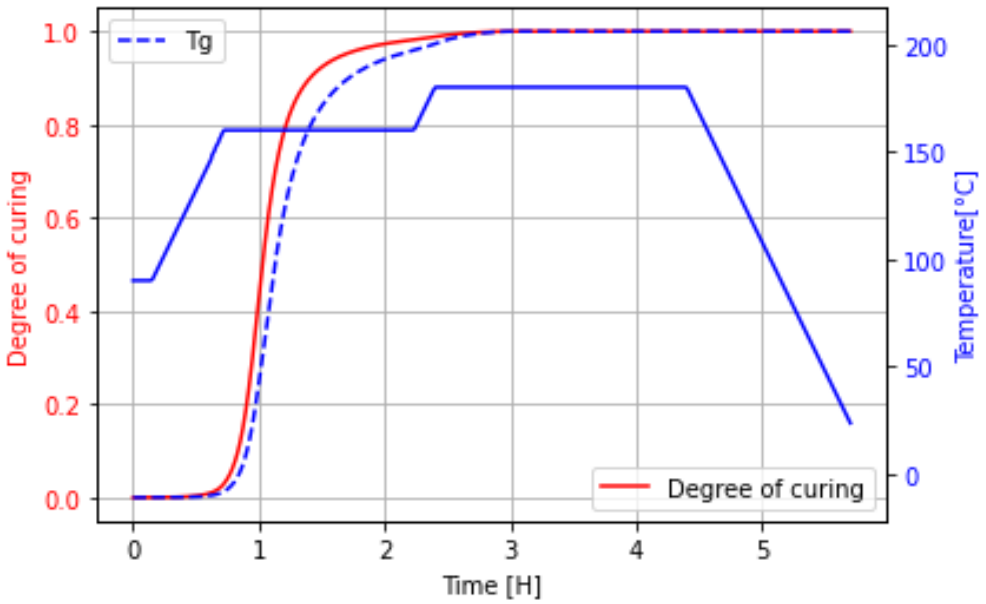

Figure 2.9: Glass transition in dashed blue with degree of curing and curing cycle in continuous blue.

	Curing cycle C160	Curing cycle C180	Curing cycle C180 Slow
Glass transition temperature $[°C]$	160	164	141
Residual resin stresses from CTE $[MPa]$	1520	1564	1314
Glass transition degree of cure $[\%]$	0.896	0.907	0.845
Residual strain from chemical shrinkage $[\mu\epsilon]$	1664	1488	2480
Total Curing time $[h]$	5.5	6.15	10.5

Table 2.5: Glass transition comparison between different curing cycles.

The C180 cure cycle is shown on figure 2.10 and the c180 Slow is shown on figure 2.11.

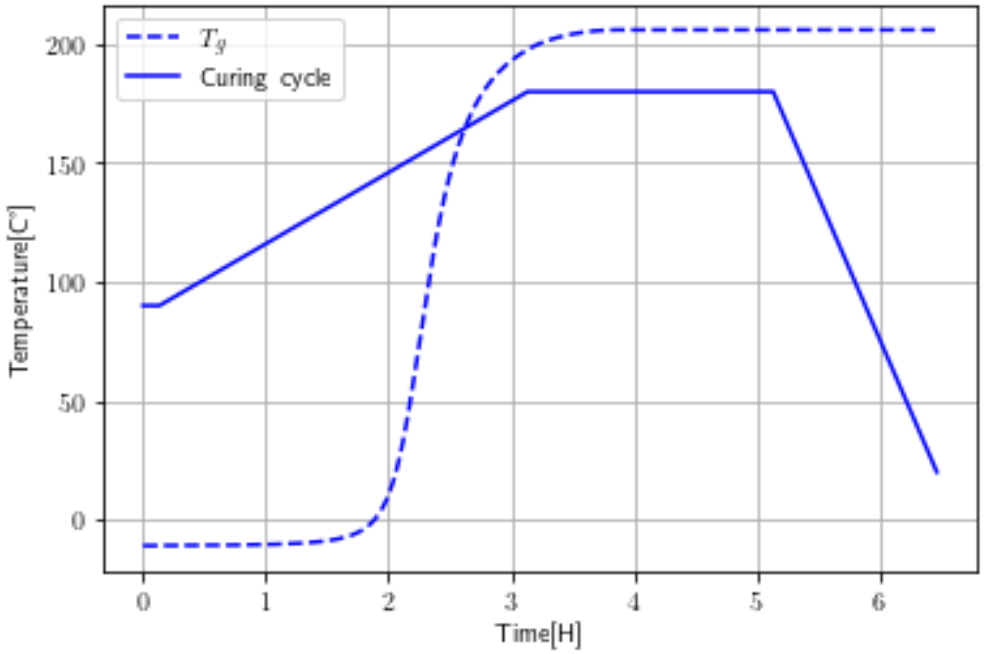

Figure 2.10: The C180 cycle and glass transition temperature evolution.

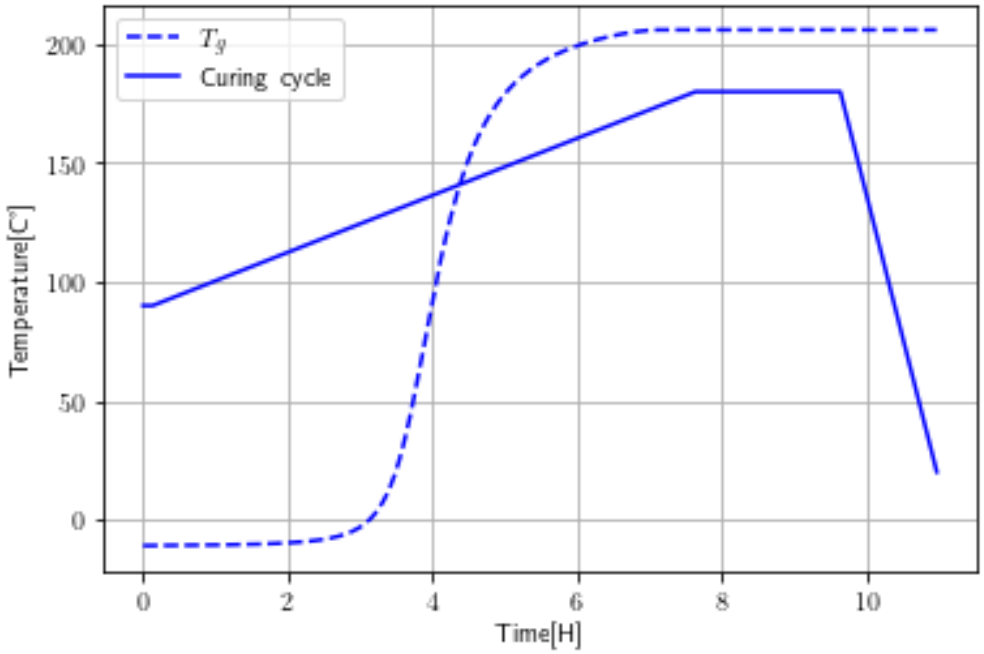

Figure 2.11: The C180 Slow cycle and glass transition temperature evolution.

2.3 Strain gauge temperature dependence

The integrated sensor will be subjected to many extreme conditions during the manufacturing process. Not only will the resin shrink chemically and due to CTE mismatch, but the curing occurs at high temperature, up to $180°C$. Pressure is applied on the mold, from atmospheric pressure up to a few tens of bar depending on the process[10]. All those conditions will modify the value read on the strain gauge during the manufacturing step and need to be compensated to get an accurate read on the strain.

For this work, the curing cycle used is shown on figure 2.7. As for the pressure due to a leak of the RTM mold, the process had to be swapped out to an autoclave at atmospheric pressure, otherwise it would have been set at 6 bars.

2.3.1 Silicon strain gauge temperature dependence

The temperature compensation is made by computing the change of mobility in the bulk silicon. A first approximation can be done via Mathiessen's rule by summing the inverse mobilities of different interactions sources. Those sources are interactions between carrier and impurities, phonon, or other carrier.

$$\mu = \left(\frac{1}{\mu_{Impurities}} + \frac{1}{\mu_{Lattice}} \right)^{-1} \tag{2.16}$$

For which their temperature dependencies are given as

$$\mu_{Impurities} = \frac{BT^{\frac{3}{2}}}{N} \tag{2.17}$$

$$\mu_{Lattice} = \frac{A}{T^{\frac{3}{2}}} \tag{2.18}$$

Where A and B are constants for a given material at a given impurity level. They can be estimated from experimental measurement, for this case the measurement from [64] will be used. The estimation of each constant requires to know the initial dopant concentration from the sensor.

This can be extracted from the properties given in the specification sheet from BCM sensor. The mobility of hole for P-doped silicon at room temperature for low and medium dopant concentration is around $480\frac{cm^2}{Vs}$. By then using the equation 2.19, the concentration of the BCM sensor can be estimated.

$$\frac{1}{\rho} = q(\mu_p P_p + \mu_n N_p) \approx q\mu_p P_p \tag{2.19}$$

The conductivity of the sensor can be computed from the resistance and geometry of the sensor by using 2.20.

$$\rho = R\frac{l}{tw} \tag{2.20}$$

Where $r = 1000$, $l = 0.26cm$, $t = 0.02cm$, $w = 0.004cm$. This gives a result of $\rho = 0.307\Omega.cm$. With equation 2.19 and the resistivity, the value extracted for the gauge doping

is $N_A = 4.23 * 10^{16} cm^{-3}$. This is an approximation as the value for the mobility may not be entirely right. On figure 2.12, the resistances for different values of doping of a block with the same dimensions as given above.

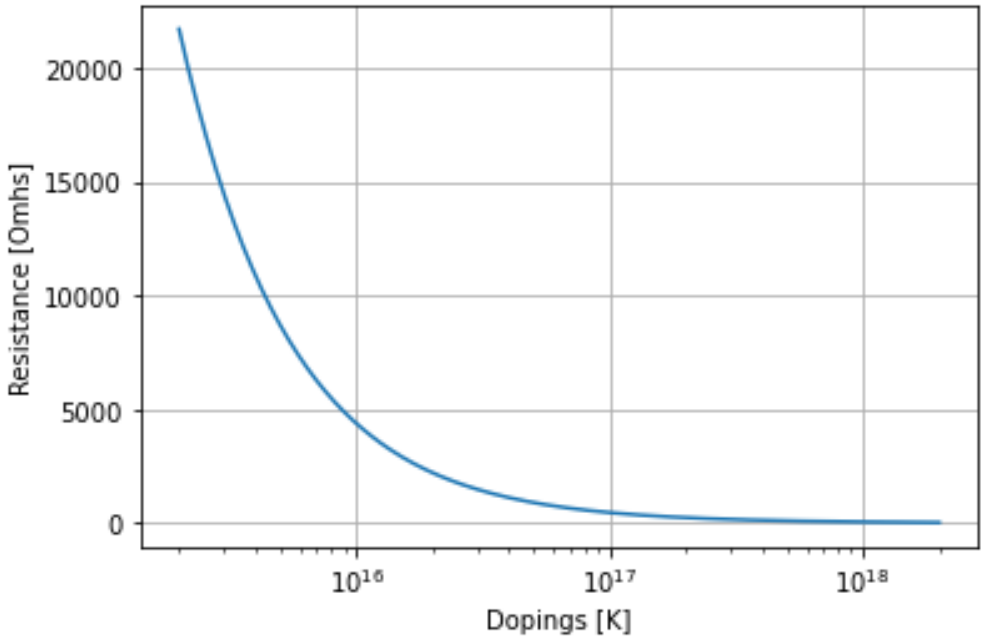

Figure 2.12: Resistance of a P doped block of silicon for different doping level.

With the extracted value of resistivity, $\rho = 0.55\Omega.cm$ extracted from [64], the constant A can be approximated.

At high temperature and low doping, equation 2.16 can be simplified into

$$\mu \approx \mu_{Lattice} \tag{2.21}$$

We obtain a value of $1.616 * 10^6$ and $5.64 * 10^16$ for A and B respectively.

For equation 2.16, the mobilities for the different interactions are simplified versions. To obtain a more accurate description, the model of Klaassen [65, 66] will be used for this work. The Mathiessen rule is still used but the mobility computation is more detailed. The total carrier mobility is given by

$$\mu^{-1} = \mu_{h,L}^{-1} + \mu_{h,D}^{-1} + \mu_{h,A}^{-1} + \mu_{h,e}^{-1} \tag{2.22}$$

Where $\mu_{h,L}$ is the highest hole mobility achievable when only the lattice scattering affects the mobility. The value of $\mu_{h,L}^{-1}$, is a parameter given in [65] and available in table 2.7.

$$\mu_{h,L} = \mu_{max} \tag{2.23}$$

$\mu_{h,D}$ is the mobility due to the minority impurity scattering. Unfortunately, the computation of the mobility requires the concentration of the minority impurities, which we do not

have. Not only that but this mobility only becomes consequent at low temperature or at high carrier density, neither situation is achieved in this work.

$\mu_{h,A}$ is the mobility due to the majority impurity scattering. It is given by equation 2.24, 2.25 and 2.26.

$$\mu_{h,A} = \mu_{h,N}\left(\frac{N_{ref,A}}{N_A}\right)^{\alpha_1} + \mu_{h,c} \tag{2.24}$$

$$\mu_{h,N} = \frac{\mu_{max}^2}{\mu_{max} - \mu_{min}} \tag{2.25}$$

$$\mu_{h,c} = \frac{\mu_{min}\mu_{max}}{\mu_{max} - \mu min} \tag{2.26}$$

Where μ_{max}, μmin, α_1 and $N_{ref,A}$ are given parameters from [65] and are available on table 2.7.

$\mu_{h,e}$ is the mobility due to electron-hole scattering. The equation describing the mobility for electron-hole scattering is the following:

$$\mu_{h,e}(n,c) = F(P_h)\mu_{h,A}(N_A = n, c) \tag{2.27}$$

The electron mobility can be computed from equation 2.24 by using the electron concentration. The concentration of electron in a non-degenerate P type silicon semiconductor can be obtained by using the neutrality of charge within the semiconductor.

$$p + N_D^+ = n + N_A^- \tag{2.28}$$

The function $F(P)$ is the mobility ratio between stationary secondary scatterer and moving secondary scatterer. This function is fitted to match the experimental result.

$$F(P) = \frac{r_1 P^{r_6} + r_2 + r_3\frac{m_1}{m_2}}{P^{r_6} + r_4 + r_5\frac{m_1}{m_2}} \tag{2.29}$$

Where m_1 and m_2 are the mass of the primary and secondary scatterer. the parameter p is given by equation 2.30

$$P = \frac{1.36 \times 10^{20}}{c}\frac{m}{m_0}\left(\frac{T}{300}\right)^2 \tag{2.30}$$

And the parameter r_i is given in table 2.6.

r_1	r_2	r_3	r_4	r_5	r_6
0.7643	2.2999	6.5502	2.367	-0.01552	0.6478

Table 2.6: Parameters fitting for mobility with electron-hole scattering

μ_{max}	μmin	α_1	$N_{ref,A}$	θ_h
470.5	44.9	0.719	$2.23 * 10^{17}$	2.247

Table 2.7: Parameters value for the mobility model

With this we have the mobility for silicon at room temperature, only the lattice scattering, and the majority impurity needs to be adapted to take into account the effect of temperature. The effect of electron-hole scattering is already considering temperature via the value of P from equation 2.30 Equation 2.23 becomes

$$\mu_{h,L} = \mu_{max} \left(\frac{300}{T} \right)^{\theta_i} \tag{2.31}$$

Where θ_i is chosen to match the experimental data, it is available in table 2.7. As for equation 2.25 and 2.26, they become

$$\mu_{h,N} = \frac{\mu_{max}^2}{\mu_{max} - \mu_{min}} \left(\frac{T}{300} \right)^{3\alpha_1 - 1.5} \tag{2.32}$$

$$\mu_{h,c} = \frac{\mu_{min}\mu_{max}}{\mu_{max} - \mu min} \left(\frac{T}{300} \right)^{0.5} \tag{2.33}$$

With α_1 being given in table 2.7.

The resulting change in resistance for a given temperature is shown on figure 2.13 where the change of resistance are nearly linear.

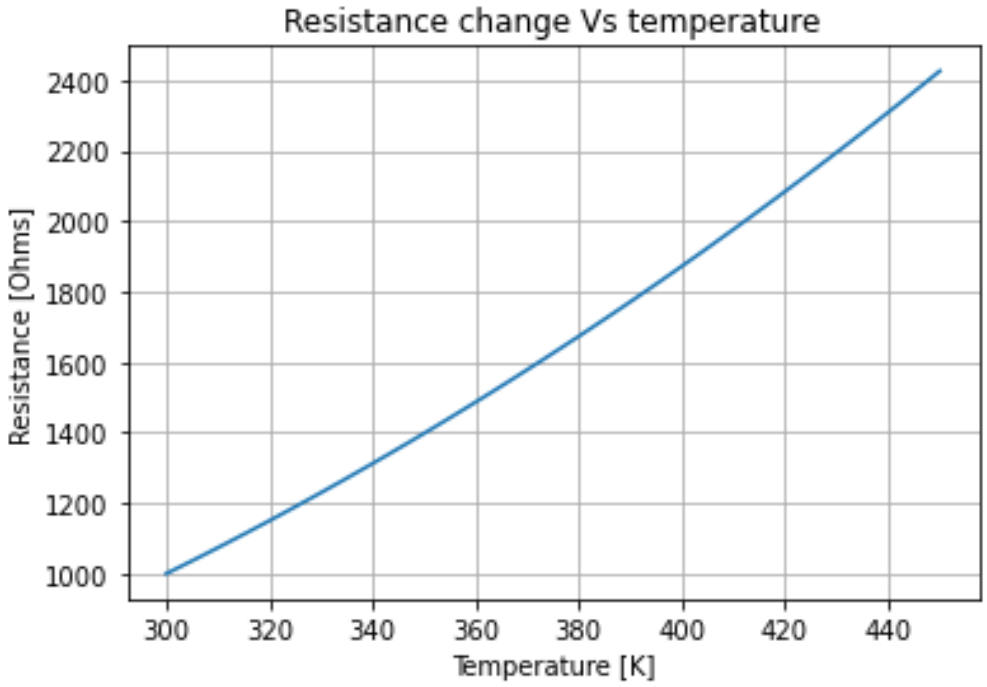

Figure 2.13: Resistance Vs temperature.

2.3.2 Metallic strain gauge temperature dependence

Metallic strain gauge reacts differently to temperature than silicon, in fact depending on the kind of alloy it is made off the dependence changes entirely. While the resistivity of metals

is often modelled as changing linearly to temperature such as shown on 2.34, the output of a piezoresistive strain sensor does not changes linearly to temperature.

$$\rho = \rho_0 + \alpha\rho_0(T - T_0) \tag{2.34}$$

The non-linearity may come from the encapsulated nature of the strain gauge or due to the way the comb pattern deforms when constraint and heated up. Regardless, the manufacture of the strain gauge often measures the dependency on temperature and provide data to compensate for it.

In the case of the Micro Measurments CEA-05-250UWA-350 Constantan alloy strain gauge, a polynomial of the fifth order is given to compensate the output of the strain gauge with. The polynomial has the form shown in 2.35.

$$\epsilon_{compensation} = a_0 + a_1T + a_1T^2 + a_3T^3 + a_1T^4 + a_5T^5 \tag{2.35}$$

For our strain gauge the final temperature compensation is shown on figure 2.14

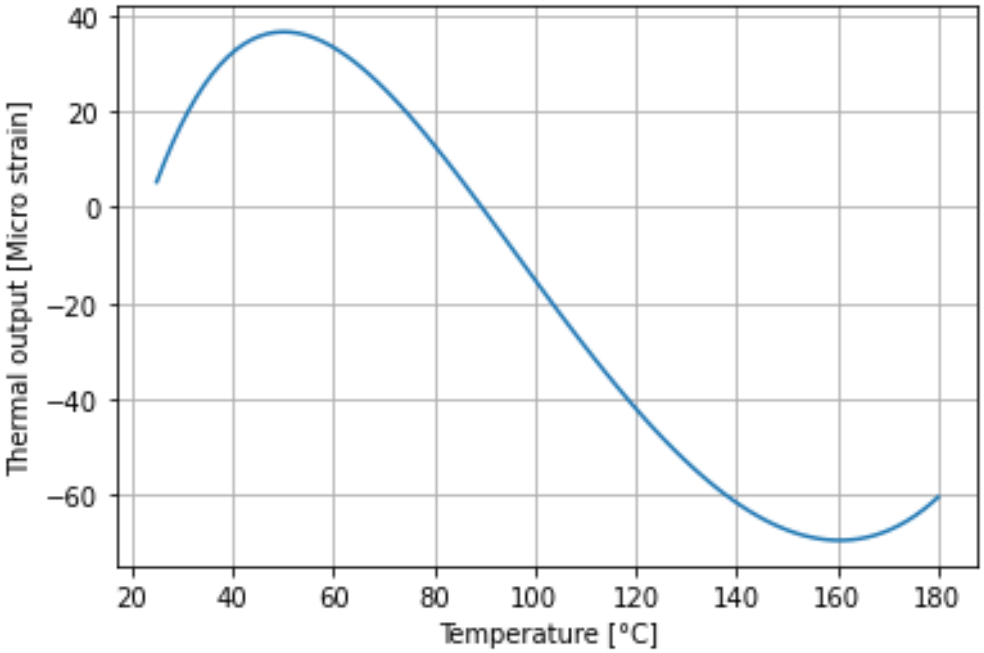

Figure 2.14: The thermal output of the metallic gauge.

As for the equivalent resistance change, it can be simply obtained by plugging the thermal output in micro-strain into equation 1.2 to obtain ΔR. The ΔR is shown on figure 2.15

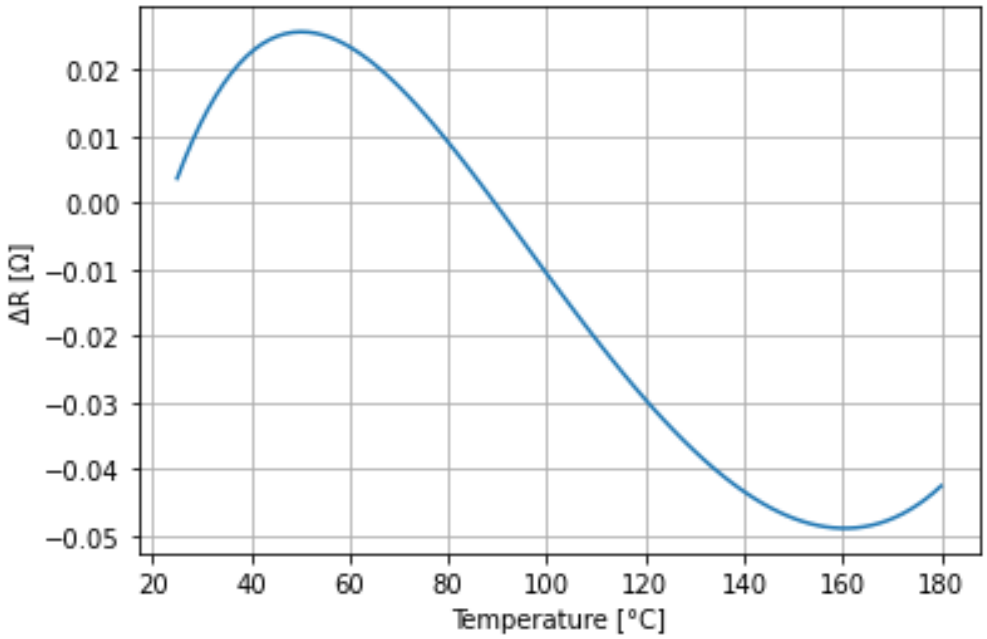

Figure 2.15: The resistance offset due to temperature.

2.4 Conclusion of the analytical model

In this chapter different model were shown and analysed to learn the impact of different parameters on the residual stress. It was found that sensor who impact the final strain of the stacks generates less stress, albeit with the probable cost of deforming the final geometry of the stack. While other parameter than the CTE mismatch affects the residual stress, the most sensitive parameter remains the CTE mismatch.

The second part of this chapter details how the variation of the materials properties was handled for the curing. Most of them can be simplified into averages and give an accurate approximation. As for the glass transition temperature, it was shown how the process can affect the moment and temperature of the transition and thus the resulting residual stress.

The third part of the chapter described the response of strain gauge to temperature, this has a twofold use.
The first one is the compensation required during the curing process; it will allow to accurately measure the strain after the glass transition has occurred. The second one, is the temperature measurement before the gel point is reached.

With the analytical result studied, they can now be compared to the simulations and the experimental data to verify their validity.

Chapter 3

Numerical Analysis

In this chapter all the numerical simulations will be presented. The first parts will compare two software for finite elements with a small thermal stress simulation.

Then all the simulations for the residual thermal stress of an embedded sensor in resin will be shown. Those simulations will sweep different parameters to verify the analytical model analysed in the previous chapter. The trends and absolute value will briefly be compared

Afterwards, the transient thermal simulation will be shown to verify the homogeneous temperature hypothesis.

Finally, a small description of the original simulation objective is given and the why it was not done in the end.

3.1 Simulations

During the previous chapter, it was shown that the geometry of the real problem is more complex than any of the geometry of the analytical models analysed. This limits the analytical model to give an approximation of the stress and it's dependencies on different parameters. Another problem is the orthotropic properties of CFC, most analytical model make the assumption that the material are isotropic, which is only the case for the resin and sensor alone. To obtain more accurate result, the use of finite element is required. Multiple simulations for different situations have been made:

- Naked gauge within a composite during cooling only
  - Parametric sweep: Temperature, Materials CTE, sensor geometry, position.
- A gauge with a baking within a composite during cooling only
  - Parametric sweep: Temperature, Materials CTE both backing and strain gauge.
- Transient simulation for curing
  - Curing evolution
  - Temperature evolution

– Full mechanical evolution(Was not done)

Each simulation comes with its own set of hypothesis and simplification and reflects different situations. The reason naked gauge and gauge with baking were compared is due to the availability of the different gauge at the time of experiment. For the experiments, gauge with baking were used as they were the only one available at first. And while naked gauge became available later on, the difficulties of soldering cable and placing them without breaking them made them unusable. A simulation was still made with their geometry, as it is possible to embed them, but it requires adequate manipulation. As for the cure evolution it was already covered in section 2.2.1.

3.2 Simulation software

Nowadays, the number of finite element analyser available makes us ask a new question, which one do we use. At UCL, quite a few are available, but two were chosen and compared.

- COMSOL Multiphysics®
- Ansys Student

Most of the simulations in this work have been made in COMSOL® , with the exception of the temperature evolution simulation which was done in Ansys.

A small case study has been made to compare each software and make sure the result of both is coherent with each other.

3.2.1 Modules

To create a working simulation each software requires modules. The modules vary depending on the type of simulation. Table 3.1 shows the different modules required in each software for the simulations listed at the beginning of section 3.1. COMSOL® has a different approach than Ansys in terms of modules. In COMSOL®, the modules are separated in physics and study while in Ansys, the modules represent the physics and the type of study within the same module.

3.2.2 Case study

A small and simple simulation was done to compare the results of both software and confirm that the final choice is arbitrary. The simulation consists of three blocks, two made of steel and one made of silicon. The cubes of steel have a $20mm$ side, while the block of silicon is $20mm$ wide and long but has a thickness of $5mm$. The block of silicon is sandwiched between the two block of steel and then the whole tower of blocks is heated up.

The situation is similar to the simulation done for the sensor embedded in the resin. This is to compare the module that would be used for this work. Another point is that the geometry now matches perfectly the multi-layer model analysed in section 2.1.3, allowing us to compare the results of both software to an analytical model.

	COMSOL®	Ansys
Thermal expansion Residual stress	Solid Mechnaics Heat transfer in solids Multiphysics: Thermal expansion Study: Stationary	Steady state Thermal Static structural
Thermal gradient analysis during cure	Heat transfer in solids Study: Time dependent	Transient Thermal
Full cure analysis	Solid Mechnaics Heat transfer in solids Multiphysics: Thermal expansion Custom script(Curing) Study: Time dependent	Transient Thermal Transient Structural ACCS(Composite cure simulation)

Table 3.1: Modules and submodules necessary for each simulation

In table 3.2, all the material properties used for both simulations are set. Originally, custom materials value were to be chosen but difficulties were encountered in making the solutions converge, thus pre-available materials in Ansys were taken.

	Density $\frac{Kg}{m^3}$	Thermal Conductivity $\frac{W}{m.K}$	CTE $\frac{1}{^\circ C}$	Heat capacity $\frac{j}{Kg.K}$	Young's Modulus Pa	Poisson ratio
Steel	7850	60.5	$12 * 10^{-6}$	434	$2 * 10^{11}$	0.3
Silicon	2329	154.3	$2.578 * 10^{-6}$	695.1	$162.7 * 10^{9}$	0.27

Table 3.2: Material properties used for the software case study

Before even creating the mesh, attention is required in some of the default value in both software. The first step to both software is to fix the geometry, otherwise the solution will simply not converge. In Ansys, it is done via remote displacement sub-module in the static structural module. In COMSOL®, it is done via the rigid motion suppression sub-module in the solid mechanics module.

The second step is to define the final temperature and the initial temperature, care should be taken as in Ansys the temperature is by default taken in Celsius and in COMSOL® in Kelvin. Temperature and initial temperature are both sub-modules of the heat transfer in COMSOL® and steady-state thermal in Ansys. It is important for those who wants to change the initial temperature in COMSOL®, to also change it in the thermal expansion sub-module of the multiphysics module.

After all parameters have been entered, our geometry needs a mesh. Both softwares have their own built in mesh builder, but both allows to import meshes too. In this case the mesh of each software were created using their built in tool. For Ansys, by default, the meshes pattern used were squares as shown on figure 3.1. Unfortunately, COMSOL® doesn't generate square with it's built in tool. Instead, a patch conforming method sub-module was

used in Ansys to generate a tetrahedral mesh.

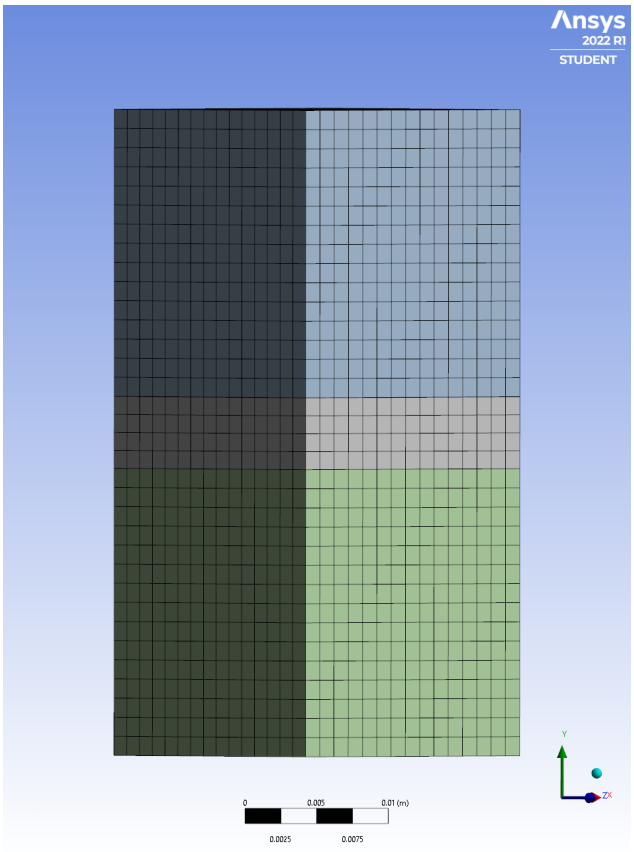

Figure 3.1: The quad mesh of Ansys default.

To compare similar mesh, different parameters for building said meshes had to be fixed in both software, the resulting parameters are available in table 3.3.

With the resulting meshes in place and both software configured to simulate the same event, both computed their results.

The only noticeable difference between the two software is the meshing, while the number of elements is nearly the same, the way some of the mesh element follows some contour is different. This result in the only noticeable difference where the stress propagation at the corner is slightly greater in Ansys than in COMSOL®. Apart from this minor difference, the overall shape and magnitude of the stress distribution is extremely similar in both software. Now that both software have been shown to be equivalent in terms of final solution, the choice of either becomes arbitrary.

The results of both software can be compared to the analytical model of section 2.1.3 to obtain a first estimation of the accuracy of said analytical model. The comparison is between the average Von Mises stress in the silicon layer in both COMSOL® and Ansys and the stress given by equation 2.8.

Ansys		COMSOL®	
Element size	1.35mm	Minimum element size	0.5mm
Max size	2mm	Maximum element size	2mm
Growth rate	1.5	Maximum element Growth rate	1.5
Mesh number of elements	37960	Mesh number of elements	36903

Table 3.3: Software parameters for the meshing and resulting number of elements

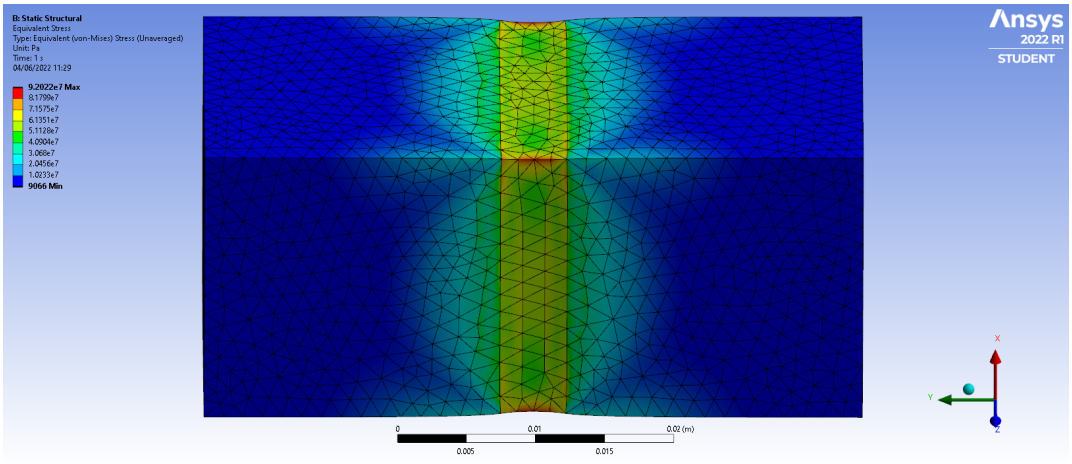

Figure 3.2: Resulting Von mises stress for thermal CTE mismatch in Ansys.

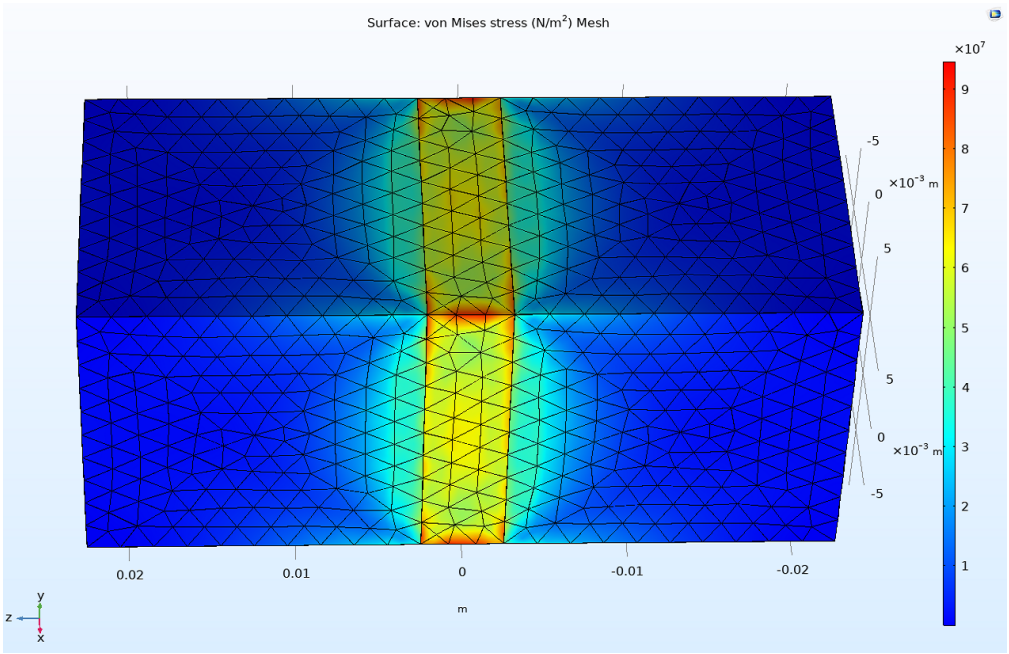

Figure 3.3: Resulting Von mises stress for thermal CTE mismatch in COMSOL®.

Analytical Result $\frac{N}{m^2}$	COMSOL® $\frac{N}{m^2}$	Ansys $\frac{N}{m^2}$
$5.12 * 10^7$	$3.77 * 10^7$	$4.1 * 10^7$

Table 3.4: Average predicted stress in the silicon block.

3.3 Baked gauge thermal mismatch

The first simulation consisted of simulating the cooling down of the composite with the baked gauge within. The baked gauge consisted of a piece of rectangular silicon on top of a modified polyimide backing. The properties of silicon are well known and defined, but less is known about polyimide, it is also a modified version of it. The materials properties are represented on table 3.5. As for the exact dimension of the sensor, baking, and resin block, they are in table 3.6

	Density $\frac{Kg}{m^3}$	Thermal Conductivity $\frac{W}{m.K}$	CTE $\frac{1}{^\circ C}$	Heat capacity $\frac{j}{Kg.K}$	Young's Modulus Pa	Poisson ratio
Epoxy	1140	0.15	$68.4 * 10^{-6}$	1100	$2.51 * 10^9$	0.38
Silicon	2390	130	$2.1 * 10^{-6}$	700	$170 * 10^9$	0.28
Polyimide	1300	0.15	$9 * 10^{-6}$	1100	$3.1 * 10^9$	0.4

Table 3.5: Material properties used for the residual stress simulations

	Width mm	Length mm	Thickness mm
Sensor	0.2	2.6	0.04
Baking	3	5	0.03
Resin	8.75	25	2.5

Table 3.6: Dimension of the resin, baking and sensor used for the simulation

At first to hasten the global simulation of the embedded strain gauge, the global property of the backing and gauge were examined. Unfortunately, due to the asymmetric placement of the gauge on the backing, only a fully anisotropic model could be used. Not only was an anisotropic model less convenient but the extraction of the elasticity modulus matrix was complicated. The definition of the elasticity matrix components is the following:

$$\begin{pmatrix} \sigma 11 \\ \sigma 22 \\ \sigma 33 \\ \sigma 12 \\ \sigma 13 \\ \sigma 23 \end{pmatrix} = \begin{pmatrix} C_{1111} & C_{1122} & C_{1133} & C_{1211} & C_{1311} & C_{2311} \\ C_{1122} & C_{2222} & C_{2233} & C_{1222} & C_{1322} & C_{2322} \\ C_{1133} & C_{2233} & C_{3333} & C_{1233} & C_{1333} & C_{2333} \\ C_{1211} & C_{1222} & C_{1233} & C_{1212} & C_{1312} & C_{2312} \\ C_{1311} & C_{1322} & C_{1333} & C_{1312} & C_{1313} & C_{2313} \\ C_{2311} & C_{2322} & C_{2333} & C_{2312} & C_{2313} & C_{2323} \end{pmatrix} \begin{pmatrix} \epsilon_{11} \\ \epsilon_{22} \\ \epsilon_{33} \\ 2\epsilon_{12} \\ 2\epsilon_{13} \\ 2\epsilon_{23} \end{pmatrix} \tag{3.1}$$

From equation 3.1, we can compute the matrix component of a material by measuring the strain due to an applied stress. This works well if the deformation in a direction is uniform, but as shown with figure 3.4, the deformation in the horizontal axis is dependent on where we take it on the vertical axis. An average could be used for two directions but the deformation in the direction going through the gauge and the backing made the simplification of the gauge impossible. The whole strain gauge being a non-trivial geometry rendered the entire point moot.

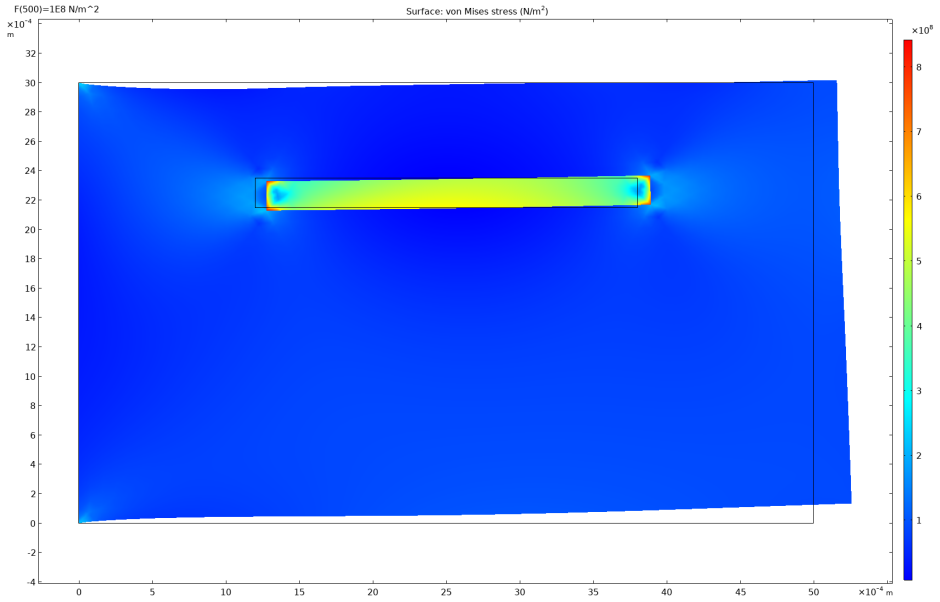

Figure 3.4: Silicon gauge deformation to a uniform horizontal load.

A second simplification has been made but this time to the composite. In [7] it was shown that different way of embedding the strain gauge result in different interaction between the gauge, the reinforcement and the matrix. In this work we only consider the resin for multiple reasons, one of them is the sheer complexity involving the whole composite. Another reason is the resin only is the worst-case scenario. Due to the complexity of the system, the worst case will represent whether embedding the strain gauge is actually feasible. Depending on the way the gauge is embedded, where it is placed and what size is the gauge, the final residual stress may be quite different. For example, not all gauges have the same size and as shown in figure 1.2, not all weaves are the same. If we take a unidirectional fiber with a small silicon gauge, the stress applied due to the fiber on the gauge will be very different if we take a five-harness satin weave and place a metallic gauge at the junction of 4 tows. A second reason for this simplification is creating a geometry for a particular weave is extremely hard, especially when you start considering the density of the carbon fiber composite and the manufacturing process. The result of the percentage of matrix vs reinforcement is generally dependent on the manufacturing process. It also changes from pieces to pieces within the same manufacturing line.

All those simplification result in the geometry shown on figure 3.5, where the strain gauge and backing are surrounded by a block of resin. There are three physics nodes used in the

simulation. The Mechanical physics node is used to estimate the stress and strain that will be generated. The thermal expansion node is used to simulate the different thermal shrinkage from the resin, backing and strain gauge. The heat transfer node is used to generate the difference of temperature between the glass transition temperature and the ambient temperature.

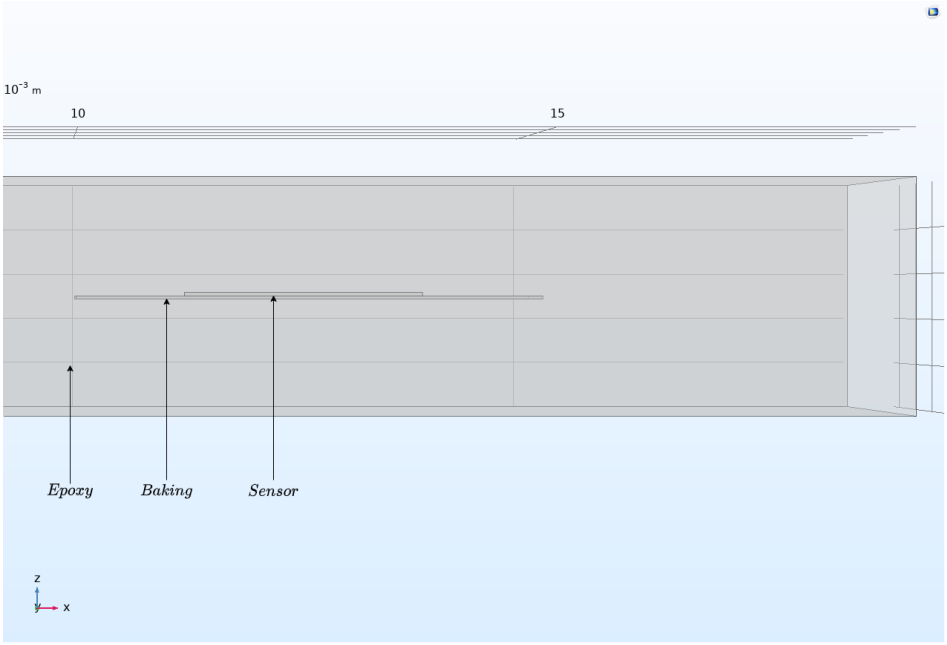

Figure 3.5: The baked gauge geometry.

3.3.1 Positioning impact

The first parameter to be analysed is the depth at which the strain gauge is embedded. In the model of Chun-Hway Hsueh[8], changing the depth correspond to shifting the thickness of layers above to layers below or vice versa relative to the studied layer. And from equation 2.8, we can see that regardless of how the different layers thickness are shifted, as long as the total thickness remains the same, the stress shall remain the same too. This is the case too even when the layer representing the strain gauge is the topmost layer. A quick parameter sweep was done in the simulation where the strain gauge is slowly rising from the center of the resin to one of it's boundary until the backing lays on top of the resin. The results can be seen on figure 3.6, where the stress start to decrease, albeit slowly, even before the strain gauge is partially out of the resin.

The resulting decrease in the average stress can be attributed to how the baking, compresses the strain gauge. The baking is made of modified polyimide which has a CTE closer to silicon than the RTM6. This reduced CTE mismatch and the fact that the backing is not compressed by the resin from all sides any more results in a reduced stress on the strain gauge. This tells us that strain gauge working for surface measurement of CFC might not

be suited for embedded design.

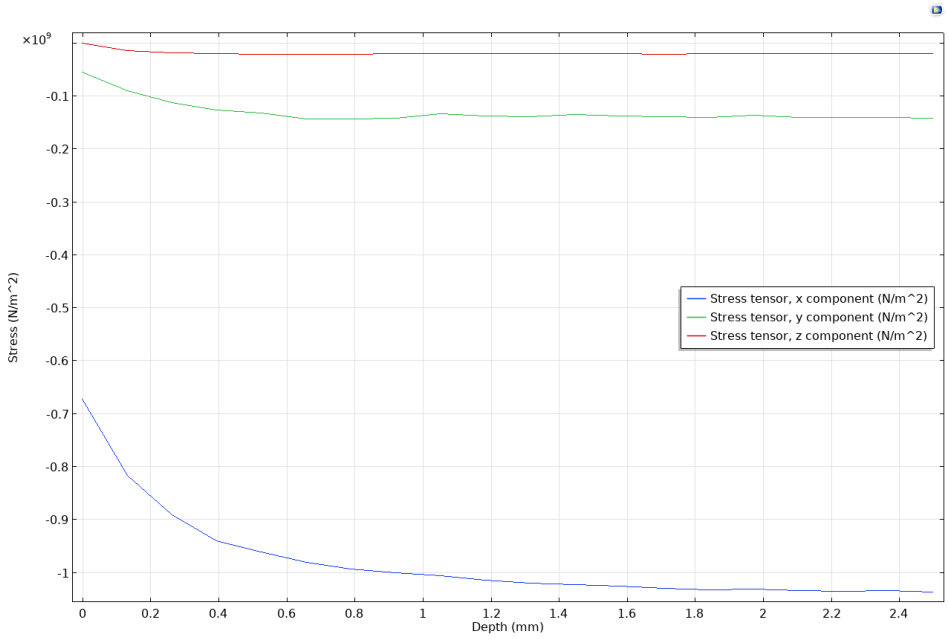

Figure 3.6: Strain gauge average stresses Vs embedding depth.

3.3.2 Corner singularities

The strain gauge used in the previous sweep was a simple bar with fillet to round the corner and avoid singularities. There exist many other geometries, many who are used with metallic gauge such as the comb pattern. The first geometry change was the introduction of fillet to the strain gauge, the goal of those fillet was to verify the presence of singularities in the simulation. The fillet were introduced with a radius of half the gauge thickness to obtain a perfectly smooth side. As shown on figure 3.7, the difference between the two geometries is small enough to discard the singularities. The biggest difference is the maximum x component of the stress tensor in the strain gauge which can simply be explained by the abrupt corner of the squared geometry. Another geometry assessed is the comb geometry.

3.3.3 Thermal mismatch sensitivity

In all analytical models, the stress variation always varies linearly to the temperature difference. While this might be true for small temperature difference, it does not consider the mechanical nonlinearity. A sweep is performed on the temperature difference to observe how the linear hypothesis holds within the range of temperature of real curing cycle.

Figure 3.8 shows that linearity of the stress due to temperature holds over the range of cure temperature even with the geometric non linearity. Even at low temperature difference,

the stress is still substantial, this is the result of high CTE mismatch and high Young's modulus.

3.3.4 Resin thickness sensitivity

In the previous chapter, the models showed a very high sensitivity to the thickness of the resin layers. The cause was highlighted as the increased strain of the sensor layer due to the other layer higher relative thickness. A sweep was performed from a $100\mu m$ thick resin, which is thinner than a single carbon fiber ply, up to 10mm which is the thickness of a thick composite stack.

The results shown on figure 3.9 corroborates the analytical models, as for a thin resin block, the stress are smaller than for a thick block. The stress quickly plateau after the total layer thickness of the resin becomes 25 times thicker than the sensor layer. This is expected, as after a certain threshold is reached, the resin has applied its full deformation upon the sensor and cannot apply further deformation without external forces.

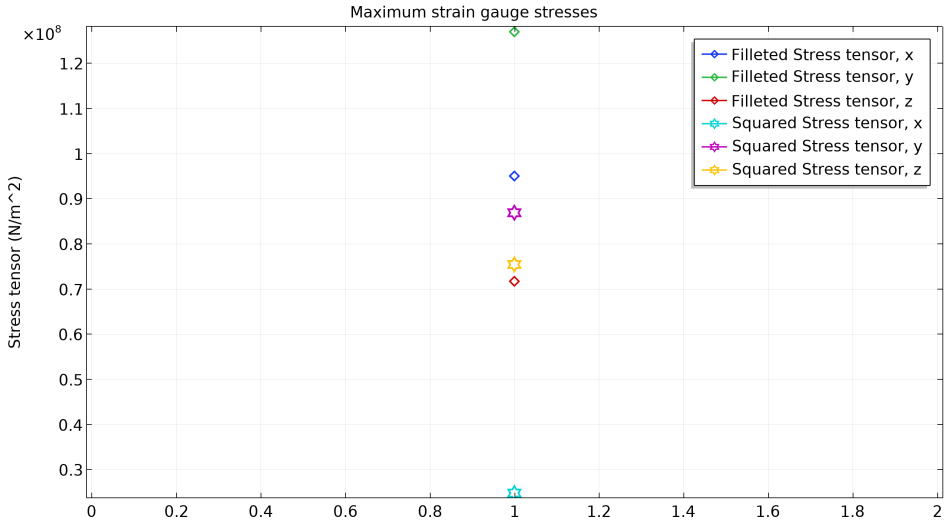

Figure 3.7: Max stresses, Fillet Vs Squared geometry.

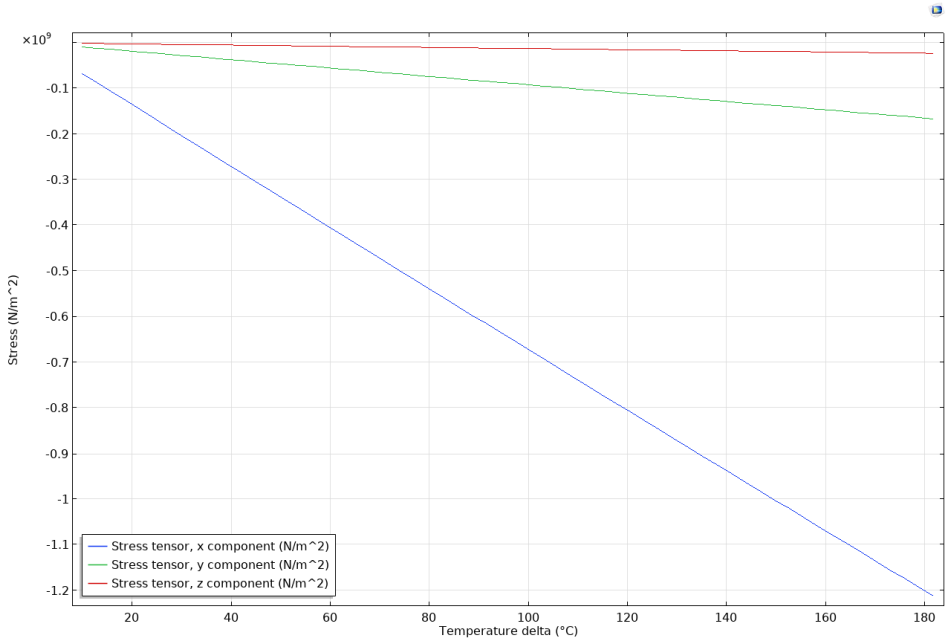

Figure 3.8: Average stress Vs varying ΔT.

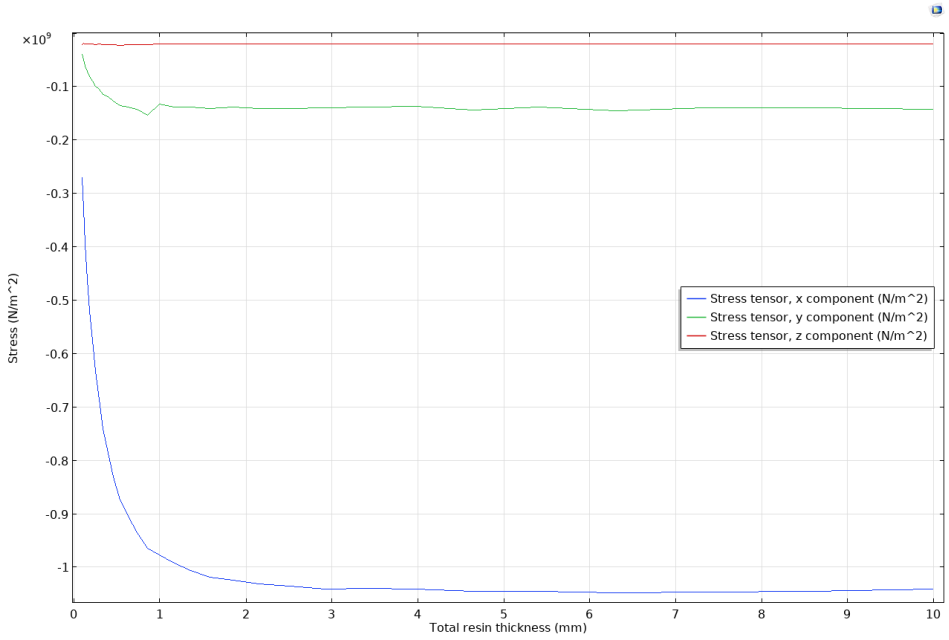

Figure 3.9: Average stress Vs varying resin thickness.

3.4 Naked gauge thermal mismatch

The second sets of simulations were very similar to the first one, except the geometry was altered. The baking of the strain gauge was removed, leaving only the gauge. This resulted

in a symmetrical problem which is much simpler. While strain gauge with this geometry were available, there fragility when manipulating them, made them unusable for our experiment.

3.4.1 Positioning impact

The same sweep on the position of the naked gauge was performed to determine how the backing affected the stress induced on the gauge. Since the problem is no longer asymmetric, the stresses will be redistributed but the overall magnitude of the stresses should remain similar.

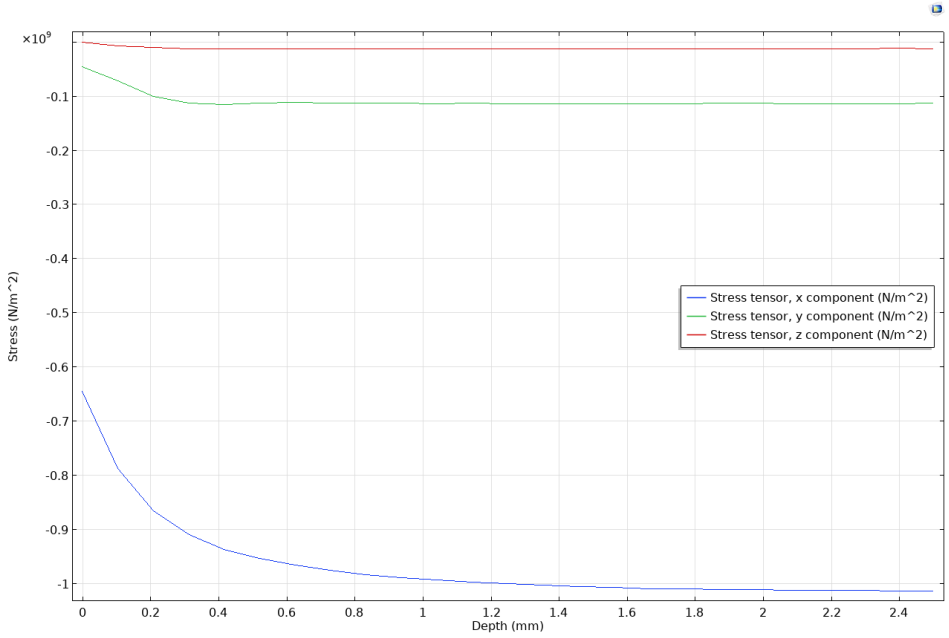

Figure 3.10: Strain gauge average stresses Vs embedding depth.

The results on figure 3.10 and 3.6 show that the backing has very little influence on the overall stress in the strain gauge. The decrease in stress even before the strain gauge is partially out of the resin is also present in the case of the naked gauge. The phenomenon may come from the very thin layer of resin above which is unable to put much stresses upon the much stiffer silicon strain gauge.

This also tells us, that the deeper the strain gauge is, the more stress will be placed upon it. The stress will plateau to a maximum but the most interesting place to have a strain gauge is also the harshest on the gauge.

3.4.2 Sensor geometry

In the last subsection, it was observed that fillet made only a small difference, so this time the comb geometry mentioned above is analysed. The geometry of the sensor is shown on

figure 3.11, it is not exactly the same as the commercial sensor as it does not have the same amount of beam, but the general geometry remains similar.

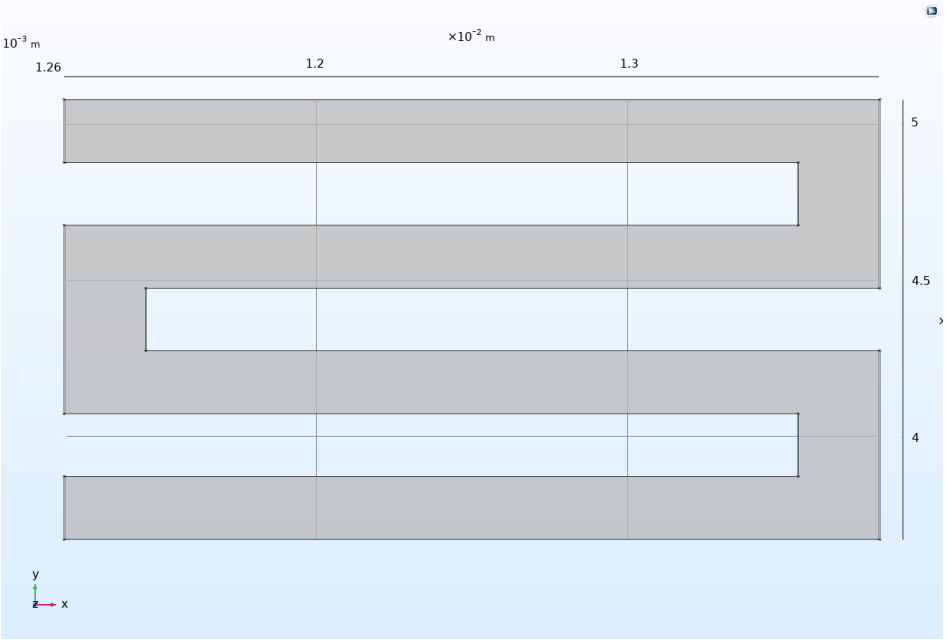

Figure 3.11: Comb sensor geometry.

	Square gauge	Comb gauge
Average stress tensor x direction $\frac{N}{m^2}$	$-2.736 * 10^8$	$-2.262 * 10^8$
Max stress tensor x direction $\frac{N}{m^2}$	$-3.489 * 10^8$	$-8.645 * 10^8$
Average stress tensor y direction $\frac{N}{m^2}$	$-3.088 * 10^7$	$-4.948 * 10^7$
Max stress tensor y direction $\frac{N}{m^2}$	$-1.085 * 10^8$	$-6.430 * 10^8$
Average stress tensor z direction $\frac{N}{m^2}$	$-2.837 * 10^6$	$-2.487 * 10^6$
Max stress tensor z direction $\frac{N}{m^2}$	$-1.088 * 10^8$	$-2.224 * 10^8$

Table 3.7: Average stress comparison between the comb geometry and square geometry.

The differences shown in table 3.7 are small. Despite the geometry changing quite dramatically, the overall order of magnitude stayed similar for the average and maximum stress. In the case of the comb, while the average stress was smaller than the square geometry in the x and z direction, the maximum value obtained in those direction was higher in absolute terms. This may result in lower measured residual strain but a higher likelihood of failure during its lifetime. Regardless since the magnitude of the stress remains the same, it is unlikely for the geometry to impact whether the embedding of a sensor is feasible or not. The only reasons for geometry would be the size constraint imposed in chapter 1. Note that to keep the comparison relevant we kept the material of the strain gauge in the simulation to silicon. This shape is used mostly for metallic commercial gauge.

3.4.3 Thermal mismatch sensitivity

The analysis is the same as in section 3.3.3, except without the baking of the gauge. Since the baking had a slightly different CTE and Young's modulus than the resin, the results are expected to be slightly different.

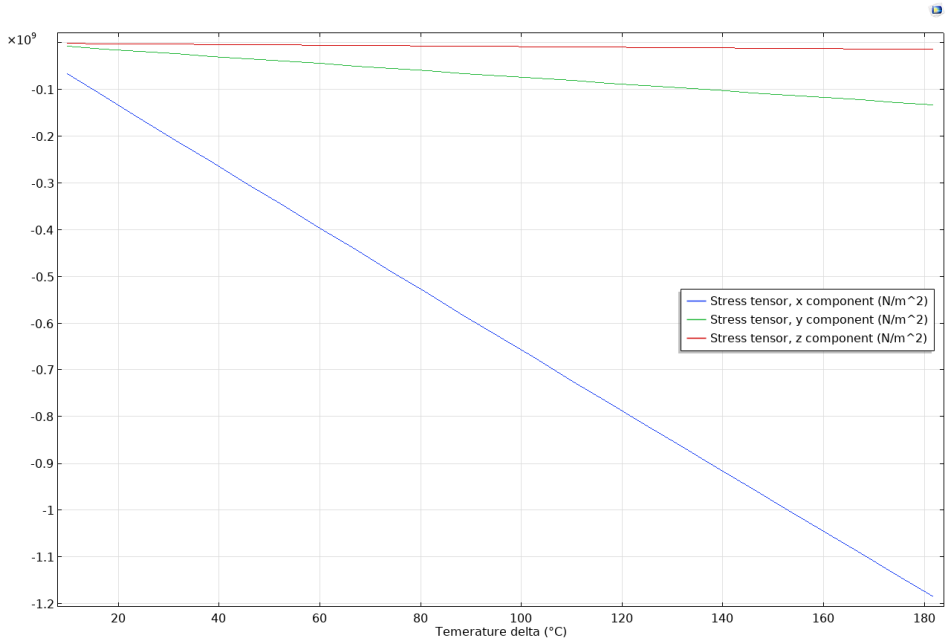

Figure 3.12: Average stress Vs different temperature delta.

The result of figure 3.12 follow the same trends as figure 3.8 which is expected. Something surprising, is the very slight decrease of the stress in the x direction of the naked gauge compared to the baked one. Indeed, since the CTE mismatch between the baking and the sensor was smaller, the absence of baking would lead to think the stress would increases. This slight decrease might be the result of the lower stiffness of the epoxy compared to the polyimide. While to reduce the residual stress of the sensor, we could surround it with a softer material, the strain transmission between the composite and the sensor may be compromised.

3.4.4 Resin thickness sensitivity

The exact same pattern that happened for the thermal mismatch happened here. The overall stress is diminished, and the trends remains the same as with the baked gauge on it. Interestingly the analytical model predicted stronger stress for thick layers of resin. From figure 2.6, the stresses for a total of 6mm of resin and a CTE mismatch of $66 * 10^{-6}$ are around $1.250GPa$ compared to $1GPa$ of figure 3.13

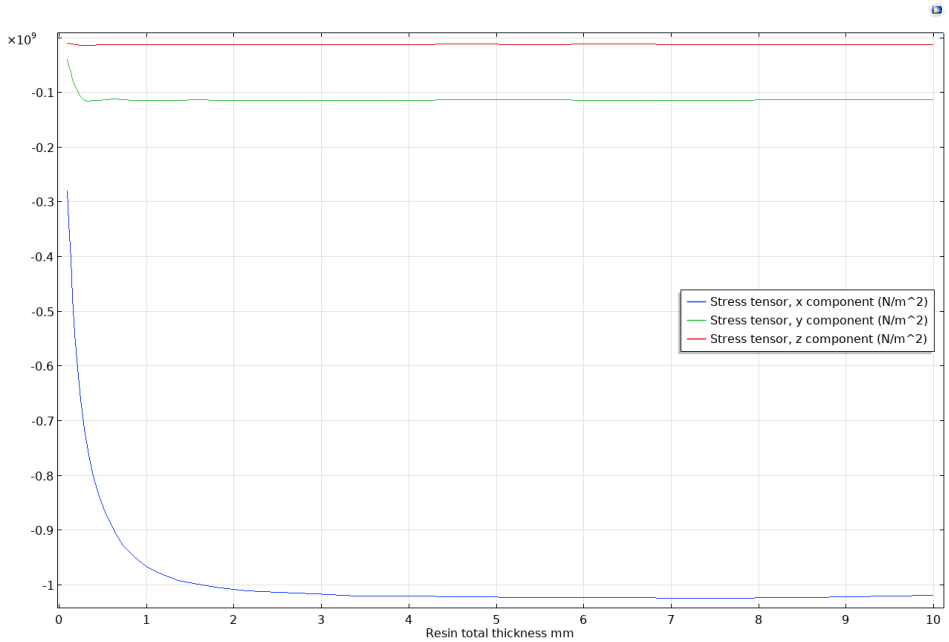

Figure 3.13: Average stress Vs total thickness of the resin.

3.5 Temperature evolution

One of the hypotheses in all simulation is the homogeneity of the cure and temperature. While the homogeneity of the cure is difficult to verify, the homogeneity of temperature is not. Two points need to be addressed to verify temperature homogeneity. The first is the heat emitted from the cure reaction, as the resin starts to cross link, it generates heat which needs to be dissipated. The second point is the thermal inertia of the mold and the resin. As the oven heats up the resin and mold will follow but since their heat capacity isn't zero and their thermal conductivity isn't infinite, the temperature of some part of the resin and mold may lag behind the temperature of the oven.

3.5.1 Generated Heat

The first aspect to model is the heat generation due to the cross-linking. This was done with the cross linking enthalpy, $H = 432\frac{J}{g}$, which was given in [67] for the RTM6. The heat emitted from a partial curing, $\dot{x}$, of a block of resin with mass m, is given as:

$$E = mH\dot{x} \tag{3.2}$$

To verify whether the heat generated is being dissipated fast enough, the samples were modelled as a two parallel heat circuit. One representing the dissipation of the heat through the resin-air circuit and the other representing the resin-mold-oven plate circuit.

The thermal resistance of the resin and mold can be computed if we make the hypothesis that the heat flows only in a single direction. Due to the low heat conductivity of the resin and its thinness, it is valid in the center piece of the sample. Close to the side, this

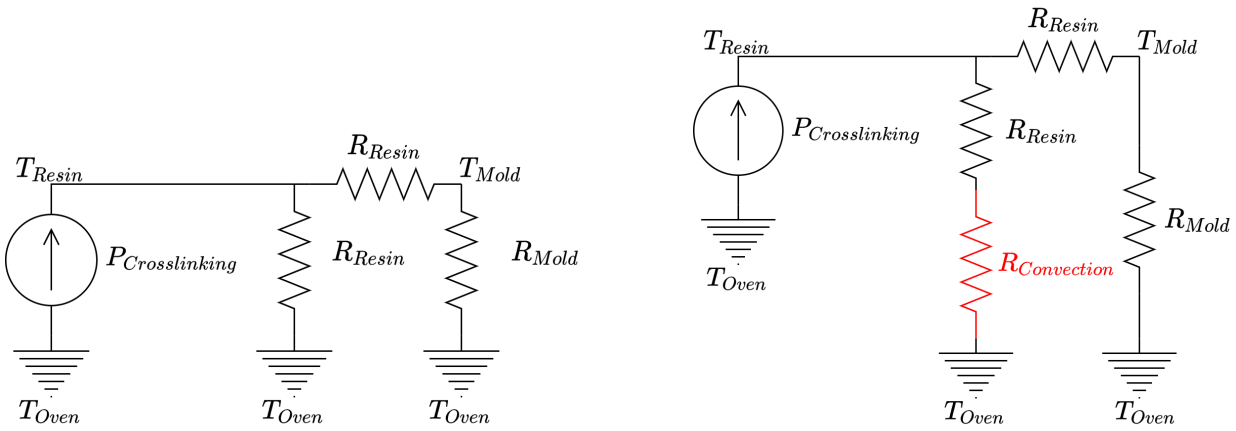

(a) Temperature boundary conditions

(b) Convection boundary conditions

Figure 3.14: Simplified heat circuit models.

approximation breaks down as the heat can be dissipated via the side of the mold. Despite the approximations not being valid anymore, since the side would dissipate more heat than the center, if the center dissipates heat fast enough, so will the sides.

The resistance of the resin and mold can be computed with the Fourier law.

$$R = \frac{t}{Ak} \tag{3.3}$$

where t is the thickness of the material, A the surface area which the heat goes through and k the thermal conductivity of the material. k has been extracted from Granta edupack of Ansys.

Before calculating the heat generated by the reaction, the boundary between the resin and the air needs to be characterised. As of now we considered both the boundaries between the mold and oven and between the resin and air to be set at the temperature of the oven. While this is true for the bottom of the mold, it is not for the top of it. The excess heat is dissipated via convection with the air. Convection in the equivalent circuit is also represented as a resistor, except the resistor value is calculated differently.

Starting with Fourier's law in 3.3, the thermal conductivity can be replaced by the heat flux with the following equation:

$$q = k\frac{\Delta T}{t} \tag{3.4}$$

To give.

$$R = \frac{t}{Aq\frac{t}{\Delta T}} \tag{3.5}$$

Which can be simplified into.

$$R = \frac{\Delta T}{Aq} \tag{3.6}$$

The heat flux from convection can be computed from the surface area and the convection coefficient. For the numerical value of the convection coefficient, the value was extracted from [68], as a typical value for free air. Convection heat flux is given by.

$$q = h\Delta T \tag{3.7}$$

Replacing the heat flux in 3.6 by 3.7 will yield the following equation.

$$R = \frac{\Delta T}{hA\Delta T} = \frac{1}{hA} \tag{3.8}$$

All the numerical for the sample are shown on table 3.8.

	Resin	Mold	Resin air interface
thickness(t)	$4mm$	$5mm$	NaN
Area(A)	$64cm^2$	$64cm^2$	$64cm^2$
Thermal conductivity(k)	$0.18\frac{W}{m\circ C}$	$16.2\frac{W}{m\circ C}$	NaN
Convection coefficient(h)	NaN	NaN	$5\frac{W}{m^2\circ C}$
Thermal resistance	$3.47\frac{\circ C}{W}$	$0.0482\frac{\circ C}{W}$	$31.25\frac{\circ C}{W}$

Table 3.8: Numerical value used to estimate the maximum temperature gradient in the resin.

To make sure the hypothesis is always valid, the maximum power emitted from the cross linking is taken.

$$P_{crosslinking} = mHmax(\dot{x}) \tag{3.9}$$

Where $\dot{x}$ is the curing done in a one second step. The value obtained for the maximum heat power emitted is $0.6W$, combined with equivalent thermal resistance value, it gives a maximum temperature gradient of $1.91\circ C$. Given this is the worst-case temperature gradient that can occur with the curing cycle shown on figure 2.7, it is safe to assume the temperature is homogeneous enough for our study.

3.5.2 Thermal inertia

A transient thermal simulation was done in Ansys to verify the hypothesis of homogeneous temperature. The simulation aimed to be as close to the experiment described in chapter 4. The geometry consisted of the steel mold containing the resin as shown on figure 3.15

As for the material properties, they are the same as the other simulation and available in table 3.5.

The resulting gradient is shown on figure 3.16, where apart from the initial spike, the gradient is always below 1 degree. As for the spike during the beginning, it's origin is the transfer of the mold from the vacuum chamber to the oven. The details are available in chapter 4

During both simulation the strain gauge was neglected due to its relatively small size to the composite. The thermal inertia results will be compared to the experimental data. The strain gauge are monitored during the whole curing cycle, and during the beginning most of

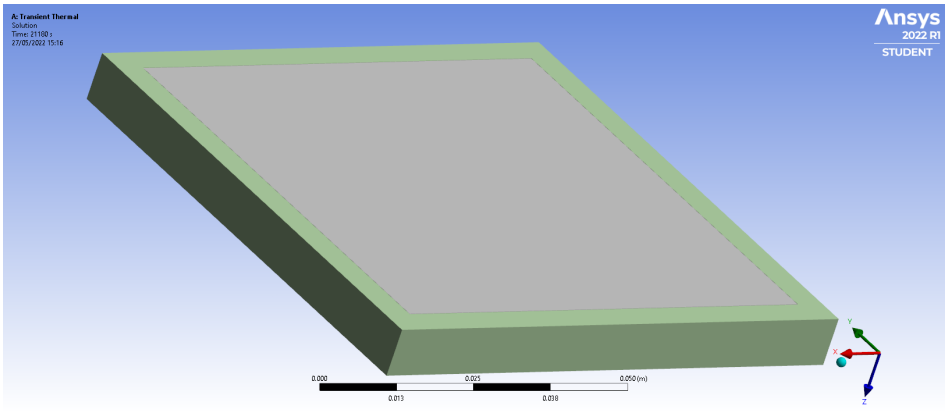

Figure 3.15: Thermal transient geometry.

the signal from the gauge comes from the temperature. This will give a coarse measurement of temperature until the gel point is reached.

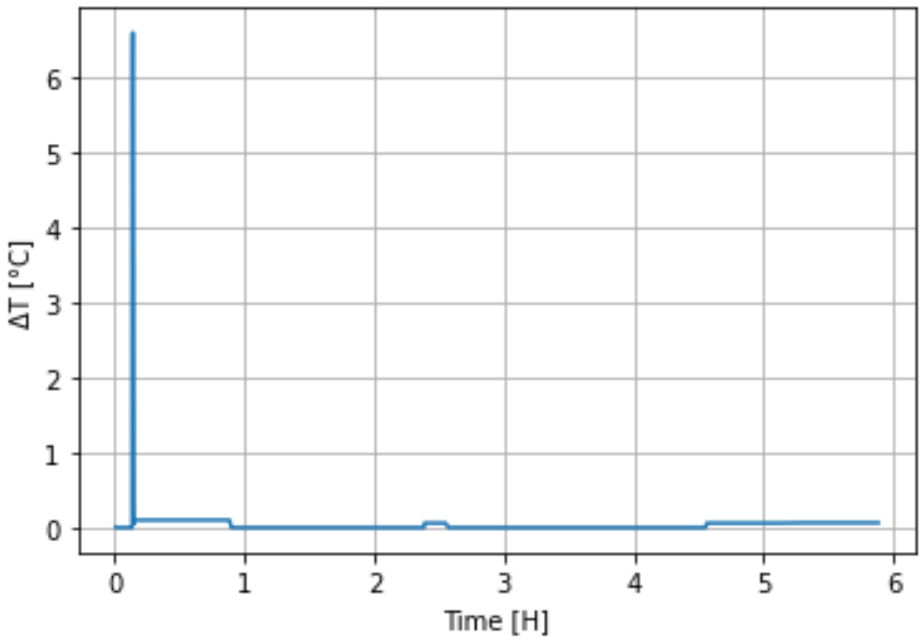

Figure 3.16: The temperature gradient throughout the curing of the resin.

3.6 Full transient simulation

The original goal for the simulations, was a full transient simulation of the curing process. This full transient simulation would then have been compared to all the simpler one to test the accuracy of a simplified model. Two mechanical models are required for the complete transient simulation of curing.

The first model is a viscoelastic model, it would be applied to the resin until the glass

transition temperature is above the temperature of the resin. Unfortunately, viscoelastic model requires many parameters to model. In addition to the classical linear elastic model parameters, The Young's modulus, the Poisson's ratio and the shear modulus, the viscoelastic model needs the shear relaxation modulus and the bulk relaxation modulus. As already shown in section 2.2.2, those materials properties change not only with the degree of cure but also with temperature making the already cumbersome model even more complex.

Then comes the second model, the linear elastic model of the resin who is no longer above the glass transition temperature. The model is simple and the properties while having a temperature dependence remains simple to obtain. The difficulty lays in the transition of material properties between the viscoelastic model and the purely linear elastic model. For example, the elasticity tensor between the gel state of the resin and the glassy state are not equal, and a transition is required. In Wucher and Martiny[55], the transition of the elastic tensor is linearly interpolated between the two values of the different states. In other such as Svanberg[69], the transition is abrupt.

The second linear elastic model is used as an approximation as it does not take into account the relaxation behaviour of the resin. In literature, the relaxation of the resin has been characterised in multiple ways, one of them involves a time-cure-temperature concept in [70]. Viscoelastic models are also used to describe the relaxation of the resin.

There exist some modules in Ansys that already do the full cure simulation, unfortunately it is not available to student, and setting up a custom script would have taken too much time.

3.7 Conclusion of Numerical Analysis

In this chapter all the numerical simulation that were done for the work have been presented. First was the choice of which software to use, which was more of a question of familiarity since the results remains the same in both software. Then came the simulation of the baked gauge, the gauge that will be shown next chapter in the experiment. Many sweeps were performed to understand what could affect the residual stress and if the analytical model in the previous chapter gave a similar trend. Afterwards came a simpler gauge, completely naked without any baking. The result ended up similar but with a small, surprising difference. Another geometry was also tested to observe the impact on the residual stress, surprisingly little difference was observed. Continuing, one of the important hypotheses was tested with a superposition of an analytical model for the heat generation and the simulation for the thermal inertia. Both showed very good agreements with the hypothesis, with the only exception being the transfer from the vacuum chamber to the oven. Finally, a brief explanation was done on the original goal of all the simulations and why it was not done.

Most of the numerical simulations remains coarse estimations and only covers the thermal mismatch at the end of curing. They can still give a good insight in to how the different parameters affect the residual stress. For example, very thin composite will yield lower residual stress and thickening said composite will quickly rise the stress until it reach a plateau. Interestingly, geometry has very little effect on the residual stress. This is one less parameter that can be used for reducing the stress, on the flip side, it allows for any shape of sensor to be embedded without worrying about increasing the risk of failure.

In the new chapter, the result will be compared to an embedded sensor.

Chapter 4

Experimental study

In this chapter, the experiments and their preparation are described. First the preparation of the embedding of the sensor which is as important as the different parameters for the stress to achieve a successful implementation.

Then it is followed by the result of the in-situ monitoring of the curing. The output of both gauges is then analysed first the strain output and then followed by the temperature for the first hour.

This finishes with the result of the bending test, where the gauges are strained higher than the aeronautic requirements. The static residual strain is also compared to what the analytical model gave and the result of the numerical simulations.

The two gauges used here are the following:

- Silicon gauge: BPY-1000-2.6-U-I-RL from BCM sensor technologies
- Metal gauge: CEA-05-250UWA-350 from Micro Measurments

4.1 Experiment plan

4.1.1 The Initial plan

The original idea for the experiment was to implement a sensor inside a stack of carbon fiber who then be processed in an RTM press. The gauge would have been implemented between the first and second plies just as shown on figure 4.1.

The objectives were the following:

- Observe any gauge failure.
- Measure the strain from the gauge.
- Test the maximum strain until failure.

Unfortunately, the process needed to cut away around 1 cm of every sides. The cutting is needed as the weaves degrades near the cut sides, just as shown on figure 4.5. The connection to the sensor would then be lost as the cable would be cut away with the composite, leaving

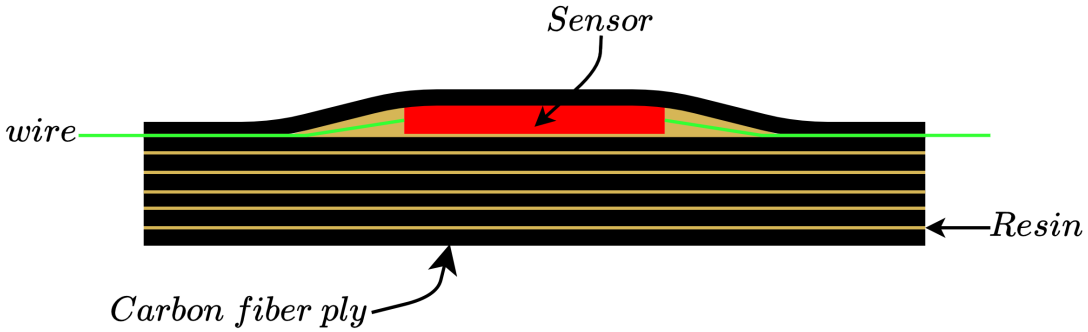

Figure 4.1: The original experiment.

only the cross section of the wire. The wire being less than a millimetre thick would have been extremely hard to make contact with.

Another point that was overlooked was the fact that carbon fiber are conductive and thus without proper insulation of the sensor from the weave, it would have been shorted. This can easily be addressed by enveloping the sensor in a little bit of resin before putting it in the stack.

The contact with the sensor may have been resolved in two different solutions. The first would be to make the wires go through the plies of carbon fiber. As shown on figure 4.5, the wires are small enough, that they could potentially pass through the plies in between the tows. This method would result in a distortion on weave around the fiber which would be unacceptable for aeronautics CFC but would allow to test a gauge inside a stack of carbon fiber. The second method is more complex and requires either the cooperation of the carbon fiber manufacturer or additional treatment. It consists of using the conductivity of the carbon fiber itself. By connecting the sensor to a a specific tow who hasn't been coated to insulate it, after the cut and polishing of the composite, the connection can be done by simply contacting the right tow on the external surface.

4.1.2 The second plan

Since embedding the sensor and getting a reading after the processing of the CFC would be overly complicated, we switched to a surface mount for the sensor. Two sensors were prepared, one which had its wire going out of the mold for an in situ monitoring of the cure. The second sensor would have it's cable remain in the mold where they wouldn't be trapped in resin just as shown on figure 4.3.

The transparent layer atop the sensor is a sheet of Teflon. It is used in this case to the wires to be freed from the resin without damaging either the wire or the composite. The diagrams on figure 4.3 show the process of freeing the wire. The resin doesn't stick to the Teflon sheet, allowing us to lift off the resin layer above it. Since that layer is very thin, it can easily be broken without damaging the wire, freeing them and allowing us to take measurement.

For the wires going out of the mold, they would be connected to a digital multimeter.

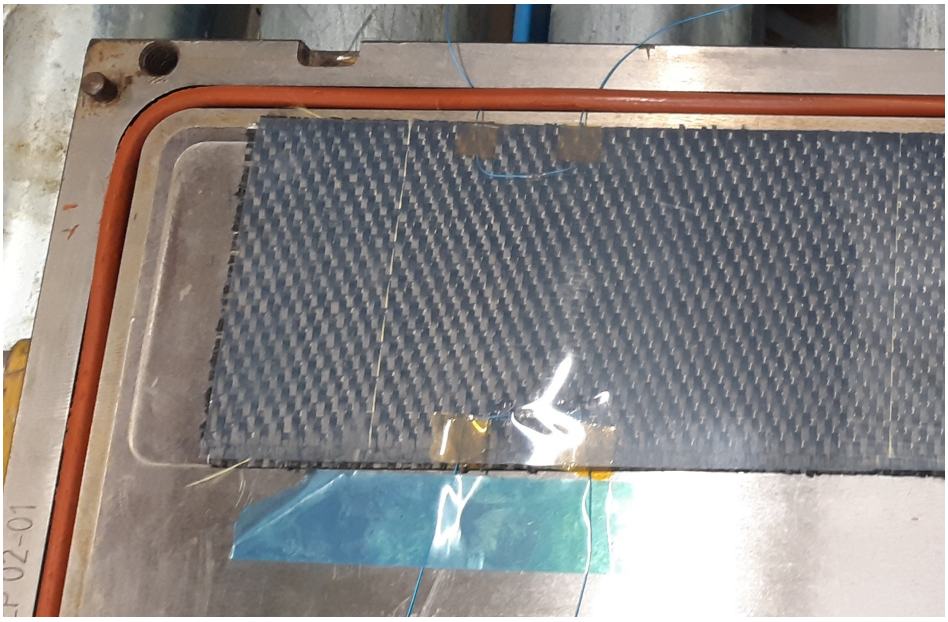

Figure 4.2: The two sensors with their respective position.

The mold while made out of steel, would not short the wire even if their jacket was stripped. This is due to all the surface treatment of mold, to avoid having the resin of the composite stick to the surface of the mold, it is coated in release agent. The release agent here made the mold completely non conductive from any surface.

As already mentioned in section 2.1.3, the analytical model does not consider the position of the sensor, the results could thus be compared without any modification to the analytical model. The numerical analysis on the other hand predicted reduced stress at the top of the resin, even when the sensor was surrounded by resin but close to the surface which would have been the case here. This experiment would have also shown if the strain gauge could have survived an RTM process.

Unfortunately, the mold had a leak, and the vacuum could not be formed properly. It was later found that the leak came from the input valve of the resin, and due to a time constraint at that point, the experiment was switched.

Before this experiment was switched, the research of the leak had taken its toll on the sensor. To search the leak and verify each of our assumption we had to take out the mold out of the press, open it, get the samples out and then back in. At some point, the samples were kept out of the procedure, but not before going through the cycle a few times. Before starting the new experiment, both gauges had to be soldered back as the resistance of either could not be measured any more. During that time both gauges had already been soldered back once, but this time only one of the gauge could be brought back as the other lost the golden wire connecting the gauge and the solder pad. The damaged gauge is shown on figure 4.6. This also serves to illustrate how much care is required when manipulating such small gauge and why naked gauge weren't used in this experiment.

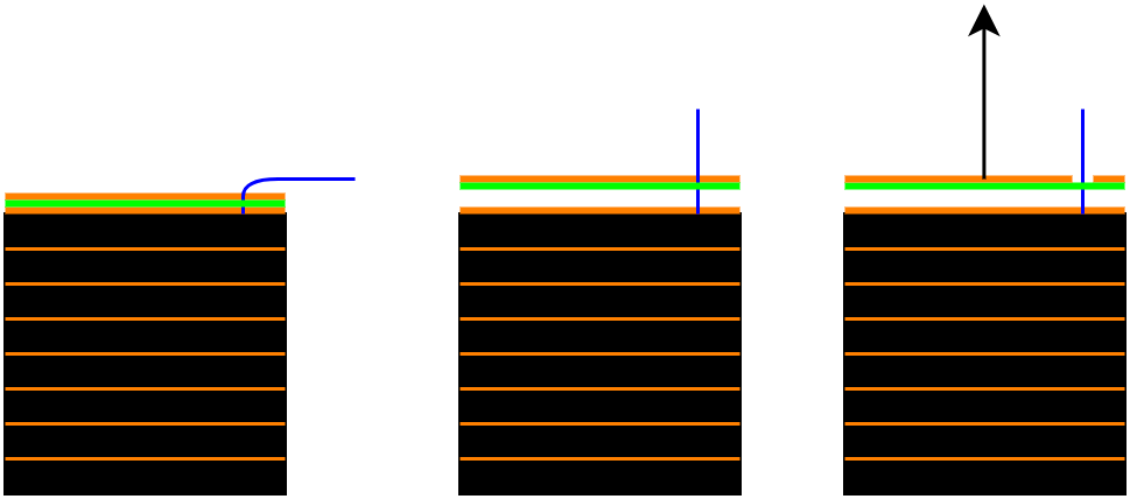

Figure 4.3: Procedure to free the wire from the resin. Wire in blue, resin in orange and the carbon fiber in black.

4.1.3 The third plan

The third plan was simply to put a gauge inside a block of resin then cure it in an oven. While this is simplified compared to the CFC manufacturing, it has the advantage of being a worst-case scenario since the CTE mismatch is the highest between the strain gauge and resin. There was also the added benefit of simplifying the in-situ monitoring of the cure since the curing would occur in a simple oven.

To replace the irreparably damaged silicon gauge, a metal strain gauge from Micro Measurment was used. Both silicon and metal gauge where then taped to the bottom of the mold which was filled with liquid resin afterwards.

For the In-situ monitoring, two Keithley 2000 digital multimeter were used, one for each sensor. The wires of each sensor were passed through the door of the oven and connected with a small clamp to the multimeter. The oven used and the cured sample still connected to the multimeter can be seen on figure 4.8

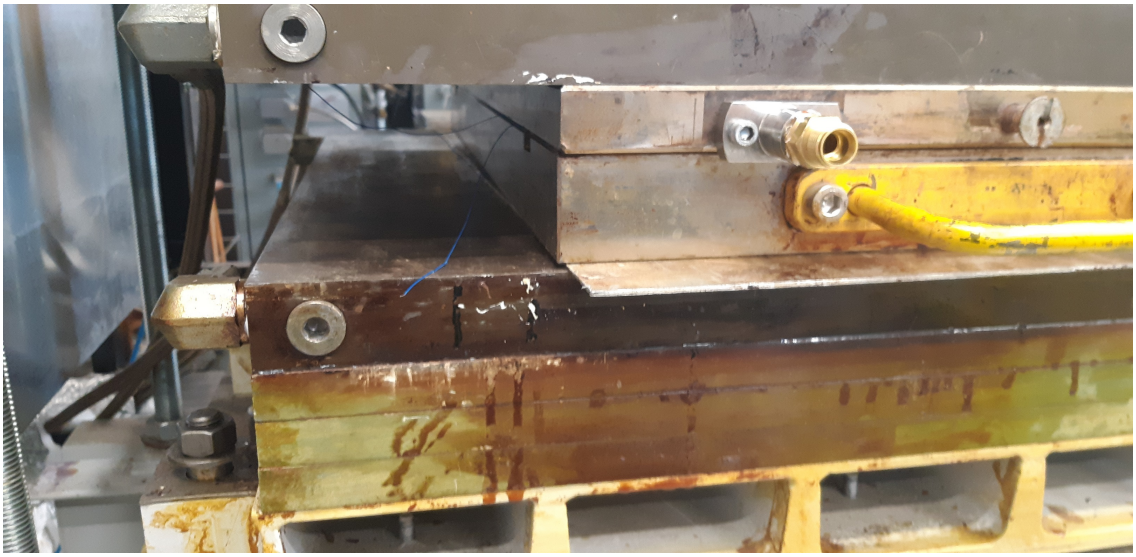

Figure 4.4: The exiting wire for In-situ monitoring of the cure.

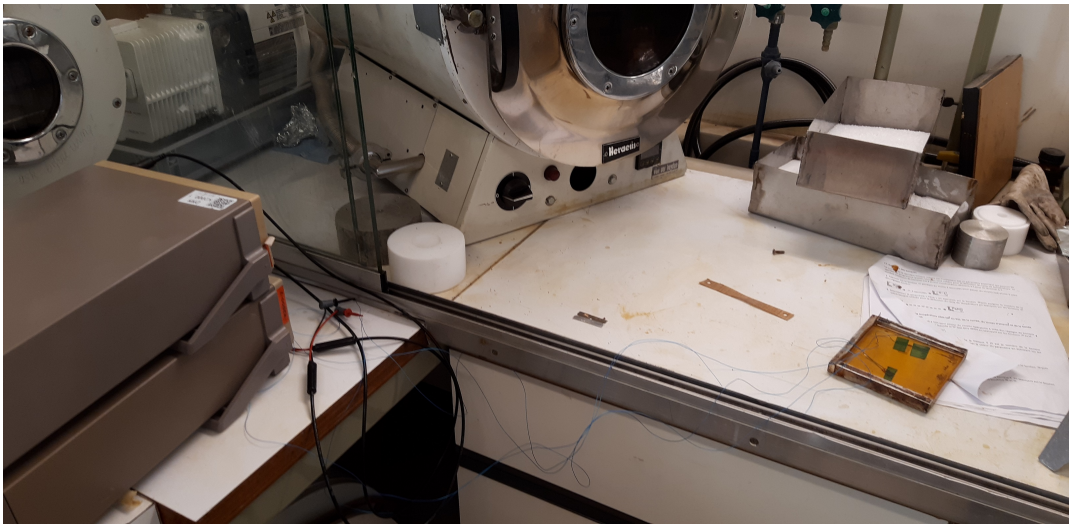

Figure 4.8: The sample, oven and multimeter at the end of the curing cycle.

4.2 Experiment

The total curing cycle of the RTM6 resin took 5 hours and half to complete. But even before the curing could begin, a few preparations steps had to be done.

4.2.1 curing

The first step of the preparation consisted of coating the entire mold with release agent, otherwise the sample would not have come off.

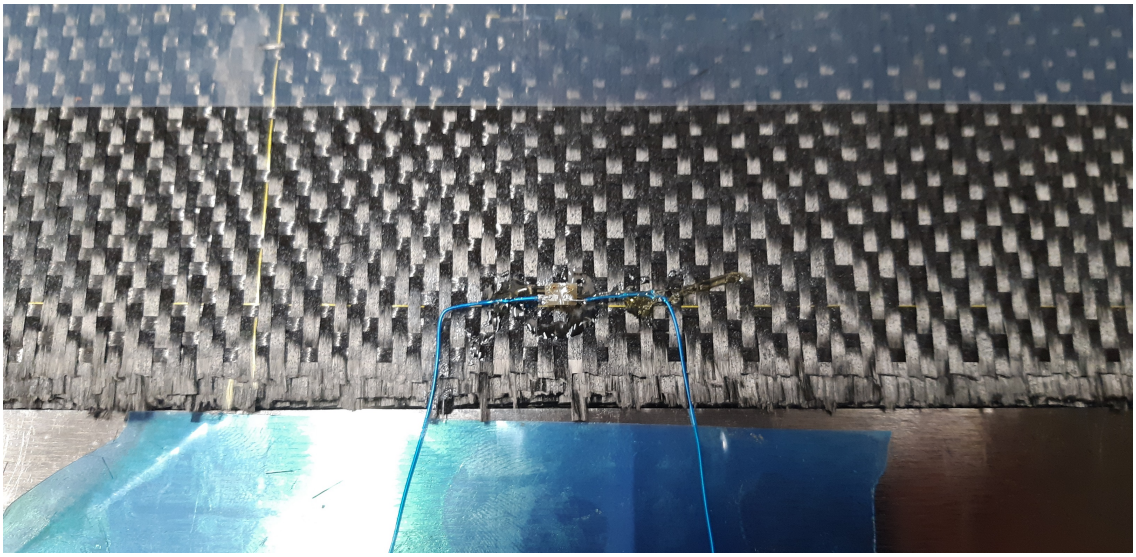

Figure 4.5: The second alternative and clear quality degradation of the weave at the sides.

Afterwards each of the gauges were fixed to the mold via tape. Due to the different way the gauge were connected to the wires, the tapes were either put on the wire or on the gauge itself. The goal of the tape was to keep the gauge from floating and keep them parallel to the mold.

The mold was then filled with RTM6 epoxy who had been heated up from the cold storage. Before the curing could begin, one last step was required. To keep the number of voids within the resin, it was put in a vacuum chamber for 8 minutes at $90°C$ to degas, the it was transferred into the oven. The recording of the strain gauge resistance began during the transfer.

4.2.2 Result

The recorded resistance throughout of both gauges are shown on figures 4.10a and 4.10b. The little dip at the beginning is due to the transition from the hot vacuum chamber to the hot oven passing by the ambient air. The initial values for both gauges were taken with a multimeter. The measurement of the silicon gauge is shown on figure 4.9. The initial silicon gauge resistance was 1069Ω and the initial resistance of the metallic gauge was 349.8Ω

The absolute values for the metallic gauge are an anomaly, unfortunately it was noticed much later. Despite the value having a clear anomaly, the trend of both gauge remains very similar, with the silicon greater sensitivity amplifying the signal compared to the metal low sensitivity. This trend is also observed in the literature, in [71], at vitrification a dip in the strain is observed.

The value of the observed strain with the temperature correction is shown on 4.11b, this value for strain is much higher than what is expected. But the most bizarre part, is the fact this value goes back to what was expected when the bending test was performed as shown on figure 4.18. Multiple sources of error have been compiled in the following list, but it was not investigated further due to the time between the experiment and the discovery of the

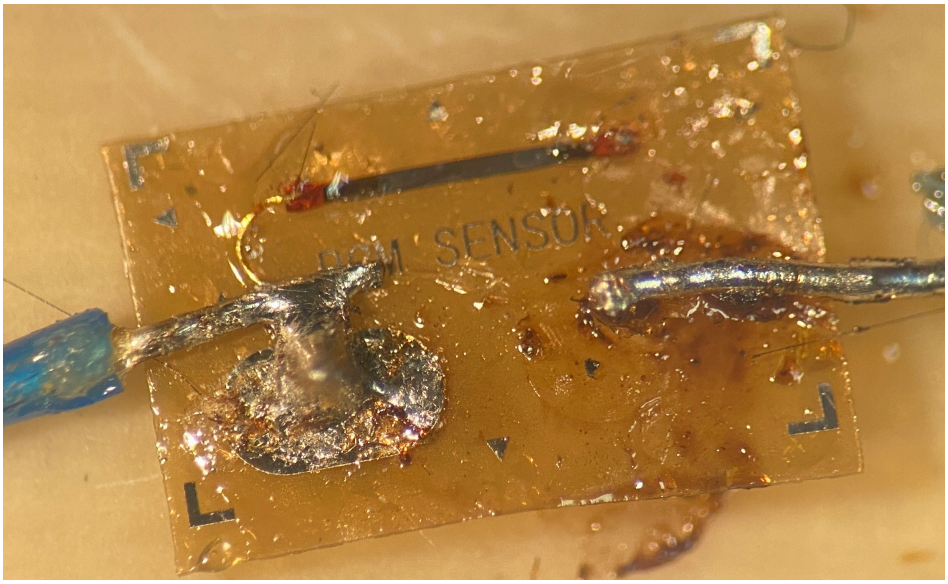

Figure 4.6: The right gold lead and solder pad are missing, rendering the gauge inoperable.

anomaly.

- The multimeter was not well calibrated.
- The tape was putting strain on the gauge.
- A big parasitic parallel resistance was present.
- The initial resistance measurement was erroneous.

Converting the resistance value of the gauge to strain is not as straight forward as just using equation 1.2. Due to the temperature of the gauge, first its thermal output needs to be computed and then subtracted. The computation of the thermal output of both the metallic and the silicon gauge have been done in section 2.3. The result from using those analytical models to offset the strain gauge output is shown on figure 4.11

As already mentioned above, the expected absolute value for the metal resistance were off by a few Omhs which leads to the gauge reading a percent of deformation throughout the cure. This unfortunately renders the extraction of the temperature from the gauge all but impossible.

For the silicon gauge, the analytical model seems to overcompensate the effect of temperature on the gauge. This could come to multiple reasons which are listed here:

- The analytical model predicts a higher increase in resistance than reality.
- The change in the gauge factor of the gauge is not considered.
- The temperature of the curing cycle is not the temperature of the gauge.
- The effect of the baking is not considered properly.

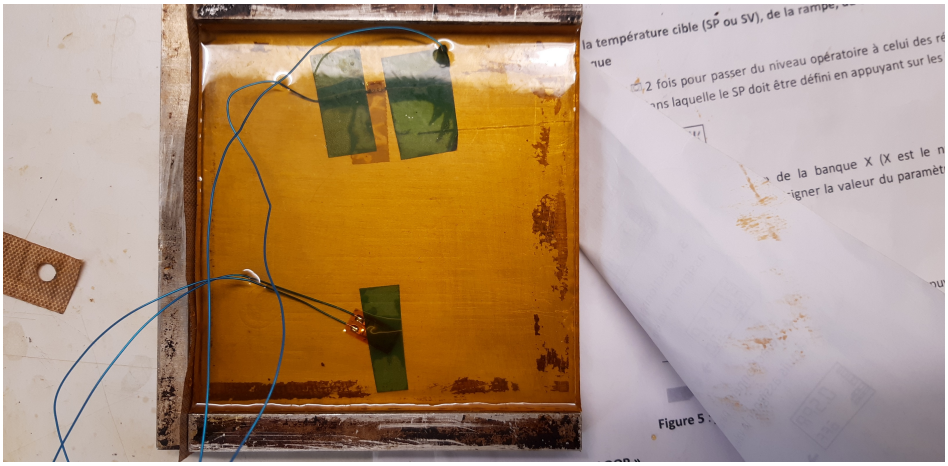

Figure 4.7: The placement of the two gauges in the resin.

Thermal resistance overestimation

For the first possibilities, on the package of the manufactures the resistance shift due to temperature is estimated to be $TCR \leq 0.4\% \pm 10\%$. Compared to the increase of the analytical model it is indeed smaller but the gauge is rated for temperature up to $125°C$ for static application. The higher rating of $190°C$ for dynamic application is normally only sustainable for two hours, meaning the resistance shift given by the manufacturer might not be valid anymore. The comparison between the analytical model and the manufacturer shift is given on figure 4.12a and the strain extracted with the manufacturer shift is given on figure 4.12b.

Now instead of overcompensating the thermal output, it is under compensating. It was shown with the model of curing in section 2.2.1, that the glass transition only occurs in the middle of the 160 $°C$ plateau, before that the resin is liquid and thus most strain should be negligible. Despite this with the manufacturer data, we are still observing nearly a $1000\mu\epsilon$ right at the glass transition.

Neglected Gauge factor

Since very little are predicted to appear during the early phase of curing, the influence of the temperature on the gauge factor was neglected. The gauge factor is expected to lose half of its value when the gauge reach a temperature around $125°C$. By taking the effect of temperature on the gauge, the readings of the gauge are amplified as shown on figure 4.13.

The addition of the variable gauge factor also smoothed out the strain variation at the end of the curing. This is due to the much lower gauge factor during the $180°C$ plateau which registered a much greater strain and the subsequent cooling strain shift which remains nearly unchanged.

Wrong gauge temperature

Figure 4.9: Multimeter measurement of the silicon strain gauge.

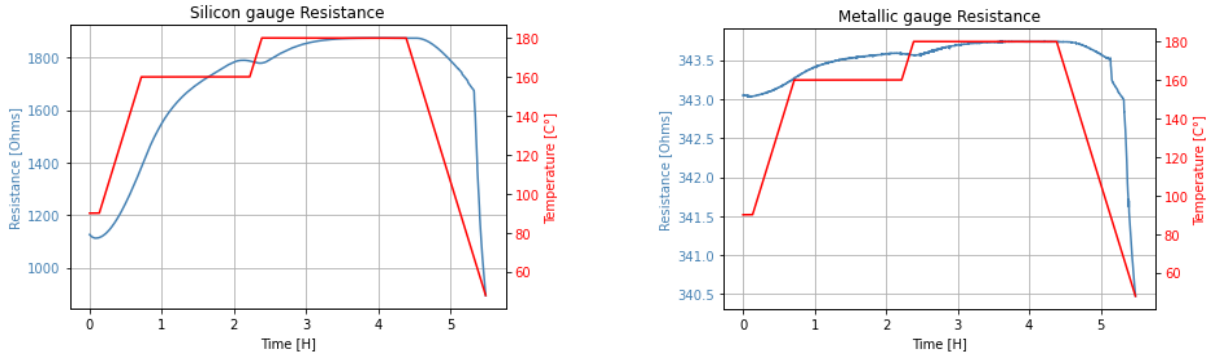

(a) Silicon resistance through curing

(b) Metal resistance through curing

Figure 4.10: Strain gauge resistance evolution throughout curing.

This is likely to be the major source of the inabilities to properly compensate the thermal output of the gauges. Up until now, it was assumed the temperature of the gauge matched the temperature of the curing. This hypothesis was even verified in section 3.5.

While the oven had a thermometer to control the curing cycle, the data of said thermometer was not logged. Instead to extract the temperature of the oven, the silicon strain gauge will be used. One of the major hypotheses done in this work and many work from the literature, is that during the curing, before the gel point, the resin generates a negligible amount of stress and thus strain. This will allow to extract a very rough estimation of temperature from the embedded gauge.

We will use both the manufacturer estimation and our analytical model for the resistance change due to thermal effect. The temperature can be extracted roughly from the following

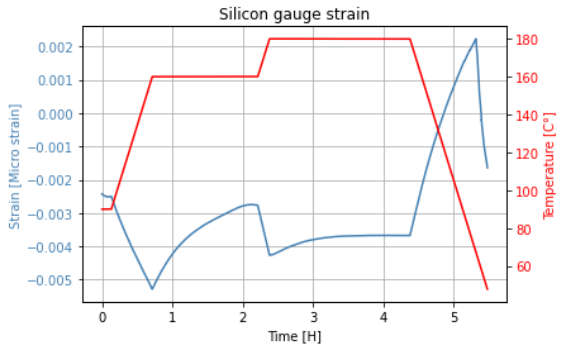

(a) Silicon gauge output through curing

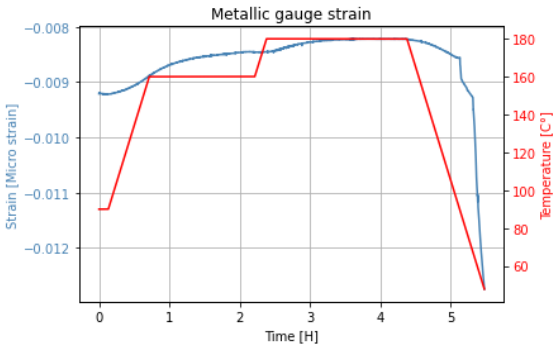

(b) Metal gauge output through curing

Figure 4.11: Strain gauge resistance evolution throughout curing.

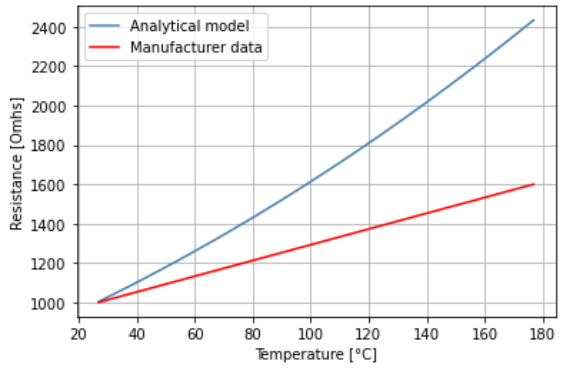

(a) Resistance evolution comparison

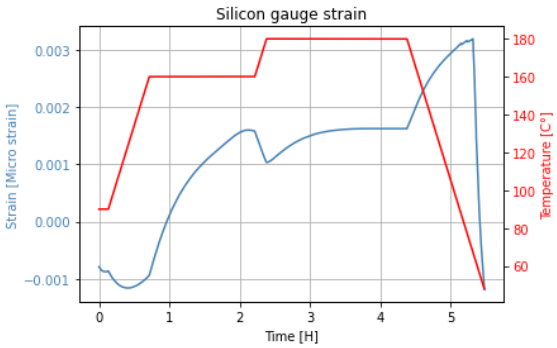

(b) Silicon strain with manufacturer thermal offset.

Figure 4.12: Manufacturer resistance offset due to temperature.

equation.

$$R(T) = R_0 + R_0 * 0.4\% * (T) \rightarrow T = \frac{R(T) - R_0}{0.4\% R_0} \tag{4.1}$$

Where T is the temperature above ambient of the gauge in $°C$ and R_0 the temperature of the gauge at ambient temperature. As for the analytical model, the extraction of the temperature necessitates the help of a computer.

To avoid measuring the strain as temperature, the temperature is only extracted for the first hour.

Figure 4.14 shows a wide gap between the measured temperature and the curing cycle temperature. Between the linear manufacturer model, which is the most optimistic in this case, there stand a $40°C$ gap. This gap shrinks as the curing enters the first temperature plateau. As for the analytical model, the gap widens to $60°C$ and continues to widen during the ramp, only catching up during the plateau.

Such a discrepancy cannot be overlooked, even if the strain gauge are not good thermometers. A few causes could be the origin of such a huge difference.

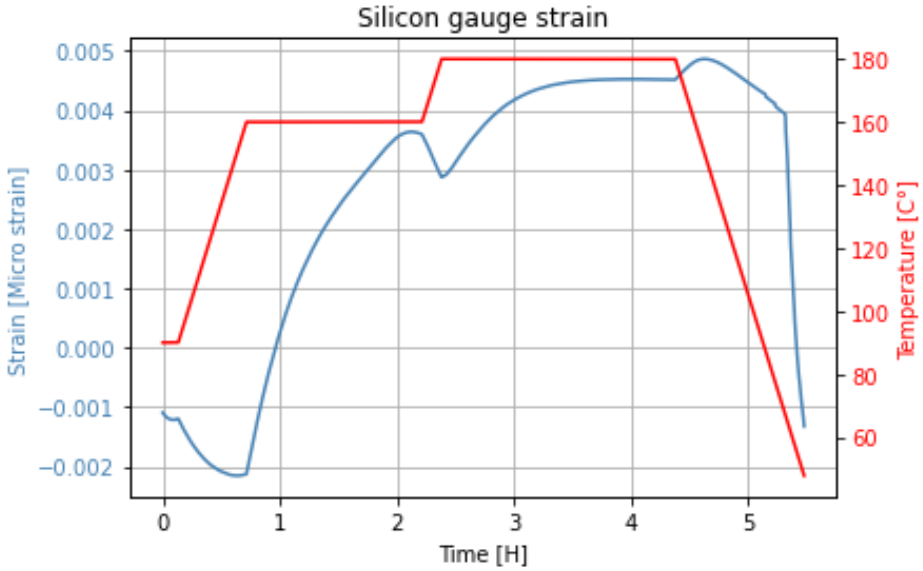

Figure 4.13: Strain with manufacturer resistance and gauge factor compensation.

- The gauge was already under strain due to the tape.
- The mold or the resin was not as conductive as hypothesised.
- The oven did not follow the curing cycle correctly.
- The contacts of the gauge were damaged due to the previous preparations.
- None of the used model represent the gauge evolution to temperature correctly.

To avoid such blunder for future experiment, an external thermometer should always be employed.

4.2.3 Bending Test

Verifying if the sensor can handle the residual stress is only the first step, as the sensor needs to be able to handle the additional strain that the composite is going to be subjected throughout its life.

Continuing with the aeronautic specification, a composite aircraft structure allows for a maximum of $3000\mu\epsilon$[72]. The block of resin was cut into two pieces to isolate each strain gauge, it should have been rectangular pieces of resin. Unfortunately, the metallic strain gauge shifted during the curing resulting in a trapezoid shape as shown on figure 4.16. The dimensions of the samples are available in table 4.1

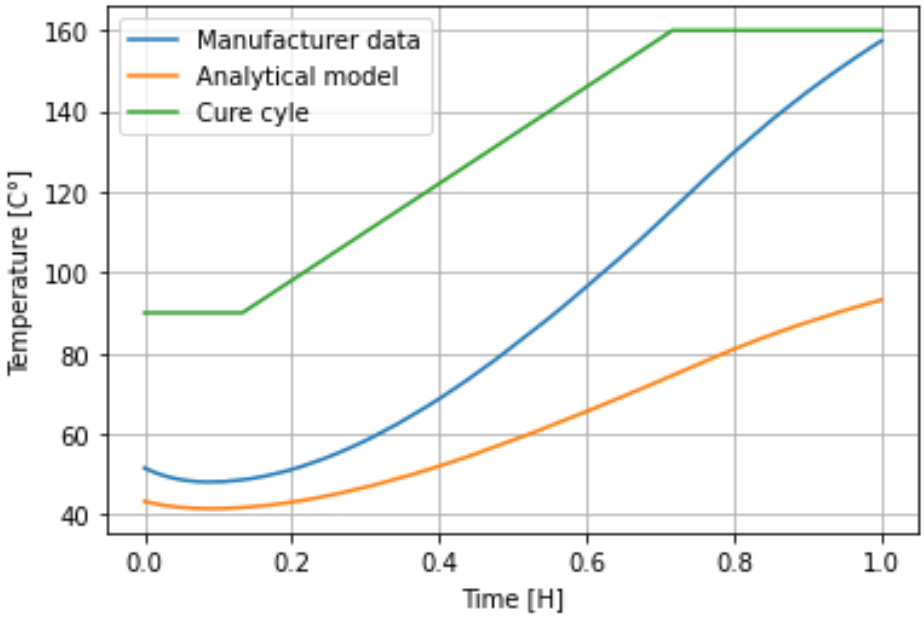

Figure 4.14: Temperature measurement of the silicon gauge for the first hour.

	Length	Width	Thickness
Metallic Gauge	100mm	65/20mm	4.6mm
Silicon Gauge	100mm	27mm	4.6mm

Table 4.1: Resin pieces dimension with the stain gauge embedded

The bending test consisted of a four point bending test with each of the supports spaced apart by 2 cm for a total of 6 cm for the two furthest support. The resistance of each gauge is measured by a Keithley 2000 digital multimeter. The test is shown on figure 4.17

The equation for measuring the strain on the sensor is given by the ASTM D7264-07 standard.

$$\epsilon = \frac{4.36\delta h}{L^2} \tag{4.2}$$

Where ϵ is the strain at the outer surface. It is also considered as the strain on the gauge, which considering the strain gauge were tapped to the bottom of the mold is accurate enough. δ is the mid-span deflection which is controlled by the bending device with the handle. h is the thickness of the sample, in our case the thickness of the resin slab. L is the length of the support span, the distance between the two outer support.

On figure 4.18, the initial value of the gauge at 0 applied strain is around 347.1 Ω this combined with the gauge factor of 2 results in a static strain of 3716$\mu\epsilon$. Which is much lower than registered during the curing shown on figure 4.10b. This value of strain is around half the expected strain value with the simplest bi-layer analytical model and the value of Constantan which is the alloy used for the gauge. The multi-layer analytical model give a closer estimate at 5487$\mu\epsilon$.

Experiment measurment	Bi-layer Analytical model	Multi layer Analytical model
3716	7490	5487

Table 4.2: Metallic gauge residual strain comparison

By converting the resistance to a strain signal, we can compare the applied strain to the measured strain of the gauge. The first observable point is the factor 2 of difference between the applied strain and observed strain, this factor increases to 3 at high strain. The second point is the non-linearity of the observed strain.

The difference in observed strain and applied strain could be attributed to either the non-linearities or a mistake during the experiment. The contraption for bending requires the marking of the needle valve to be halved, this could have been done twice, explaining part of the difference. Even by multiplying the applied strain by two, the error would not be completely erased, this point to another source of error. One of those sources could be the non-linear response of the resin.

For the silicon strain gauge, the strain was tested both in compression and tension, this was not done for the metallic gauge due to the triangular shape not fitting well in the test device. There is also a small error between the applied strain and the measured strain albeit smaller than for the metallic gauge. The non-linearity of the gauge can also clearly be seen. This non-linearity can be attributed to two sources, the first one is simply the non-linearity of the strain gauge. The manufacturer includes in the data sheet of the strain gauge a small amount of non-linearity for strain up to a $1000\mu\epsilon$. For the gauge used, the non-linearity is rated at $\pm 0.2\%$. Since we are at much higher strain, we can expect a much higher non-linearity. As for the second source of error, this could come from the viscoelastic properties of the resin. The viscoelastic model adds a time dependence to the materials, this can e observed partially at 0 applied strain, where we can see the materials not quite coming back to it's original shape. This is further exacerbated by time as a measurement of both gauges three month later yielded different value of resistance as shown on table 4.3.

	Immediate	3 month later
Silicon gauge	504	614
Metal gauge	347.1	348.8

Table 4.3: Relaxation of resin measured by strain gauge.

On table 4.4, the different prediction of the analytical models and simulation are compared to the observed strain at the end of the experiment. Interestingly, despite having predicted a higher residual stress and thus strain since the modulus are very similar between silicon and Constantan, the silicon gauge actually registers less residual strain than the metallic gauge. Another point is that even with just the thermal mismatch alone, the models are predicting a higher residual stress than what is observed in spite of neglecting the chemical shrinkage. From the data in table 4.3, this could be attributed to the relaxation of the resin which occurs with time.

Experiment measurment	Bi-layer Analytical model	Multi-layer Analytical model	Simulation
3526	9282	8483	4411

Table 4.4: Silicon gauge residual strain comparison

4.3 Conclusion

In this chapter, the preparations for embedding the sensors in CFC were described. The evolution of how the experiment changed from embedding the sensor, to putting it on the surface, to finally embed it in a pure resin slab was shown. The success of an embedded sensor relies just as much on a good preparation of the embedding as the right choice of parameters. Often time, the handling of the tiny sensor proves to be as much a difficulty as the residual stress.

The result of the in-situ monitoring of the cure were shown and analysed. An attempt at extracting the temperature was also made but yielded poor result, either due to a false hypothesis or the experiment not being followed properly.

Finally, a bending test was performed on both sensors to verify their ability to be used, which both gauges passed without trouble. It also highlighted the non-linearity of the gauges and a non-negligible error in their readings. The error would need more examination for the gauge to be used properly.


NICKELE
ACIAP

NICKELÉ
ACIAP

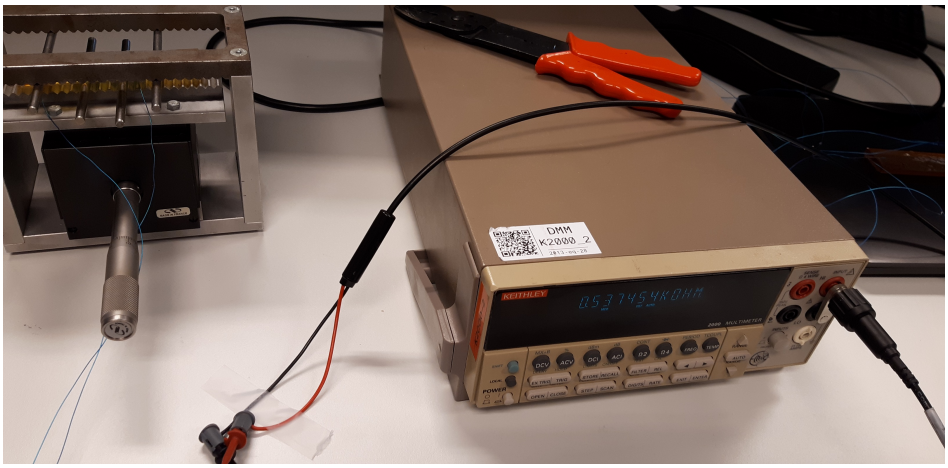

Figure 4.17: Bending test set-up.

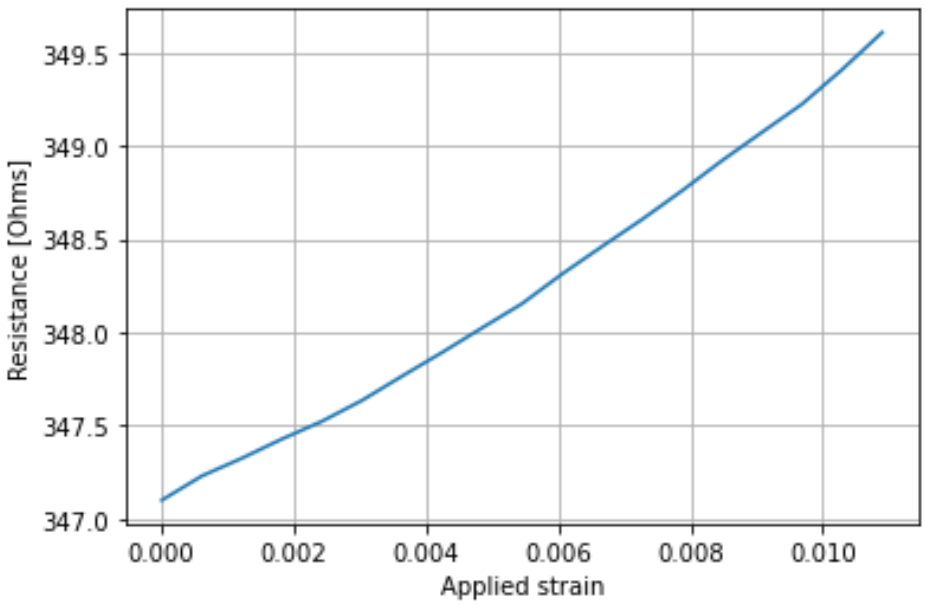

Figure 4.18: Metallic strain gauge resistance Vs applied strain.

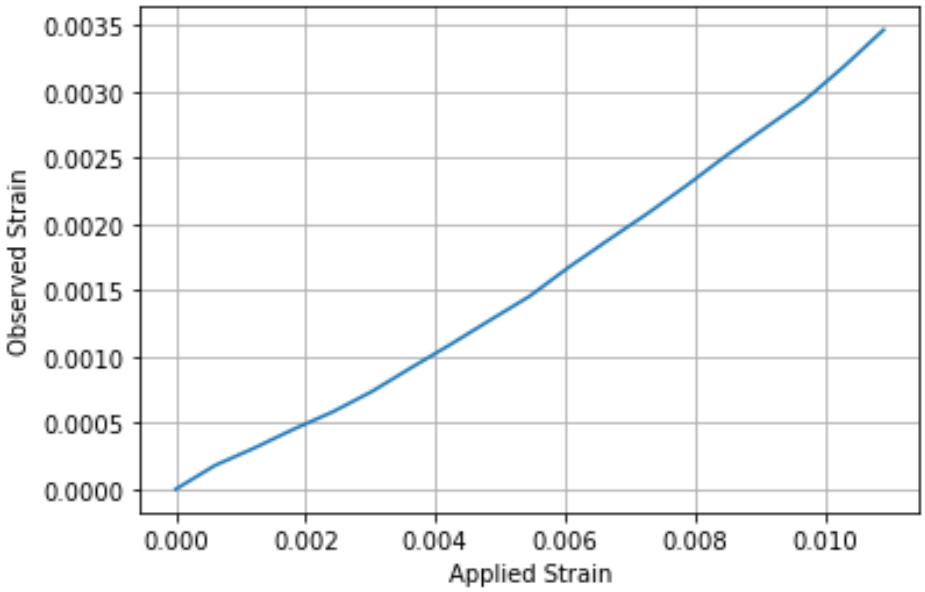

Figure 4.19: Metallic gauge measurement Vs applied strain.

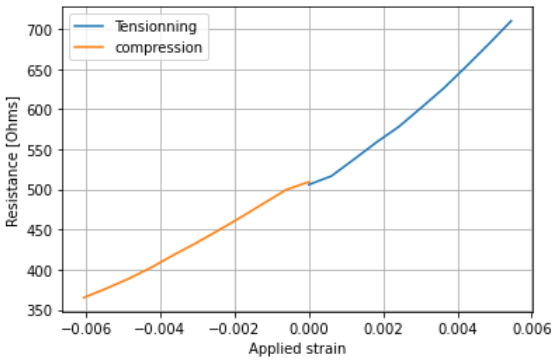

(a) Silicon strain gauge resistance Vs applied strain

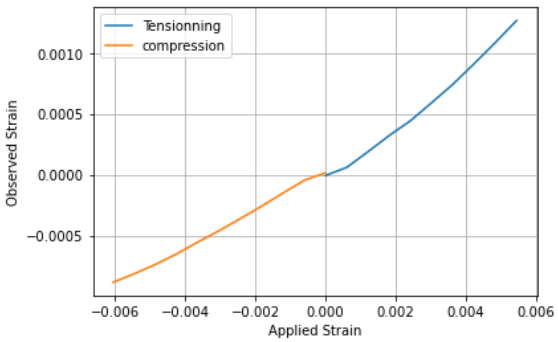

(b) Silicon strain gauge measurment Vs applied strain.

Figure 4.20: Silicon strain gauge bending test.

Conclusion

In the first chapter, the nature of carbon fiber was presented, afterwards all the different configuration of the fiber alone was described. Then the different matrix family were presented followed by the different manufacturing method to obtain a composite. All of this served to highlight the sheer number of possibilities available when working with composites. All those possibilities rendered the initial idea of verifying the possibilities of embedding a sensor inside said composite nearly impossible. While an experiment would work for one particular combination, the other combination would have no guarantee to work. This shifted the goal of this work from verifying the possibility to embed a sensor in a composite to find models that would allow us to predict which parameters affected the residual stress which is one of the main concerns for embedded sensor. One of the first parameter that could be analysed is the sensor itself, multiple type of sensors were presented with their advantages and drawback in embedded application. Then a review of the literature over embedded sensor in any composites was done to show the priorities in the field. The use of semiconductor strain gauge in embedded application was strangely absent from the literature.

For the second chapter, different analytical models were first proposed to obtain a rough estimation of the thermal stress. First the simplest model with Stoney's approximation, requiring very little computation, then the multi-layer Chun-Hway Hsueh model requiring a bit more computation. From those models, the different parameters that influenced the residual stress were extracted and sweeped. From the sweep, the different trends were obtained showing the sensitivity of the residual stress over the different parameters. Afterwards, the resin curing was detailed to show the impact of the curing on different important parameter of the residual stress. For example, how the curing cycle impacts the glass transition temperature and thus the differential temperature used to compute the residual stress. This point is important as even with the same resin, with a different curing cycle, the result may differ. Since most materials properties are dependant on temperature which change all along the curing, some approximation had to be made. Fortunately, most properties have a linear dependency on temperature, allowing average to be taken without generating errors. Even for the slightly non-linear Young's modulus, the error is negligible. To compensate the temperature output of the gauges during the in-situ monitoring, a model for the resistance change in silicon was investigated.

The third chapter present all the result of all the numerical analysis. It begins with the comparison of two softwares for simulation, where a case study resembling our original problem is presented. All the modules required for the simulations are presented with their default value. The meshing is also compared as both softwares have their built-in mesh

builder. At the end of the case study, it is shown that both softwares are equivalent, the choice is thus more personal. Afterwards the first sensor geometry is analysed, the gauge with a baking. An attempt at simplifying the geometry is made but quickly fails, instead the simulations are done with a full geometry. The first parameter to be analysed is the position of the sensor, in the analytical model there was no influence of the position on the stress. The numerical analysis diverged from the analytical model, the closer to the surface the less the stress on the gauge. Then came the analysis on the corner singularities. To verify whether singularities were present in the simulation, a comparison between a fillet geometry without any angle and a simple block with all 8 angles was done. The difference of maximum stress between the two were small enough to dismiss singularities. Two sweeps where the performed on the resin total thickness and the temperature differential to compare to the analytical result. Both showed the same trends while their absolute values were slightly different. The same analysis was the done on a naked gauge geometry without the backing showing similar result with a small surprise. Finally, a simulation and a small analytical model were used to confirm one of the important hypotheses: An homogeneous temperature.

The result from both analytical model and numerical analysis were then compared to our experimental result. Unfortunately, due to the missing temperature data, the comparison during the in-situ monitoring could not be done properly. But the final residual stress post curing for the silicon gauge were predicted quite accurately by the simulation. And while the analytical model gave a good order of magnitude estimation, they were still off by a factor of two or more. Even with the corrected Young's modulus, CTE and glass transition temperature. Afterwards a bending test to confirm the ability of the strain gauge to function at such high stress was done. The applied strain was twice and thrice the maximum expected strain for aeronautic in the case of the silicon gauge and metallic gauge respectively. This highlighted a few important aspects about the embedded sensor. The residual strain alone pushes the gauge far into a non-linear range, with the additional external strain it goes even beyond its rated limit of $5000\mu\epsilon$ for the silicon strain. While the silicon strain gauge still functions, work need to be done to obtain correct signals. As for the metallic gauge, it is still within its expected range as it can strain up to 5% which is high above the CFC limit. It has two drawbacks, the increased energy consumption and bigger size.

Possible improvements and future works to take this study further:

- Characterize the response of semiconductor gauge embedded in resin and composites under the residual strain at different time.(Immediatly after curing, 1 month after, 3 month after).
- Experimentally test the validity of the models and simulation by experimenting with different resin.
- Study the fatigue life of the strain gauges under such residual stress. While the gauge was tested once outside its specification, for SHM, the gauge has to have a fatigue life equal or greater than the one from the composites otherwise it defeats the purpose.
- Repeat the experiment with embedded in resin and in-situ measurement with a temperature sensor and a controlled curing cycle.

- Implement the whole wireless SHM device.
- Test the possibilities of using small patches of glass fiber for wireless transfer in a carbon fiber composite.
- Test an embedded sensor between two carbon fiber plies, with connecting wire going through the ply.

Bibliography

[1] M. Behr, J. Rix, B. Landes, B. Barton, G. Billovits, E. Hukkanen, J. Patton, W. Wang, D. Keane, and S. Weigand, "High-temperature tensile cell for *in situ* real-time investigation of carbon fibre carbonization and graphitization processes," *Journal of Synchrotron Radiation*, vol. 23, pp. 1379–1389, Nov 2016.

[2] A. Karuppiah, *predicting the influence of weave architecture on the stress relaxation behavior of woven composite using finite element based micromechanics*. PhD thesis, 12 2016.

[3] S. Das, J. Warren, D. West, and S. M. Schexnayder, "Global carbon fiber composites supply chain competitiveness analysis," 5 2016.

[4] M. Ashby, *Materials Selection in Mechanical Design*. Elsevier Science, 2016.

[5] R. Nur, N. Matsuhisa, Z. Jiang, M. O. G. Nayeem, T. Yokota, and T. Someya, "A highly sensitive capacitive-type strain sensor using wrinkled ultrathin gold films," *Nano Letters*, vol. 18, 08 2018.

[6] P. Moyo, J. Brownjohn, R. Suresh, and S. Tjin, "Development of fiber bragg grating sensors for monitoring civil infrastructure," *Engineering Structures*, vol. 27, no. 12, pp. 1828–1834, 2005. SEMC 2004 Structural Health Monitoring, Damage Detection and Long-Term Performance.

[7] K. Schaaf, "Composite materials with integrated embedded sensing networks," 2008.

[8] C.-H. Hsueh, "Modeling of elastic deformation of multilayers due to residual stresses and external bending," *Journal of Applied Physics*, vol. 91, no. 12, pp. 9652–9656, 2002.

[9] V. Kaajakari, *Practical MEMS*. Small Gear Pub., 2009.

[10] S. Park, *Carbon Fibers*. Springer Series in Materials Science, Springer Netherlands, 2014.

[11] Y. Kim, Y. Kim, C. Lee, and S. Kwon, "Thin polysilicon gauge for strain measurement of structural elements," *IEEE Sensors Journal*, vol. 10, no. 8, pp. 1320–1327, 2010.

[12] H. Corporation, *HexFlow RTM6 180C Mono-component epoxy system for resin transfer moulding and infusion technologies*. Hexcel Corporation, 281 Tresser Blvd, 16th Floor, Stamford, CT 06901, USA 203-969-0666, 2018.

[13] M. Kinsella, D. Murray, D. Crane, J. Mancinelli, and M. Kranjc, "Mechanical properties of polymeric composites reinforced with high strength glass fibers," *International SAMPE Technical Conference*, vol. 33, 01 2001.

[14] C. Cavallo, "All about 6063 aluminum (properties, strength and uses)."

[15] M. Azo, "Stainless steel grade 316ln."

[16] M. Properties, "Oak wood – density – strength – melting point – thermal conductivity."

[17] L. Thomas and M. Ramachandra, "Advanced materials for wind turbine blade- a review," *Materials Today: Proceedings*, vol. 5, no. 1, Part 3, pp. 2635–2640, 2018. International Conference on Advanced Materials and Applications (ICAMA 2016), June 15-17, 2016, Bengaluru, Karanataka, INDIA.

[18] M. Jawaid, M. T. Hameed Sultan, N. Saba, and H. Bouguessir, *Sustainable Composites for Aerospace Applications*. 05 2018.

[19] A. Crosky, C. Grant, D. Kelly, X. Legrand, and G. Pearce, "4 - fibre placement processes for composites manufacture," in *Advances in Composites Manufacturing and Process Design* (P. Boisse, ed.), pp. 79–92, Woodhead Publishing, 2015.

[20] P. Mallick, *Composites Engineering Handbook*. Materials Engineering, Taylor & Francis, 1997.

[21] Y. Nawab, S. Shahid, N. Boyard, and F. Jacquemin, "Chemical shrinkage characterization techniques for thermoset resins and associated composites," *Journal of Materials Science*, vol. 48, no. 16, pp. 5387–5409, 2013.

[22] S. Gilet, "Wireless power transfer for structural health monitoring of composite structures," Master's thesis, Ecole polytechnique de Louvain, Université catholique de Louvain, Prom. : Flandre, Denis ; Francis, Laurent, 2016.

[23] B. sensor, *Linear Strain gauges for Bending Beam Force Transducers*. BCM sensor, Industriepark Zone 4, Brechtsbaan 2 B-2900 Schoten - Antwerpen, Belgium, 2021.

[24] A. D. Bykhovski, V. V. Kaminski, M. S. Shur, Q. C. Chen, and M. A. Khan, "Piezoresistive effect in wurtzite n-type gan," *Applied Physics Letters*, vol. 68, no. 6, pp. 818–819, 1996.

[25] M. Nie, Y.-h. Xia, and H.-s. Yang, "A flexible and highly sensitive graphene-based strain sensor for structural health monitoring," *Cluster Computing*, vol. 22, 07 2019.

[26] W. S. Lee, S.-W. Lee, H. Joh, M. G. Seong, H. Kim, M. Kang, K.-H. Cho, Y.-M. Sung, and S. Oh, "Designing metallic and insulating nanocrystal heterostructures to fabricate highly sensitive and solution processed strain gauges for wearable sensors," *Small*, vol. 13, p. 1702534, 10 2017.

[27] S.-R. Kim, J.-H. Kim, and J.-W. Park, "Wearable and transparent capacitive strain sensor with high sensitivity based on patterned ag nanowire networks," *ACS Applied Materials & Interfaces*, vol. 9, 07 2017.

[28] K. Arshak, D. McDonagh, and M. Durcan, "Development of new capacitive strain sensors based on thick film polymer and cermet technologies," *Sensors and Actuators A: Physical*, vol. 79, pp. 102–114, 02 2000.

[29] H. Nesser and G. Lubineau, "Strain sensing by electrical capacitive variation: From stretchable materials to electronic interfaces," *Advanced Electronic Materials*, vol. 7, no. 10, p. 2100190, 2021.

[30] K. Shivakumar and L. Emmanwori, "Mechanics of failure of composite laminates with an embedded fiber optic sensor," *Journal of Composite Materials*, vol. 38, no. 8, pp. 669–680, 2004.

[31] M. Torres, "Parameters' monitoring and in-situ instrumentation for resin transfer moulding: A review," *Composites Part A: Applied Science and Manufacturing*, vol. 124, p. 105500, 06 2019.

[32] M. Yeager, M. Todd, W. Gregory, and C. Key, "Assessment of embedded fiber bragg gratings for structural health monitoring of composites," *Structural Health Monitoring*, vol. 16, no. 3, pp. 262–275, 2017.

[33] D. Kinet, P. Mégret, K. W. Goossen, L. Qiu, D. Heider, and C. Caucheteur, "Fiber bragg grating sensors toward structural health monitoring in composite materials: Challenges and solutions," *Sensors*, vol. 14, no. 4, pp. 7394–7419, 2014.

[34] J. Sirohi and I. Chopra, "Fundamental understanding of piezoelectric strain sensors," *Journal of Intelligent Material Systems and Structures - J INTEL MAT SYST STRUCT*, vol. 11, pp. 246–257, 04 2000.

[35] B. Lin, V. Giurgiutiu, and P. Pollock, "Durability and survivability of piezoelectric wafer active sensors on metallic structure," *Aiaa Journal - AIAA J*, vol. 48, 03 2010.

[36] G. Thomas and A. Khatibi, "Durability of structural health monitoring systems under impact loading," *Procedia Engineering*, vol. 188, pp. 340–347, 12 2017.

[37] K.-S. Kim, M. Breslauer, and G. S. Springer, "The effect of embedded sensors on the strength of composite laminates," *Journal of Reinforced Plastics and Composites*, vol. 11, no. 8, pp. 949–958, 1992.

[38] J. Leng and A. Asundi, "Structural health monitoring of smart composite materials by using efpi and fbg sensors," *Sensors and Actuators A: Physical*, vol. 103, no. 3, pp. 330–340, 2003.

[39] A. Ghoshal, J. Ayers, M. Gurvich, M. Urban, and N. Bordick, "Experimental investigations in embedded sensing of composite components in aerospace vehicles," *Composites Part B: Engineering*, vol. 71, pp. 52–62, 2015.

[40] L. P. Canal, R. Sarfaraz, G. Violakis, J. Botsis, V. Michaud, and H. G. Limberger, "Monitoring strain gradients in adhesive composite joints by embedded fiber bragg grating sensors," *Composite Structures*, vol. 112, pp. 241–247, 2014.

[41] V. Murukeshan, P. Chan, L. Ong, and L. Seah, "Cure monitoring of smart composites using fiber bragg grating based embedded sensors," *Sensors and Actuators A: Physical*, vol. 79, no. 2, pp. 153–161, 2000.

[42] G. Pereira, C. Frias, H. Faria, O. Frazão, and A. Marques, "On the improvement of strain measurements with fbg sensors embedded in unidirectional composites," *Polymer Testing*, vol. 32, no. 1, pp. 99–105, 2013.

[43] "Effect of the recoating and the length on fiber bragg grating sensors embedded in polymer composites," *Materials and Design*, vol. 30, no. 5, pp. 1818–1821, 2009.

[44] K. Kuang, R. Kenny, M. Whelan, W. Cantwell, and P. Chalker, "Embedded fibre bragg grating sensors in advanced composite materials," *Composites Science and Technology*, vol. 61, no. 10, pp. 1379–1387, 2001.

[45] Y. Okabe, S. Yashiro, T. Kosaka, and N. Takeda, "Detection of transverse cracks in CFRP composites using embedded fiber bragg grating sensors," *Smart Materials and Structures*, vol. 9, pp. 832–838, nov 2000.

[46] Y. Yan and L. Yam, "Online detection of crack damage in composite plates using embedded piezoelectric actuators/sensors and wavelet analysis," *Composite Structures*, vol. 58, no. 1, pp. 29–38, 2002.

[47] H.-Y. Tang, C. Winkelmann, W. Lestari, and V. L. Saponara, "Composite structural health monitoring through use of embedded pzt sensors," *Journal of Intelligent Material Systems and Structures*, vol. 22, no. 8, pp. 739–755, 2011.

[48] J. S. Chilles, A. F. Koutsomitopoulou, A. J. Croxford, and I. P. Bond, "Monitoring cure and detecting damage in composites with inductively coupled embedded sensors," *Composites Science and Technology*, vol. 134, pp. 81–88, 2016.

[49] C. Hautamaki, S. Zurn, S. Mantell, and D. Polla, "Experimental evaluation of mems strain sensors embedded in composites," *Journal of Microelectromechanical Systems*, vol. 8, no. 3, pp. 272–279, 1999.

[50] Y. Su, J. Yang, Y. Liao, P. Zhou, L. Xu, L. min Zhou, and Z. Su, "An implantable, compatible and networkable nanocomposite piezoresistive sensor for in situ acquisition of dynamic responses of cfrps," *Composites Science and Technology*, vol. 208, p. 108747, 2021.

[51] A. Dinesh, S. Sudharsan, and S. Haribala, "Self-sensing cement-based sensor with carbon nanotube: Fabrication and properties – a review," *Materials Today: Proceedings*, vol. 46, pp. 5801–5807, 2021. International Conference on Advances in Materials Science, Communication and Microelectronics.

[52] K. M. Tripathi, F. Vincent, M. Castro, and J. F. Feller, "Flax fibers – epoxy with embedded nanocomposite sensors to design lightweight smart bio-composites," *Nanocomposites*, vol. 2, no. 3, pp. 125–134, 2016.

[53] J. Sebastian, N. Schehl, M. Bouchard, M. Boehle, L. Li, A. Lagounov, and K. Lafdi, "Health monitoring of structural composites with embedded carbon nanotube coated glass fiber sensors," *Carbon*, vol. 66, pp. 191–200, 2014.

[54] S. Nag-Chowdhury, H. Bellegou, I. Pillin, M. Castro, P. Longrais, and J. Feller, "Non-intrusive health monitoring of infused composites with embedded carbon quantum piezoresistive sensors," *Composites Science and Technology*, vol. 123, pp. 286–294, 2016.

[55] B. Wucher, P. Martiny, F. Lani, T. Pardoen, C. Bailly, and D. Dumas, "Simulation-driven mold compensation strategy for composites: Experimental validation on a doubly-curved part," *Composites Part A Applied Science and Manufacturing*, vol. 102, 08 2017.

[56] G. G. Stoney, "The Tension of Metallic Films Deposited by Electrolysis," *Proceedings of the Royal Society of London Series A*, vol. 82, pp. 172–175, May 1909.

[57] P. I. Karkanas and I. K. Partridge, "Cure modeling and monitoring of epoxy/amine resin systems. i. cure kinetics modeling," *Journal of Applied Polymer Science*, vol. 77, no. 7, pp. 1419–1431, 2000.

[58] C. Billotte, F. Bernard, and E. Ruiz, "Chemical shrinkage and thermomechanical characterization of an epoxy resin during cure by a novel in situ measurement method," *European Polymer Journal*, vol. 49, no. 11, pp. 3548–3560, 2013.

[59] G. Struzziero, B. Remy, and A. A. Skordos, "Measurement of thermal conductivity of epoxy resins during cure," *Journal of Applied Polymer Science*, vol. 136, no. 5, p. 47015, 2019.

[60] Q. Voleppe, *Characterization and modelling of the microstructure and fracture of thermoset/thermoplastic interphases*. PhD thesis, 09 2016.

[61] K. Magniez, A. Vijayan, and N. Finn, "Apparent volumetric shrinkage study of rtm6 resin during the curing process and its effect on the residual stresses in a composite," *Polymer Engineering & Science*, vol. 52, no. 2, pp. 346–351, 2012.

[62] W. Exner, A. Kühn, A. Szewieczek, M. Opitz, T. Mahrholz, M. Sinapius, and P. Wierach, "Determination of volumetric shrinkage of thermally cured thermosets using video-imaging," *Polymer Testing*, vol. 49, pp. 100–106, 2016.

[63] P. Karkanas and I. Partridge, "Cure modeling and monitoring of epoxy/amine resin systems. ii. network formation and chemoviscosity modeling," *Journal of Applied Polymer Science*, vol. 77, pp. 2178 – 2188, 09 2000.

[64] S. S. Li, "The dopant density and temperature dependence of hole mobility and resistivity in boron doped silicon," *Solid-State Electronics*, vol. 21, no. 9, pp. 1109–1117, 1978.

[65] D. Klaassen, "A unified mobility model for device simulation—i. model equations and concentration dependence," *Solid-State Electronics*, vol. 35, no. 7, pp. 953–959, 1992.

[66] D. Klaassen, "A unified mobility model for device simulation—ii. temperature dependence of carrier mobility and lifetime," *Solid-State Electronics*, vol. 35, no. 7, pp. 961–967, 1992.

[67] P. Navabpour, A. Nesbitt, B. Degamber, G. Fernando, T. Mann, and R. Day, "Comparison of the curing kinetics of the rtm6 epoxy resin system using differential scanning calorimetry and a microwave-heated calorimeter," *Journal of Applied Polymer Science*, vol. 99, no. 6, pp. 3658–3668, 2006.

[68] P. Kosky, R. Balmer, W. Keat, and G. Wise, "Chapter 12 - mechanical engineering," in *Exploring Engineering (Third Edition)* (P. Kosky, R. Balmer, W. Keat, and G. Wise, eds.), pp. 259–281, Boston: Academic Press, third edition ed., 2013.

[69] J. Magnus Svanberg and J. Anders Holmberg, "Prediction of shape distortions part i. fe-implementation of a path dependent constitutive model," *Composites Part A: Applied Science and Manufacturing*, vol. 35, no. 6, pp. 711–721, 2004.

[70] Y. Eom, L. Boogh, V. Michaud, P. Sunderland, and J.-A. Månson, "Time-cure-temperature superposition for the prediction of instantaneous viscoelastic properties during cure," *Polymer Engineering & Science*, vol. 40, no. 6, pp. 1281–1292, 2000.

[71] M. Harsch, J. Karger-Kocsis, and F. Herzog, "Influence of cure regime on the strain development in an epoxy resin as monitored by a fiber bragg grating sensor," *Macromolecular Materials and Engineering*, vol. 292, no. 4, pp. 474–483.

[72] G. Gardiner, "Integrating antennas into composite aerostructures."

UNIVERSITÉ CATHOLIQUE DE LOUVAIN
École polytechnique de Louvain
Rue Archimède, 1 bte L6.11.01, 1348 Louvain-la-Neuve, Belgique | **www.uclouvain.be/epl**